Experimental techniques for investigating lubricated, compliant, contacts

By

Connor William Myant

Thesis submitted to Imperial College London
for the Degree of Doctor of Philosophy
and Diploma of Imperial College London (D.I.C.)

April 2010

Tribology Section
Department of Mechanical Engineering
Imperial College London

Abstract

The study of Tribology between soft or compliant surfaces is not well understood despite its importance to many biological and engineering applications, ranging from synovial joints to rubber o-ring seals. It has also been shown that the science of Tribology and lubrication in compliant contacts is an important factor in the sensory perception and functionality of skin, hair and the oral cavity, and so has an immediate application of the design of consumer products such as skin creams, hair conditioners and foodstuffs.

This thesis aims to improve our understanding of thin film lubrication between soft, deformable surfaces under light loading and low-pressure conditions. The primary focus of the thesis is the development of techniques by which to measure the film thickness between compliant surfaces, from the nano- to the micro-scale.

Several experimental techniques currently exist for measuring film thickness in hard, metallic contacts and these are widely employed in Tribology research of engineering systems. However they require considerable modification to be applicable to compliant contacts. This thesis describes the development of two such techniques;

- a optical interferometric technique; for measuring nano-scale thicknesses in compliant contacts;
- a laser induced fluorescence technique; developed to enable measurement of lubricant thickness of relatively thick films in compliant contacts.

Acknowledgements

I would like to thank my supervisor, Hugh Spikes, for his advice and encouragement throughout the project.

Special thanks must go to Jason Stokes, who was always willing to answer the phone and discuss any queries I had. I wish him the best of luck in his new adventure at Queensland University. Thanks to everyone at Unilever Colworth who helped me and sponsored me throughout my PhD. Especially Jeroen Bongearts, Lubica Macakova, Gleb Yakubov, Ann-Marie Williamson, Pual Pudney and special thanks to George Marinov.

Huge thanks to everyone at PCS Instruments for their patience and help. Especially Matt Smeeth and Clive Hamer, who never seemed unwilling to discuss and solve any experimental issues. I'd also like to thank Celine Cluzel for all her help during the first half of my PhD in developing the MTM software.

I am indebted to Mark Fowell for all his help in writing the optical interferometry software. Without that a huge chunk this thesis would not be possible. And a big thank you to Dr Simon Medina for his help on adhesive forces.

I must thank everyone in the Imperial College Tribology team. Special thanks go to my climbing partner Danny Bear, Welshy for his guns work out, the Hoff for thrashing me at squash (every time!!). Robbie Bobby B, Big D, Dr K and the all the rest who were always around when I needed a pint after work. They all helped the batteries re-charge when they needed it most.

And, of course no amount of words can do it justice, but a huge thank you to Chrissy Stevens.

To Pete and Charmain. For all the inspiration and guidance they gave me when it mattered most. Thank you. x

Table of contents

List of tables

Chapter 3:

Chapter 4:

Chapter 5:

List of Figures

Chapter 2:

Chapter 3:

with a PDMS disk.

Chapter 4:

Chapter 5:

Chapter 6:

Chapter 7:

Chapter 8:

Chapter 1

Introduction

1.1 General Introduction

The study of tribology between compliant surfaces is not well understood despite its importance in many biological and engineering applications. For example it has also been shown that the science of tribology and lubrication in 'soft' or compliant contacts is an important factor in the sensory perception and functionality of skin, hair, food and beverage products [1].

By contrast, the Tribology of stiff solid surfaces in relative motion is now relatively well understood especially in terms of the lubricant film thickness generated between surfaces. A great deal of work has been carried out in this field, aimed primarily at reducing friction and extending the useful life of engineering components. Investigations have applied such work to the design of bearing and gear surfaces and the use of performance additives and surfactants within engine lubricants, to name but a few applications [2,3]. A few film thickness studies have also been carried out in compliant-tribological systems, but our understanding of this topic lags behind that of stiff contacts. 'Soft' or compliant-tribology research has, in the past, been led by the rubber and oil seals industry, with very little interest or knowledge originating within the bio-medical and bio-science industries. The latter industries have traditionally focussed on the rheological properties of fluids rather that their tribological ones.

1.2 Research Objectives

This project aims to develop a clearer understanding than exists at present of liquid lubrication between compliant surfaces under light load and low pressure conditions, compared to stiff, metallic contacts. The primary focus will be on developing

techniques with which to measure the film thickness between shearing surfaces from the nano- to the micro-scale.

Techniques exist to measure film thickness in hard, or metallic, contacts, but these need considerable modification to be applied to compliant contacts. The techniques to be used in this project will be:

- Optical interferometric technique; will be applied to measure nano-scale thicknesses in compliant contact.
- A laser induced fluorescence technique will be developed to enable measurement of thickness for relatively thick films.

The development of visualization and film thickness measurement techniques could then be utilized by industry to gain a better mechanistic understanding of the lubricating properties of their product. Ultimately, this may lead to improved controlled product design.

1.3 Structure of thesis

The thesis starts with a literature review of techniques for investigating lubricated, compliant contacts in chapter 2.

Chapter 3 describes the main experimental technique used to investigate friction in lubricated, compliant contacts. Results from this work are presented and discussed in chapter 4.

Chapter 5 describes the first of the two experimental techniques developed to measure lubricant thin film thickness in a compliant contact. This is optical interferometry, which is a standard technique for measuring lubricant film thickness in ‘hard’, metallic contacts. The technique is developed and adapted to meet the

requirements of poorly reflective contacting materials, where one or both materials have a low elastic modulus.

Film thickness results obtained using the modified interferometry method is presented in chapter 6. Film thickness maps and profiles across a range of applied loads and entrainments are shown for two Newtonian fluids. Film thickness maps are compared to a theoretical model.

The second of the two film thickness techniques is presented in chapter 7, where the use of laser induced fluorescence (LIF) to measure lubricant film thickness in compliant contacts is explored. Chapter 8 presents results for a pure sliding contact between PDMS and glass lubricated with glycerol and water solutions over a range of entrainment speeds. Film thickness measurements are made for both fully-flooded and starved conditions using LIF.

A final summary and conclusions, as well as suggestions for possible future work to follow on from that already carried out are presented in chapter 9.

Chapter 2

Techniques for investigating lubricated, compliant contacts: A review

The following chapter reviews the state of experimental techniques and procedures for measuring friction and liquid film thickness in both stiff and compliant contacts. Particular reference is given to the developments of test apparatus for investigating the isoviscous elastohydrodynamic lubrication (I-EHL) regime.

In many practical lubricated engineering and biological applications one or both of the bodies in the contact has a low elastic modulus and the prevailing lubrication mode is Isoviscous-Elastohydrodynamic Lubrication (I-EHL). In this regime, the contact pressure is large enough to cause significant elastic deformation of one or both of the interacting solids, but the pressure within the contact is low and insufficient to cause any substantial change in the lubricant viscosity within the contact inlet [4]. Typical example applications are:

- Friction of windscreen wipers [5]
- Road and tyre contact [6]
- Performance of rubber o-ring seals [7-10]
- Studies of natural synovial joint lubrication [11,12],
- Oral processing [1]
- Taste and taste perception of foodstuffs and beverages [13-16]
- The feel and function of cosmetics and skin cream [17]

Most previous experimental investigations into I-EHL have focussed on the frictional characteristics of lubricated compliant contacts. By measuring friction/entrainment speed curves or "Stribeck curves" one is able to obtain a clear indication of the prevalent lubrication regime. This has shown how lubrication regimes can be controlled by varying contact parameters such as slide/roll ratio [18], surface roughness [19] or wetting characteristics [20]. There has been a growing interest within the biological industry to understand the tribological properties of complex fluids, in particular foodstuffs and skin cream. For example, for many soft-solid foods, it has become clear through controlled sensory tests that bulk rheology alone does not provide all the characterisation of in-mouth sensory properties [21]. It is now recognised that the tribological properties of the foodstuff in the soft tongue/palate contact influence how the food is perceived [1]. Likewise, for non-Newtonian fluids, both their in-use performance and processing is dependent on the solutions' tribological properties [16]. It is therefore important to model these bio-surfaces and processes.

2.1 Test materials for biological surfaces

In-situ testing of bio-surfaces is difficult to achieve. However, there have been a few studies in which the tribological properties of bio-surfaces have been investigated by employing a real bio-surface. Prinz *et al.* [22] investigated the frictional conditions within the human mouth. The coefficient of friction between two pig mucosal surfaces was measured using human saliva. Work carried out by Adams *et al.* [17] and Tang *et al.* [23,24], investigated the lubricating properties of human skin. Adams *et al.* used a smooth glass or polypropylene, spherical tipped probe sliding against a human forearm, while Tang *et al.* employed shaved Porcine skin. Results were reported for a range of lubricating conditions, but repeatability of testing was difficult to achieve.

Due to ethical issues and the difficulty in obtaining biological tissues many researchers have used elastomer as a replacement test medium and, for the majority of research, crosslinked polydimethyl siloxane (PDMS) has been employed. This is widely used to mimic bio-surfaces due to its similar mechanical properties to human tissue. PDMS is utilized as one [18,21,23,24] or both [1,20,25] of the contacting surfaces in the tribological contact to maintain low contact pressures and create the conditions for I-EHL to occur. One key advantage of PDMS which has contributed to its widespread use is its ease of fabrication. Prior to crosslinking, PDMS can be cast into suitable moulds of almost any desired shape. Other attractive features of PDMS include its physiological inertness, availability, low unit cost, as well as its good thermal and oxidative stability.

The tribological properties of PDMS are now well understood. Vorvolaskos and Chaudhury [26] investigated the effect of molecular weight and test temperature on friction in a pure sliding contact between a PDMS and metal surface. Bongearts *et al.* [25] investigated the effect of surface roughness of PDMS on the lubricating properties of biopolymers and aqueous solutions. PDMS, like most elastomeric

surfaces, is by nature hydrophobic but an oxidation treatment can be employed to create a hydrophilic surface. Hillborg *et al.* [27-29] and Schneemilch *et al.* [30] investigated the wettability of PDMS before and after oxidisation by several techniques and studied the effect of crosslink density on oxidation. Lee *et al*. [20], and de Vicente *et al.* [14,31] looked at the influence of surface modification of PDMS on its aqueous lubrication properties.

However, there remains some debate over the suitability of PDMS as a model bio-surface. Ranc *et al.* investigated the effect of surface structure on the frictional behaviour of a tongue/palate tribological system [32]. The tribological system involved steel or PTFE hemispherical body sliding against silicone samples, with the latter having well-defined surface structures that were produced in order to cover the different scales of roughness of the human tongue. PDMS was selected to model a human tongue because of closely-matching mechanical characteristics. The investigation by Ranc *et al.* found that friction is affected by a complex combination of factors, such as surface topography, contact pressure, wetting behaviour and build up of lubricating film. The investigation concluded that moulded silicone surfaces constitute a promising way to asses the effect of tongue topography on 'in-mouth' friction.

In a similar investigation, by Dresselhuis *et al.* [33], the surface characteristics of pig tongues were compared with that of PDMS. The investigation concluded that PDMS showed dissimilarities in surface characteristics to those of a tongue surface; therefore oral mucosa and PDMS rubbers, even with a structured surface to reproduce biological scenarios, are very different and not interchangeable in tribological experiments. Although PDMS rubbers have similar hydrophobic qualities to a tongue, PDMS is smoother and has an elastic modulus two orders of magnitude larger. Finally, Dresselhuis *et al.* [33] suggested that tribological studies using simple rubber devices were not suitable for studying the behaviour of emulsions in the mouth. However, Dresselhuis *et al.* failed to take into account the variable mechanical characteristics of a 'live' tongue. Despite their conclusions, many authors continue to use PDMS in modelling 'in-mouth' friction.

2.2 MTM friction testing

The majority of laboratory investigations into the lubricity of liquids are performed using a tribometer; *i.e.* a friction measuring instrument. There are a number of tribometers commercially available but perhaps the best known and widely used is the MTM, or Mini Traction Machine (PCS Instruments, London, UK).

Due to the growing interest in bio-contacts, the MTM has been used to assess lubrication properties of some biopolymers in conditions relevant to describe bio-tribological contacts; *i.e.* significant elastic deformation of the mating surfaces but insufficient contact pressure to cause any increase in the lubricant viscosity [34]. There is a lack of knowledge concerning the real-life contact conditions of bio-tribological contacts; *i.e.* contact pressures and entrainment speeds during oral processing. Much of the research has, therefore, sought to merely create I-EHL conditions, which is considered to be the main lubrication regime. To make these investigations possible, modifications were needed to the MTM, which was originally designed to study steel/steel contacts. Cassin *et al.* [34] noted that, with steel-steel conjunctions, the maximum Hertz contact pressure is around 1 GPa for a load of 10 N. Such contact pressures are irrelevant for describing tribological contacts between soft, deformable surfaces. A lower load can be applied during testing, but between a pair of non-conforming steel surfaces, Hertz theory means that pressures continue to be above 10 MPa even at mN levels of load. For this reason, a body with a low elastic modulus is essential. As a result, all experiments by Cassin *et al.* [34], and later by de Vicente *et al.* [14-16,18,31] were carried with an elastic disc. Figure 2.1 shows the standard ball on disk setup employed by the MTM, and the elastomer disk setup employed by Cassin and later by de Vicente *et al.* [18].

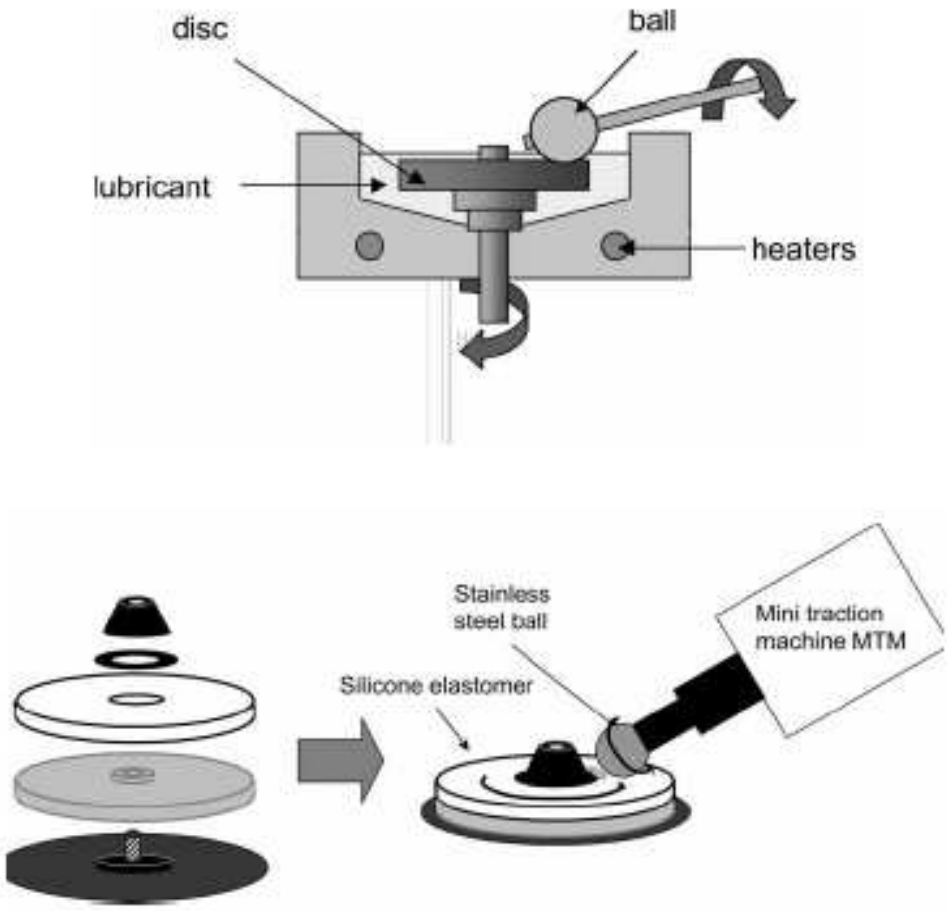

Figure 2.1. Schematic representation of the mini traction machine and arrangement of the silicone elastomer disc holder (MTM) [18].

De Vicente *et al.* [18] compared friction results using the MTM to the predictions of a numerical models. However, the models predicted lower friction than that measured and disparities of ~ 4% were found. It was concluded that these errors between theoretical models and MTM data were due to minor errors within the MTM, rather than the models themselves; in particular a calibration error in the applied load, which is used to convert measured friction force into friction coefficient. The load is applied by a leaf spring and stepper motor and calibrated by counting the number of steps taken by the motor to reach contact, when under an arbitrary upward load. All other loads are extrapolated from this calibration process. Bongaerts *et al.* [25] noted that the compliance of the elastomer renders it impossible to know the exact curvature of the load beam (and hence the applied load) if the

curvature is not measured directly. Therefore, Bongaerts *et al.* installed a strain gauge on to the leaf spring through which the load is applied on the MTM. They found that previous studies carried out at 3 N were in fact carried out at 1.3 N. The addition of the strain gauge makes more accurate low load/low pressure investigations possible.

Studies done by Cassin e*t al* [34] used a soft elastomer mounted on a stainless steel disc to decrease the contact pressure. This modification emulated more realistically the forces applied in the mouth and the hydrophobic nature of the oral tissues than the conventionally-used steel [21]. Elastomer can be used to model the compliance, surface roughness and surface chemistry that exist in many bio-tribological contacts [25]. The low elastic modulus and low contact pressure means that, when a lubricating film is present, the contact should operate in the I-EHL regime [16].

2.3 Film thickness measurements

When designing any component that will encounter lubricated sliding, the fluid film thickness is one of the most important components in its design and eventual performance. At large film thickness, within the I-EHL regime, where surface asperities are no longer in contact, the hydrodynamic properties of the fluid govern the frictional forces between the two surfaces. As a result, energy is needlessly expended to overcome shearing and churning losses. In contrast, for very thin film thicknesses, typically lower than 1-3 nm, breakdown of the boundary lubricating film can occur, causing high levels of friction and wear. In the last sixty years a large number of lubricant film thickness measurement techniques have been developed, with varying amounts of success.

As yet there is no established technique for routinely obtaining film thickness data within compliant contacts formed by elastomeric and most biological materials. Indeed, to date there has been little work published on film thickness measurements

in I-EHL contacts. This is unlike stiff contacts formed by most ceramics and metals, where optical interferometry is now routinely used to measure the EHL film thickness properties of lubricants, while electrical capacitance measurements are often employed to measure EHL and hydrodynamic film thicknesses in engineering components. To identify an appropriate technique of measuring film thickness in compliant contacts it is valuable to review the available techniques for detecting lubricant presence in non-compliant contacts. These are now presented.

Currently the techniques for measuring lubricant film thickness within lubricated contacts can be divided into two main groups, those based on electrical techniques, e.*g.* electrical capacitance and resistance measurement and electromagnetic radiation-based techniques; *e.g.* optical interferometry, Raman spectroscopy, X-ray transmittance, laser fluorescence. There are also a few other techniques such as ultrasonics and direct displacement.

2.3.1 Electrical techniques

Electrical methods for measuring lubricant film thickness involve obtaining, (by direct measurement or deduction), an electrical property of the lubricant film (typically resistance, capacitance or inductance), which is then linked to film thickness [2]. An electric circuit is created which includes the two surfaces and the film between them. The contact electrical properties will be a function of the contact area, contact geometry and material properties, contact conditions, operating lubrication regime and the electrical resistivity or capacitance of the contacting material and lubricant. When direct metal-to-metal contact is made between the specimens, there will be a short circuit, and the potential or capacitance will be reduced to zero, thus a zero film reading. During a test, the lubricant between the specimens is normally non conductive, so the electrical signal gives an indication of the separation of the specimens. The electrical properties of this circuit change according to the distance between the two surfaces, and thus an indicator of lubricant

film thickness within the contact can be deduced. Electrical techniques have the benefit to being suited to study metal-metal contacts but are difficult to calibrate and require electrical isolation.

The electrical techniques of electrical contact resistance (ECR) [35] and voltage discharge [36-38] have been applied to measure lubricant film thickness since the 1950s, but with only limited success [39]. It is important to note here that ECR is used as an indicator of the presence of a separating lubricant film thickness or the level of contact interaction, as it can not be calibrated to quantitative thickness measurements. A tool for monitoring such information using ECR has, indeed, recently been developed as an additional accessory for the MTM (PCS-Instruments, UK) [40]. Resistive techniques involve supplying either a constant voltage or current and deducing the resistance. Once surfaces are fully separated, the ECR signal reaches a maximum and there is no further change. This limits the technique's value to the boundary and mixed lubrication regimes. There are a number of other disadvantages of this approach; the sensor must be insulated and surface mounted or components must be in complete electrical isolation of the contact elements. The applied potential across the contact can cause undesired rheological effects, caused by molecular alignment and arc degradation/oxidisation of the lubricant can occur at high voltages.

From the 1960s, measurement of electrical capacitance became a popular technique for measuring lubricant film thickness. Like resistive techniques, capacitive techniques require electrical isolation. However, capacitance can be calibrated to give direct lubricant film thickness measurements. The technique is based upon the fact that the capacitance present between two parallel plates is inversely proportional to the separation between the surfaces. Unlike ECR method, capacitance will work within the EHL regime; indeed, accuracy will increase as film thickness decreases within the EHL regime, so capacitance is a popular technique for investigating film thickness in high pressure, smooth, contacts, such as ball bearings. From the 1960s, the capacitance method allowed previously unvalidated, theoretical film thickness predictions of EHL lubrication to be experimentally confirmed [39].

One disadvantage of electrical techniques is the location of the sensor. The sensor or probe must be in contact with the oil and therefore located at the bearing surface. Capacitance or resistance probes are located at a bearing contact face and may be recessed into the surface. This may structurally weaken the bearing component and or disrupt the formation of the oil film. However, over the last few decades improvements in modern electronics and miniaturization, and the availability of sputtering, have reduced the likelihood of interference by the probe on lubricant behaviour. Microtransducers have become employed to produce film thickness, temperature and pressure across EHL contacts [41]. The ability to obtain scalar profiles greatly strengthened the capacitance technique since it removed some of the difficulties of interpreting average capacitance measurements across contacts [39].

2.3.2 Magnetic resistance

In an attempt to measure film thicknesses up to the hundreds of microns within compliant I-EHL contacts, Poll *et al.* [8] used an approach involving magnetic flux measurement. Here, magnetite particles were dispersed within the lubricant, using surfactant molecules to protect against oxidation and coagulation. The particle size (average diameter of 10 nm and maximum of 80 nm) is claimed to be sufficiently small to avoid affecting film formation or wear. A magnetic circuit is built such that magnetic flux is directed through the seal contact. Due to the high permeability of magnetite, the inductivity and impedance of the coil, providing the magnetic potential, can be calibrated to the amount of fluid present. Using this method, film thickness was successfully measured within a rotary lip seal. The advantage with this technique is that no optical window is required, the input and output signal are transmitted by the same device (no separate optics for ingoing and out coming light). The test specimen keeps its original surface microgeometry (no optical transparency required), allowing rough surfaces to be investigated. Although, few results are given to prove the system resolution is capable of this. The technique suffers from a

number of disadvantages; firstly a magnetic fluid is required, this clearly limits the range of lubricants which can be tested, and puts a lower limit on the measurable thickness. Contact profiles of the lubricant film cannot be recorded simultaneously but only by axial displacement of the sample or test rig (in relation to each other), making film thickness maps difficult to obtain.

2.3.3 Ultrasonic and mechanical methods

Mechanical methods such as direct displacement were some of the earliest used techniques for measuring lubricant film thickness. As early as 1886 Goodman used a simple experimental apparatus which employed a micrometer screw to measure liquid film thickness in journal bearings [42]. Over the last century the technique has developed considerably and now employs the use of laser detection techniques, which greatly increase test accuracy [43]. An alternative technique is Ultrasound which uses ultrasonic sound waves sent through the lubricated contact. The reflected pulses are digitised using either an oscilloscope or a PCI digitising card in a PC. A coefficient amplitude spectrum can then be produced, and film thickness values calculated. The technique is still in its infancy and has not been widely used due to lack of calibration, testing, and validation [44]. Ultrasound methods are constrained by the need to match acoustic properties of the contact mediums. Also, although film thickness mapping is possible, it is time consuming and therefore the method is confined to film thickness measurements analyzed over a region of contact.

2.3.4 Electromagnetic radiation

An advantage of all the above methods is that no observation window is needed to obtain film thickness measurements, making it easier to obtain in-situ, real time

measurements from engineering components. However, all the above systems lack the ability, or it is very time consuming, to map film thickness over the entire contact. To do this one, or both, of the rubbing surfaces must be made transparent to some form of electromagnetic radiation and emitted or transmitted radiation used to probe film conditions [39].

A number of techniques for measuring film thickness exist based on electromagnetic radiation. These include X-ray transmission, Infrared (IR) absorption spectroscopy, IR emission and Raman spectroscopy. As well as film thickness [45], some of these techniques also allow lubricant temperature [46], rheology [47], composition [19], and molecular alignment [48] to be investigated. By using a confocal method, lubricant film thickness can be measured, although the accuracy is only as good as the focusing resolution. Wahl *et al.* [49] have applied confocal Raman spectroscopy to measure in situ Raman spectra from within the rubbing contact. A contact was formed between a hard probe and a glass slide, a small sinusoidal motion was applied. The system has the added ability of detecting lubricant composition through depth and position in contact. However, Wahl *et al.* suffered from limited range of entrainment speeds and could not maintain a continuous flow from one direction. Bae *et al.* [50] performed confocal Raman experiments in a surface-force apparatus to investigate confinement effects on the nanometer scale. Although very suitable for investigating nano-rheological properties in a well-defined model contact, it is not suitable at the contact scales at speeds that are present in most I-EHL operating contacts.

Bongaerts *et al.* [19] successfully demonstrated the use of confocal Raman spectroscopy to measure lubricant film thickness and composition within a complaint tribological contact, lubricated with simple Newtonian fluids and stabilized oil/water emulsions. It is the ideal technique for emulsions and opaque lubricants, *e.g.* shampoos. However, the process has certain limitations. Water has a poor Raman signal, so aqueous solutions need another bulk solvent added to the polar phase, making low viscosity aqueous solution difficult to study. It is time

consuming and values can only be obtained at singular points, making lubricant film thickness maps or profiles difficult to acquire.

2.3.5 Optical Interferometry

Optical interferometry was first used in the 1960s as a quantitative tool for measuring lubricant films in contacts. It was realised that EHL film thickness was the same order of magnitude as the wavelength of visible light [51], thus interferometry was seen to have the potential to study this lubrication regime. Interferometry was used to study both hard [52] and compliant [53] contact situations during the early 1960s.

By using white light Gohar *et al.* [52] and Cameron *et al.* [54] were able to create chromatic interferometric images, and thus map film thickness sliding and rolling EHD contacts. The principle of this early work is illustrated in Fig. 2.2.

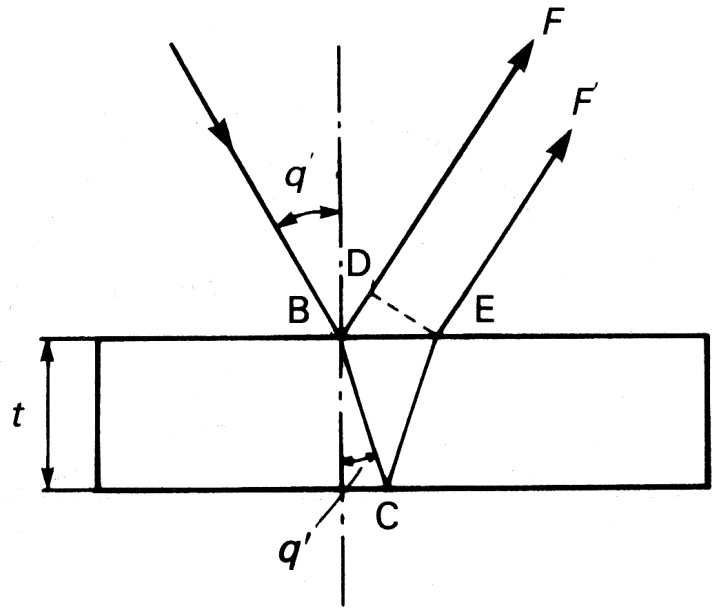

Figure 2.2 Principle of Two-beam optical interferometry [2]

A lubricated contact is formed between a steel ball and glass disc. White light illuminates the contact region through the glass window. Light is reflected from the underside of the glass disc and the steel ball. A phase difference is created between the two reflected beams, due to one travelling twice through the lubricant. Optical interference then occurs on recombination [51]. The use of white light creates complex interference maps where the perceived colours vary continuously. A time-consuming film thickness/perceived colour calibration process is therefore required before film thickness measurements can be calculated from interferograms.

During the late 1960s, Gohar and Cameron refined their optical interferometry system in two important ways. The use of monochromatic and later duochromatic light sources instead of white light, led to improved interference fringe clarity [55]. Duochromatic interferometry utilizes two discrete wavebands of light, these were normally green and red [56], giving the fringe clarity of monochromatic with resolution close to that of chromatic interferometry [51]. The second was the introduction of a semi-reflective layer on the underside of the glass disc. This had the effect of enhancing the reflectivity at the glass/lubricant interface [57]. This system enabled multiple beam interferometry [2], which produces much sharper interferences fringes than two-beam interferometry. The principle is shown in Fig. 2.3.

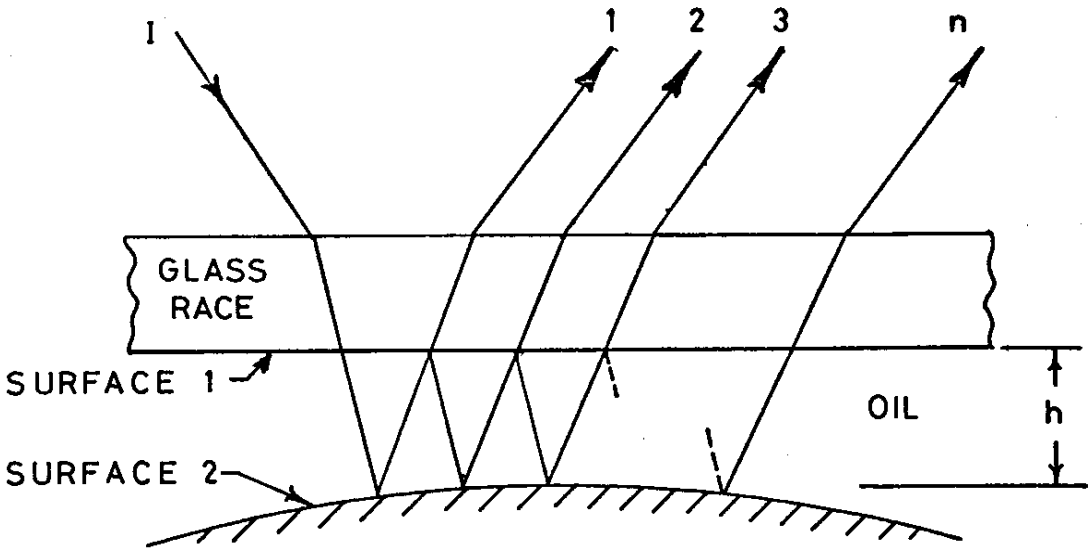

Figure 2.3 Multiple-beam optical interferometry [56]

The above interferometry systems were limited to minimum film thickness of 45~75 nm. For optical interference to occur the path difference must be at least half a wavelength of light, which means films less than one quarter of a wavelength of light thick (70 nm) cannot be measured [2]. The human eye's inability to accurately distinguish colours gives the systems a resolution limit of ± 10 nm [39]. In 1967, Westlake overcame these limitation by inventing the 'spacer layer' approach [58]. By sputtering a transparent layer on top of the semi reflective layer with the same refractive index as the lubricant, the spacer layer and lubricant act as one. Their total thickness is now always greater than one quarter wavelength of the light used. This allows thin film thickness measurements down to ~ 20 nm.

By 1990, the principles of all the above methods had been combined and developed to produce ultrathin film interferometric techniques [59]. Incorporating the spacer layer method and spectrometric light dispersion, ultrathin film thickness measurements of ~ 1 nm were made possible [51]. Chromatic light illuminates the contact and film thickness measurements can be taken from the resulting images using two different processes. The interfered reflected beam can be directed to a spectrometer and dispersed by wavelength. The resulting spectral image is then detected by a black and white CCD camera and captured by a frame grabber. By

finding the wavelength of maximum constructive interference or each row of pixels can be analysed independently to yield a separation profile across the contact [51]. A schematic diagram of ultrathin film interferometry is given in Fig. 2.4.

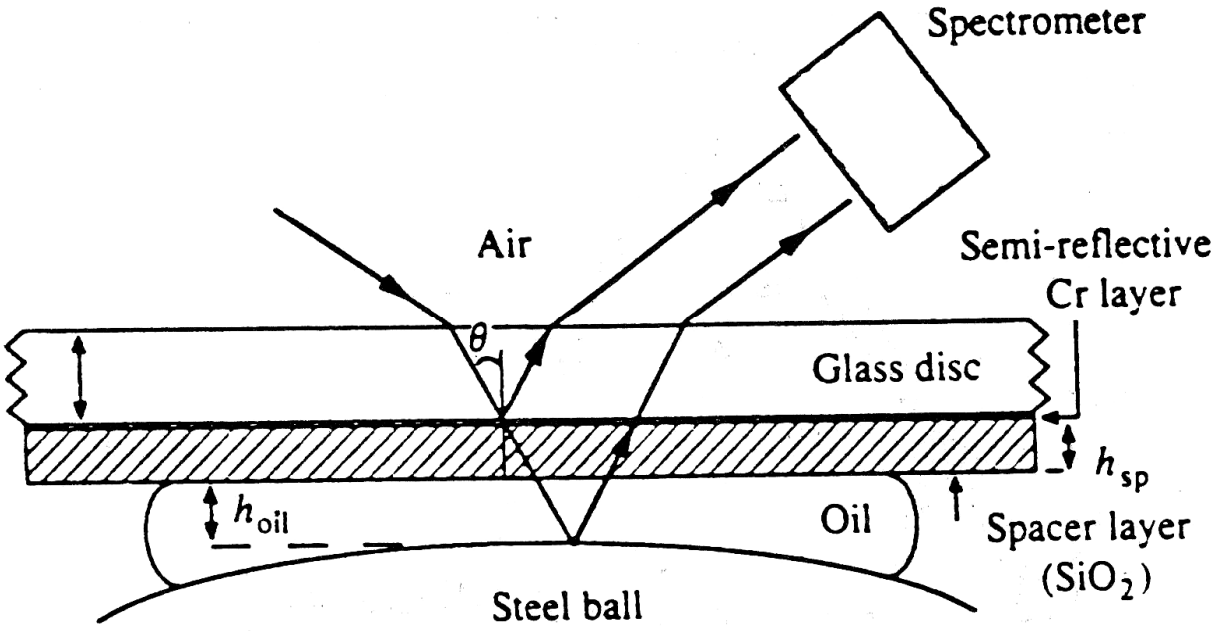

Figure 2.4 Principle of ultra thin film interferometry. [2]

Ultrathin film interferometry is limited to 1-D film profiles, due to the need for spectrometric dispersion. A 2-D mapping of the film separation across the contact was developed by Gustafsson *et al.* [60] in the early 1990s. Previous mapping techniques had involved compiling photographic or video images and was a time consuming process. Gustafsson *et al.* used computer processing to analyse captured images, pixel by pixel, and create film thickness maps based on colour representation of interference images. The process was developed and refined to combine spacer layer and chromatic light methods [61]. In this spacer layer imaging method (SLIM) each pixel is analysed using a set of RGB optical path difference calibration curves, to produce a measure of separation at that point, which, after subtraction of the spacer layer thickness yields the lubricant film thickness [62].

The silica layer is applied to the plain glass surface using radio frequency sputtering, which can produce small variations in the silica thickness. It is difficult to obtain exact film thickness values for the silica layer, the estimation of which has a strong influence on the accuracy of measured film thickness values [63]. The sputtered layers are expensive to produce and are prone to wear, which will introduce errors in film thickness measurements. Recently Křupka *et al.* [64-66] developed an ultra thin film thickness measurement technique that does not require a spacer layer. This has been achieved by replacing the RGB scale with the more complex CIELAB space colour map and improvements to the calibration process that provide colour to film thickness dependence in the form of empirically-fitted functions instead of discrete look-up tables.

'Soft' or compliant contact interferometry is based on the same principle as hard contact interferometry. Work conducted by Blok and Keons [53] used an interferometric technique to study lubricant behaviour of a flexible rubber seal on a reciprocating rod. Visualisation of the contact was achieved, but image quality was low (Fig. 2.5). Therefore results were more qualitative than quantitative.

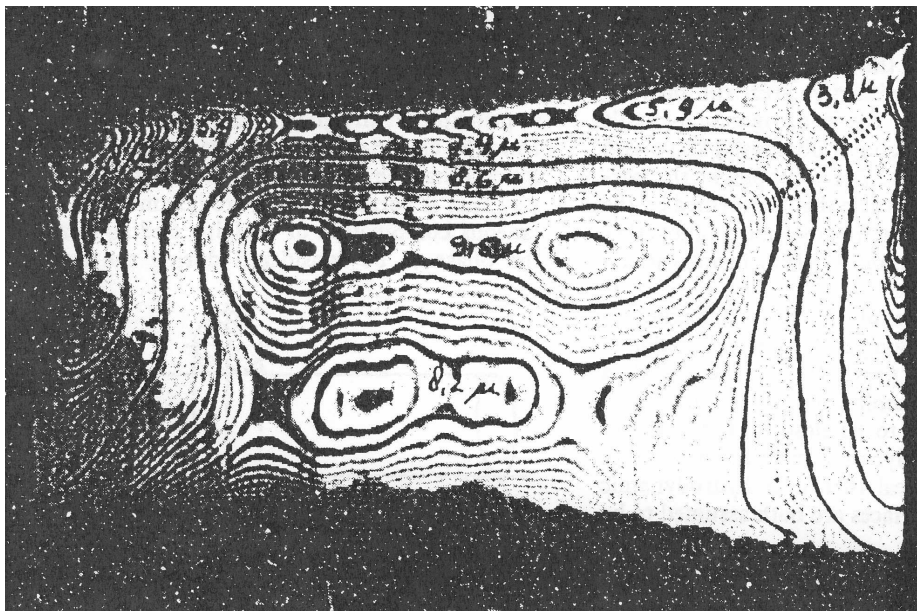

Figure. 2.5 Interference pattern corresponding to a certain phase in a breathing cycle. [53]

It was not until the late 1960s in a series of pioneering studies by Roberts and Tabor [67] that soft contact interferometry produced reliable quantitative results. The interference between a flat glass plate and a hemisphere or hemicylinder of smooth rubber was examined by reflected monochromatic light. It was found that conventional rubber surfaces were rough and poorly reflecting so the interferometric observations were unsatisfactory [68].

Two important developments took place in the early 1970s to improve image quality. First, Roberts *et al.* [68] successfully developed optically smooth rubber samples with the help of Trico-Folberth Ltd and the Avon Rubber Company. The optically smooth samples were created using hot compression moulding against polished glass or metal formers [69]. Optically smooth rubber surfaces with peak-to-valley surface roughness no greater than 20 nm [70] could be created using this process. Samples were developed further [71] by adding carbon black to the specimens before curing. This improved light absorption and therefore reduced interference light and improved image quality, this can be seen by comparing Figs. 2.5 and 2.6. The second important advance was to replace the flat glass disc with an Abbe prism. The illuminating beam is now at non-normal incidence to the contact area, so the amount of scattered light received by the detector is greatly reduced. Using this method Roberts *et al.* [71,72] were able to achieve film thickness measurements down to ~ 20 nm.

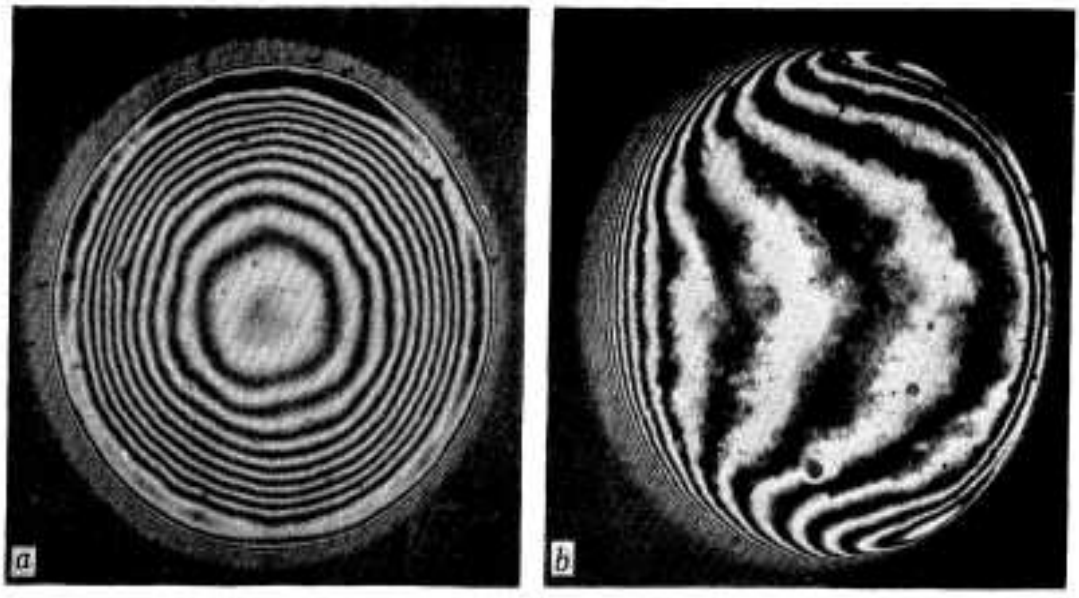

Figure 2.6 Interference patterns corresponding to (a) squeeze film conditions and (b) sliding conditions (velocity 0.1cm/s). [68]

Early soft contact work was restricted to static loading and studied fluid film flow squeezed from the contact zone over a time period [67,72,73]. These initial investigations were used to compare experimental results to existing theoretical models [74]. A small, lateral, sinusoidal motion was introduced by Roberts [68,71] and visualisation of the contact was achieved with good image quality. Film thickness and friction results were taken at low sliding speeds in the range of 70 μm s^{-1} – 5 mm s^{-1}.

More recently Kaneta *et al.* [9,10] used a monochromatic optical interferometric technique to investigate the lubricant film thickness in a reciprocating, compliant, line contact. Film thickness and friction measurements were obtained simultaneously. Investigations were made into the behaviour of o-ring seals by forming contacts between a nitrile rubber specimen of D-shaped cross section and a sinusoidally-oscillating, flat glass plate. Film thickness and friction coefficient profiles were reported at a range of positions within the stroke. There are two key difference between the technique presented by Kaneta *et al.* and that used by Roberts *et al.* Firstly, Kaneta *et al.* use a flat glass plate as the optical window with the illuminating beam projected into the contact at an angle of 55°. Secondly, Kaneta *et*

al. use a semi-reflective layer on the glass surface. The use of this seems confusing as its presence will greatly increase the reflectivity of the glass/lubricant interface and drown out the lubricant/rubber reflection, resulting in a reduction of image visibility. Disappointingly there is little explanation given by Kaneta *et al.* of the need for a semi-reflective layer, the significance of which is discussed further in chapter 5.

2.3.6 Laser induced fluorescence

As a tool to measure lubricant film thickness, fluorescence has several advantages over other, more established techniques. A limiting factor to optical interferometry is the coherence of the illuminating light which is reduced as the separating gap is increased. Interference image quality reduces proportionally with reducing coherence and eventually film thickness measurements are no longer obtainable. This critical point is dependent on the interference system in use; *i.e.* reflecting surfaces, light source *etc*. and generally occurs at thicknesses around 2 μm. Theoretically fluorescence has the capability to measure far greater values of film thickness. Another significant advantage of fluorescence techniques is that they require no reflective coatings on the contacting surface. Such coatings are expensive and are prone to wear, especially for rough surfaces. Fluorescence also has the potential to measure very low levels of photon emission down to as little as that emitted from one molecule. This can be achieved with development of the experimental equipment and the use of modern visible light photon detectors, which are extremely sensitive.

There has been very little application of fluorescence to EHL contacts, probably because optical interferometry already provides an accurate measurement tool for most applications. Sugimura *et al.* [75] used laser induced fluorescence (LIF) to measure thin lubricant films in hard ball-on-disc contacts. Attempts were made to

measure thin lubricating films in a ball-on-disc contact using a normal CCD camera system. However there were two substantial problems that made accurate thickness determination difficult. Poor image equipment meant a high level of background noise was present in all images and optical interference within thin films, inherent in all illuminated hard/metallic contacts. This was solved by making both contacting bodies transparent; however this reduced the detected intensities further. Consequently, few experimental film thickness results were presented. Poll *et al.* [7] successfully used fluorescence to investigate lubricant film thickness in rubber rotary lip seals. Few results were given, but sub-micron film thickness measurements were achieved across a narrow entrainment speed range (10 – 150 mms^{-1}). Poll *et al.* also present a clear explanation of the LIF technique.

Since this work, photon detection equipment, as well as fluorescent dye technology, have advanced significantly. Hidrovo *et al.* [76] used modern EMCCD equipment and a two-dye technique. The need for two fluorescent emissions arise as a consequence of the fluorescence dependence on excitation light intensity, as observed by Sugimura *et al.* A ratiometric scheme that normalizes the fluorescent emission of one dye against a second dye is used in order to eliminate undesirable effects due to illumination intensity fluctuations, in both space and time, optical interference and optical distortions [77]. High quality images were presented but the lower and upper limits of the system were not identified, nor was the technique used on a realistic tribological contact. Much of the noise seen in the images presented by Hidrovo *et al.* is the result of a highly focused powerful laser which has a strong Gaussian distribution. By using simple optics this laser intensity distribution can be flattened, although at the cost of lowering the intensity power. Such an approach would eliminate the need for two EMCCD cameras, which are expensive.

2.4 Numerical investigations into lubricated, compliant, contacts

Theoretical, numerically-based investigations into lubricated, compliant, contacts can be split into two groups; (i) fully flooded, I-EHL regime (ii) dry and partially lubricated conditions.

Previous investigations into I-EHL have concentrated on modelling the full film hydrodynamic regime. This has led to regression equations for predicting the film thickness in the isoviscous-EHL regime. Perhaps the best known of these are the Hamrock and Dowson equations for film thickness in elliptical contacts for materials of low elastic modulus [78];

$$\tilde{H}_c = 7.32(1-0.972e^{-0.28k})\overline{U}^{0.64}\overline{W}^{-0.22} \quad (2.1)$$

$$\tilde{H}_m = 7.43(1-0.85e^{-0.31k})\overline{U}^{0.65}\overline{W}^{-0.21} \quad (2.2)$$

where $\tilde{H}_c$ and $\tilde{H}_m$ are the dimensionless central and minimum film thicknesses respectively and equal to h/R'. k is the ellipticity parameter, which reduces to unity for the circular contact of interest in this project. Therefore;

$$h_c = 3.3\overline{U}^{0.64}\overline{W}^{-0.22}R' \quad (2.3)$$

$$h_m = 2.8\overline{U}^{0.65}\overline{W}^{-0.21}R' \quad (2.4)$$

where h_c and h_m are the central and minimum film thickness respectively and the dimensionless operating parameters are:

$$\text{dimensionless speed parameter, } \overline{U} = \frac{U\eta}{E'R'} \tag{2.5}$$

$$\text{dimensionless load parameter, } \overline{W} = \frac{W}{E'R'^2} \tag{2.6}$$

where U is the entrainment speed, W the applied load, η the lubricant dynamic viscosity, R' the reduced contact radius in the entrainment direction, and E' the reduced elastic modulus. The latter two terms are defined by $1/R' = 1/R_{x1} + 1/R_{x2}$ and $2/E' = (1 - \upsilon_1^2)/E_1 + (1 - \upsilon_2^2)/E_2$, respectively, where R_{x1}, R_{x2}, E_1, E_2, υ_1, and υ_2 denote the radii in the entrainment direction, the Young's moduli, and the Poisson's ratios of the two contacting bodies.

Recently de Vicente *et al.* [31], used numerical solutions to the Reynolds and elastic deformation equations to develop regression equations to predict the separate contributions of Couette and Poiseuille flow on friction coefficient in circular (ball on flat), I-EHL contact;

$$\mu_{Poiseuille} = 1.46\overline{U}^{0.65}\overline{W}^{-0.70} \tag{2.7}$$

$$\mu_{Couette} = SRR(3.8\overline{U}^{0.71}\overline{W}^{-0.76} + 0.96\overline{U}^{0.36}\overline{W}^{-0.11}) \tag{2.8}$$

Where SRR is the slide-roll ratio, defined as the ratio of the absolute value of the sliding speed, $u_s = |u_b - u_d|$, to the entrainment speed, $U = (u_b + u_d)/2$, where u_b and u_d are the surface speeds of the ball and disc, respectively. *SRR* can be given as:

$$SRR = \frac{|u_b - u_d|}{0.5(u_b + u_d)} \tag{2.9}$$

The Poiseuille component results from shear stresses arising due to the fluid film pressure gradient, $\tau_p = -(h/2)dp/dx$, where h is the local film thickness and dp/dx the pressure gradient in the entrainment direction. Poiseuille friction is present in both rolling and sliding contact. It always has a net negative value, *i.e.* it hinders the

surface moving relative to the contact. The Couette component of flow arises from the shear stresses created in the fluid film due to the surfaces moving relative to each other. Therefore, Couette forces have different sign for each surface depending upon the sign of the sliding speed. As part of the solving process de Vicente *et al.* produced their own set of numerical predictions for I-EHL film thickness;

$$h_c = 3.3\overline{U}^{0.60}\overline{W}^{-0.14}R' \tag{2.10}$$

$$h_m = 2.8\overline{U}^{0.66}\overline{W}^{-0.22}R' \tag{2.11}$$

Eq. (2.10) and (2.11) predict slightly lower film thickness values in comparison to the Dowson and Hamrock equations. Both show different dependences on the speed and load parameters although both were derived from simulations of compliant contacts. It should be noted that a small change in the power law coefficients will produce a large change in film thickness values.

Previous work on compliant contacts has also focused on the friction of dry or partially-lubricated soft/solid contacts in both rolling and sliding conditions. In these contacts it has been shown that the rolling friction arises primarily from hysteresis losses in rubber during the elastic deformation cycle. Interestingly, it was found that, with spheres, the sliding friction in a well-lubricated contact was almost the same as the rolling friction [79]. Greenwood *et al.* calculated that, for a sphere on a flat elastomeric surface, the friction coefficient due to deformation energy losses, μ_{def}, is;

$$\mu_{def} = \alpha\frac{3}{16}\frac{a}{R} \tag{2.12}$$

where α is the loss factor, a the Hertzian contact radius and R the ball radius [80]. The loss factor, $\alpha = k\pi\tan\delta$, where k is a constant and tan δ the loss tangent, is the ratio of energy dissipated to the average energy stored per cycle in a deformation process and can be estimated from the loss tangent. De Vicente *et al.* [18] assumed

the loss tangent and thus the loss factor to be constant and incorporated this deformation friction into the prediction of rolling friction coefficient across a complete Stribeck curve;

$$\mu_{rolling} = \mu_{def} + \mu_{Poiseuille} \tag{2.13}$$

This was found to give reasonably close agreement with experimental measurements. However, since α is not strictly constant [79], it is shown later in this thesis (chapter 4) that a closer fit with experimental data can be achieved by predicting the elastic properties of the viscoelastic substrate (i.e. tan δ) across a loading frequency range. The constant k is a correction factor to be found [81] and is quoted to be between 1 and 3 [18,79,81,82] although no explanation for this was found in the literature.

2.5 Conclusion

Over the last few decades, lubricated, compliant, contacts have been receiving increased academic attention. Of particular interest are biological contacts from within the foodstuffs and cosmetics industries. The employment of tribometers to study the lubricity of different bio-lubricants has developed greater understanding of their micro-rheological behaviour. This has also allowed for the development and verification of theoretical predictions of friction in the I-EHL regime. However, mechanical errors in the experimental apparatus employed by de Vicente *et al.* led to a mistaken calculation of applied load. Subsequently, the majority of MTM friction investigations have only been carried out under two applied loads, 1.3 or 3 N. The lack of results over a larger applied load range means that the robustness of Eqs. (2.8) and (2.13) is unknown. Also, previous investigations into deformation losses have assumed that the loss tangent, tan δ, is constant. This is known to be untrue

[80]. It would be useful to know the effect of change in the loss tangent has on the overall friction.

While friction investigations for lubricated compliant contacts have developed rapidly in the last few decades, experimental techniques for measuring lubricant film thickness have not. This is in marked contrast to the numerous techniques available for investigating lubricant film thickness in hard or metallic contacts. For compliant contact tribological situations, many of the methods for measuring film thickness in hard/metallic contacts are unsuitable. For example electrical techniques are restricted to hard contact investigations with non-aqueous lubricants. The application of conducting polymers would be necessary before complaint contacts under the I-EHL regime could be investigated. In recent years a few electrically-conducting polymers have been developed but these are still difficult to obtain and expensive and were not investigated in this project. Ultrasonic techniques are still under development, and are complicated by the low acoustic properties of soft materials.

Work carried out by Roberts *et al.* and Kaneta *et al.* has shown the possibilities of using optical interferometry to investigate film thickness from the nano- to the micro-scale (limited to $h < ca$ 2 μm). However, previous work has failed to acquire film thickness measurements under continuous entrainment conditions, nor have any film thickness maps been presented. There is room for a technique to be developed for thin film thickness measurements using optical interferometry. By rotating the polymeric test specimen, rather than employing a sinusoidal motion [10,71], continuous entrainment could be achieved.

For investigating thick films ($h > 2$ μm), a number of techniques could be used. Bongaerts *et al.* have shown that confocal Raman spectroscopy can be used to measure both lubricant film thickness and composition, in thick films. However, the technique is still in its infancy and obtaining measurements is time consuming. Theoretically, applying the same confocal technique, IR absorption spectroscopy could be used to measure film thickness in compliant contacts. However, both

systems suffer the disadvantage that water has a poor signal, which would greatly limit the range of usable test lubricants. Poll *et al.* demonstrated the use of magnetic resistance to measure the film thickness in compliant contacts into the hundreds of microns range. However, it is necessary to disperse magnetic particles into the lubricant. Surfactants are required to aid dispersion and protect the magnetic particle against oxidation. This greatly limits the range of research that can be carried out using such a technique, as little is known about the affect of surfactants and particulate within a compliant contact.

The most promising technique for measuring thick films in compliant contacts appears to be Laser Induced Fluorescence. Poll *et al.* have already demonstrated that LIF can be used to measure film thickness in rubber lip seals. Problems with the image capture and illumination systems used with the LIF technique have been highlighted by Sugimura *et al.* and Poll *et al.* However, since their work was carried out, technological advances have been made. With the use of EMCCD equipment high quality images and thus film thickness measurements may be achieved.

In conclusion two promising film thickness measurement techniques present themselves for development within this project; monochromatic optical interferometry for thin film investigations and laser induced fluorescence for thick films.

Chapter 3

Friction measurements in lubricated compliant contacts

This chapter describes the experimental technique used to investigate friction in lubricated compliant contacts. An experimental procedure provides a system whereby rolling and sliding friction can be measured using a mini traction machine. Results from this work are discussed in the subsequent chapter.

3.1 Introduction

The lubrication regimes for all lubricated contacts can be separated into a number of basic systems, these being boundary, mixed and hydrodynamic lubrication.

In boundary lubrication, only a very thin, if any lubricant film is present so the state of lubrication is governed by the properties of the bounding surfaces at the contact interface. The rheological properties of the bulk fluid are of minor significance, and the coefficient of friction is virtually independent of both speed and viscosity [58].

In hydrodynamic lubrication a film of entrained lubricant wholly separates the solid surfaces and the behaviour of the contact is determined by the bulk physical properties of the lubricant, such as viscosity. Hydrodynamic lubrication is analysed using Reynolds equation and the prevailing friction is due to viscous shearing and hydrodynamic forces present within the lubricant.

Elastohydrodynamic lubrication (EHL) is a special form of hydrodynamic lubrication where the elastic deformation of the contacting bodies and the changes of viscosity with pressure play fundamental roles [83]. EHL contacts generally occur in point or line contacts between bodies made of stiff materials. In these, the entire load is concentrated over a small contact area and this, combined with the stiffness of the bodies results in high contact pressures, reaching typically 2 GPa. Conventional hydrodynamic films, as formed between conforming surfaces, are unable to support such high pressures, and application of simple hydrodynamic theory predicts negligible lubricant film thickness. However, lubricant films do form in non-conforming contacts, with thicknesses comparable to the contacting surfaces' roughness. This is due to the combined effect of (i) high pressure causing local elastic deformation of the contact and (ii) high pressure greatly increasing the viscosity of the lubricant in the contact. Elastohydrodynamic lubrication is

consequently analysed using a combination of Reynolds' equation, elasticity theory and lubricant viscosity-pressure equations.

The intermediate system between boundary and hydrodynamic/elastohydrodynamic lubrication is recognised as the mixed lubrication regime [58]. Mixed lubrication regime occurs at speeds below those needed to give full hydrodynamic or EHL where the lubricant film thickness only partially separates the surfaces so that part of the applied contact load is supported by fluid pressure and part by asperity contact pressure. This regime is governed by a complex series of rules which involve interactions between the contacting surfaces and asperity tips, as well as the lubricant physical properties.

There is a little uncertainty in the location of regime boundaries, and their transition regions are ill defined. However, Fig. 3.1 shows a schematic Stribeck curve for a lubricated contact, with an approximate indication of the lubrication regimes relative positions given. Also shown is an indication of film thickness or separation of surfaces for each regime.

Lubricated compliant or "soft" contacts, where one or both contacting solids has a low elastic modulus, are present in many practical engineering and biological applications. In such contacts, the prevailing lubrication mode is Isoviscous-Elastohydrodynamic Lubrication (I-EHL). In this regime, the contact pressure is great enough to cause elastic deformation of one or both of the interacting solids. This has a significant effect on the thickness of the fluid film separating them, but the pressure within the contact is low and insufficient to cause any substantial change in fluid viscosity [4]. Unlike in hard, metal-metal contacts, rolling friction can be considerable and this originates in part from the viscoelastic properties of the compliant surfaces.

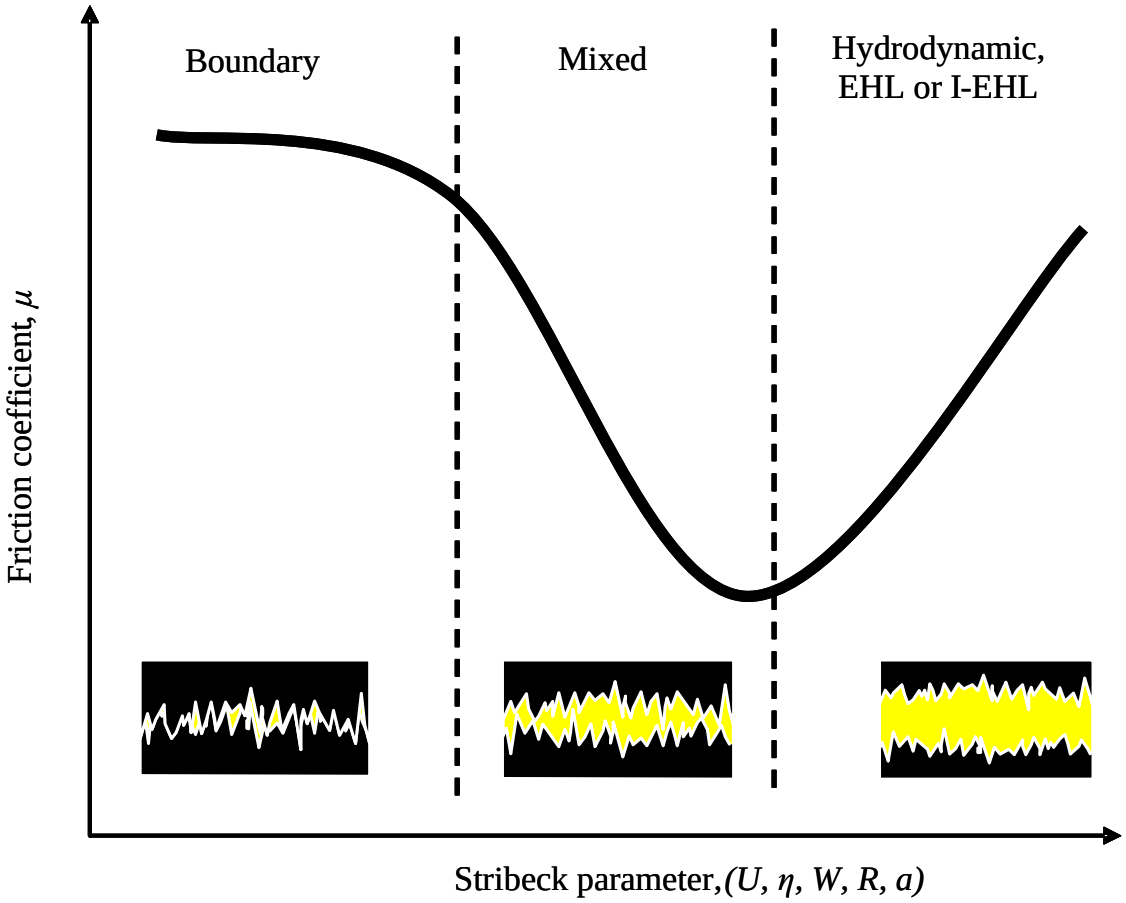

Figure 3.1 Log-Log Stribeck curve showing friction coefficient versus a function of contact conditions.

3.2 Apparatus:

Friction investigations were performed on a mini traction machine (MTM, PCS Instruments, UK), Fig. 3.2. The MTM is a flexible general purpose instrument for measuring the frictional properties of lubricated and un-lubricated contacts under a wide range of rolling and sliding conditions [40]. The control software runs on a standard PC and allows the user to easily define a test profile containing a sequence of temperatures, loads and speeds. The selected profile steps the instrument through the test sequence, recording data as required, without any intervention by the user. The original design parameters of the instrument were chosen so that high contact

pressures, temperatures and speeds could be obtained within a safe, easy to use, laboratory bench top system [84].

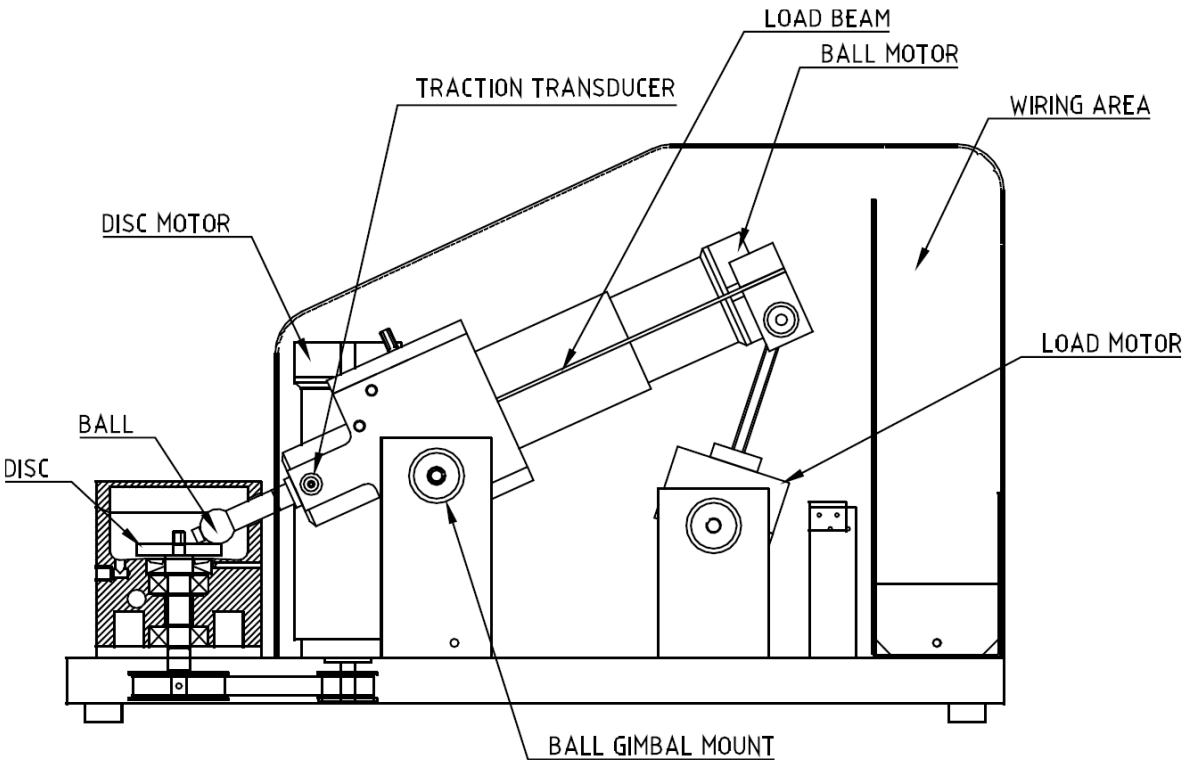

Figure 3.2. Schematic of MTM [84].

3.3. MTM development:

The material characteristics and tribological properties of compliant contacts differ from the more usual steel on steel contact. The low elastic modulus of elastomeric materials employed in the current investigations means that there is considerable elastic deformation of the specimens under low load. Also the elastic hysteresis of the materials means that there is significant rolling friction in addition to the usual sliding friction [85].

Normally, the MTM uses metal balls and discs, but in the current study, a compliant contact was obtained by loading a stainless steel ball against a polymer disc, as shown in Fig. 2.1. Recently, development of the MTM has been carried out so that accurate friction measurements under low load low pressure conditions can be obtained. The motor speeds can be controlled in both directions so that the MTM can measure the rolling as well as sliding friction. The operational mode is called 'Bi-Directional'. The loading system has been modified to enable very accurate control of the load under large deformations. The MTM software has been updated to allow greater control of load and friction results. This development work has been done in conjunction with PCS Instruments.

The following sections describe the main features of the modifications.

3.3.1. MTM principle

The test contact is formed between a polished 19.05 mm (3/4 inch) diameter steel ball and the flat surface of a polymer disk, each independently driven to produce a sliding/rolling contact. The disk specimen is mounted on a vertical shaft in a stainless steel test fluid reservoir and the ball is end-mounted on a pivoting shaft and is automatically loaded against the disc at the start of the test. DC servomotors rotate the disk with accurate speed control and the traction force applied to the ball specimen is measured with a high sensitivity force transducer [21].

Tests can be carried out at over a wide range of applied loads, temperature, and in mixed sliding-rolling conditions with a fixed slide-roll ratio, SRR. The lateral force exerted on the ball is measured through a force transducer and yields the friction coefficient, μ, which is defined as the ratio of the applied load, W and the measured friction force, f:

$$\mu = \frac{f}{W} \tag{3.1}$$

In the MTM, the friction force in a mixed rolling/sliding contact is generally obtained by taking two successive measurements from the load cell attached to the ball drive shaft, at the same entrainment speed, one with the disk surface travelling faster than the ball and one with the ball travelling faster than the disk. The friction force is then the average of the two readings. This is done to cancel any offset in the load cell. However, de Vicente *et al.* [18] noted that this method also serves to cancel any rolling friction force, since this, like the load cell offset, does not change sign with respect to the relative speeds of the surfaces [31].

3.3.2. Bi-directional mode

The MTM used in this investigation is able to separate the rolling and sliding friction components of the overall friction. This is done using the MTM operating mode called 'Bi-Directional'. In the bi-directional mode, the ball and disc can rotate in both directions. One possibility arising from this is that SRR can be greater than 200 % so higher sliding speeds can be attained. This option also allows the calculation of the rolling friction present in mixed rolling-sliding contacts [85]. For this, two further friction measurements are taken, with the ball and disc rotating at the same speeds as before but in the opposite direction. These results can be used to separate the load cell offset from the previously cancelled rolling friction since the latter changes direction when the direction of rotation of both surfaces is reversed.

Figure 3.3 shows the directions of the rolling and sliding friction force for a typical MTM contact, taken from ref [85]. The tribological contact is operating at a mean entrainment, U, of 200 mms^{-1} and SRR, of 50 %. The applied load, W, is arbitrary, while the contacting materials and lubricant are assumed to be Newtonian. The sliding friction force, f_c, is determined from:

$$f_c = 0.5\left[\frac{|TF1 - TF2|}{2} + \frac{|TF4 - TF3|}{2}\right] \tag{3.2}$$

which cancels any offset and also rolling friction.

The rolling friction force, f_p, is the difference between the rolling force in the positive direction and the force in the negative direction:

$$f_p = 0.5.\left|\frac{(TF1 + TF2)}{2} - \frac{(TF3 + TF4)}{2}\right| \tag{3.3}$$

which cancels any offset and also any sliding friction.

The sliding or rolling friction coefficient is calculated by using Eq. (3.1) with (3.2) or (3.3) for sliding or rolling respectively.

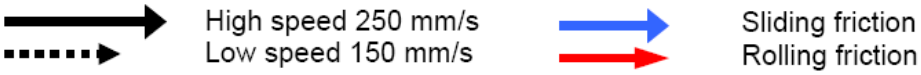

Umean	SRR	Traction force
200	50	TF1
200	-50	TF2
-200	50	TF3
-200	-50	TF4

Figure 3.3. An example of a traction measurement from ref [85].

3.3.3. Loading system

The MTM uses a displacement load system applied via a leaf spring load beam, controlled by a load motor located at the rear of the MTM, as shown in Fig. 3.2. Calibration of the load motor is carried out before testing, using a steel calibration ball and disk. A zero load ('just touching') position is located by the MTM before a calibration weight lifts the ball and disk out of contact. The subsequent

displacement applied by the load motor to achieve 'just touching' contact conditions again, is recorded. The MTM now takes the two measured values; displacement for zero load from the 'rest' position, and displacement required to apply the calibration load from the zero load position and extrapolates all subsequent loads from these two values. For compliant contacts an offset is applied by the MTM software to take into account the increased contact deformation and lower elastic modulus of the test specimen compared to 'hard', metallic specimens.

However, this method for loading non-compliant, or 'hard' metallic materials, was demonstrated by Bongaerts *et al.* [25] to be inadequate for compliant contacts. For a desired load of 3 N an induced error of *ca* 1.7 N was found to occur. Bongaerts *et al.* demonstrated that, to improve the loading system the load beam, a 2 mm thick leaf spring, should be replaced with a thinner, 1 mm leaf spring and fitted with a feedback strain gauge.

The new system has a load range of 0.01 to 10 N. This allows the loading steps to be 0.01 N per step as opposed to 0.07 N in the previous system, giving greater control and accuracy of the applied load. The load applied to the contact is measured by the strain gauge, installed on the load arm. This is checked to fit within pre-set load tolerances (within the mtm.ini file); normally two magnitudes lower than the desired applied load. A new load calibration menu allows the user to perform two separate calibrations for the loading system of both the load motor and the strain gauge. This allows the user to manually set the zero load, or 'just touching', position and re-set the stain gauge and stepper motor reading to correspond with this point. This manual calibration of the zero point compensates for small changes in dimensions between the calibration apparatus and test specimens.

For each test the load motor step position and strain gauge load are stored in the file \mtm\OUTLOAD.txt. Figures 3.4 and 3.5 give the load motor step position and the applied load, from the strain gauge, for two standard entrainment speed range tests. Figures 3.4 and 3.5 demonstrate the improvements made to the loading system in recording the actual load and maintaining a constant load. The tribological contact

was formed between a soft elastomer disc and stainless steel ball. The MTM test profile was programmed for 1 N applied load across an entrainment speed range of 0.001 to 1 ms^{-1}. The temperature and SRR were fixed at 35 °C and 50 % respectively.

In Fig. 3.4, the surfaces were lubricated with pure glycerol and under these conditions the contact will have been operating in the isoviscous elastohydrodynamic lubrication regime. An average load of 0.92 N, across the entire test period, was observed, which satisfies the preset load tolerances of 0.1 N. A constant displacement, of *ca* 2270 steps, was maintained by the load motor, suggesting that the applied load was also constant through out the entire test. However, the actual load, measured by the strain gauge and plotted as a red solid line, did not remain constant across the entire entrainment speed range. The noise in the load increased as U was increased and a resultant small climb in the average applied load is observed. This was probably due to an increase in MTM vibration which is visible at entrainment speeds greater than *ca* 0.6 m s^{-1}. Another possibility is a variation in load due to changing hydrodynamic forces in the lubricant. Once the surfaces are completely separated so that the contact is operating within the I-EHL regime, which occurs at *ca* U = 25 mm s^{-1} under the given operating conditions, the load is borne by the lubricant layer. Changes to this fluid thickness due to vibrations or changes in entrainment direction, however small, will result in fluctuation in applied load.

The addition of the strain gauge allows the user to record the error between actual and desired or input applied load. In the case of Fig. 3.4 an error of *ca* 6 % would be induced in the calculated friction coefficient if the input load and not the true load were used in Eq. (3.1).

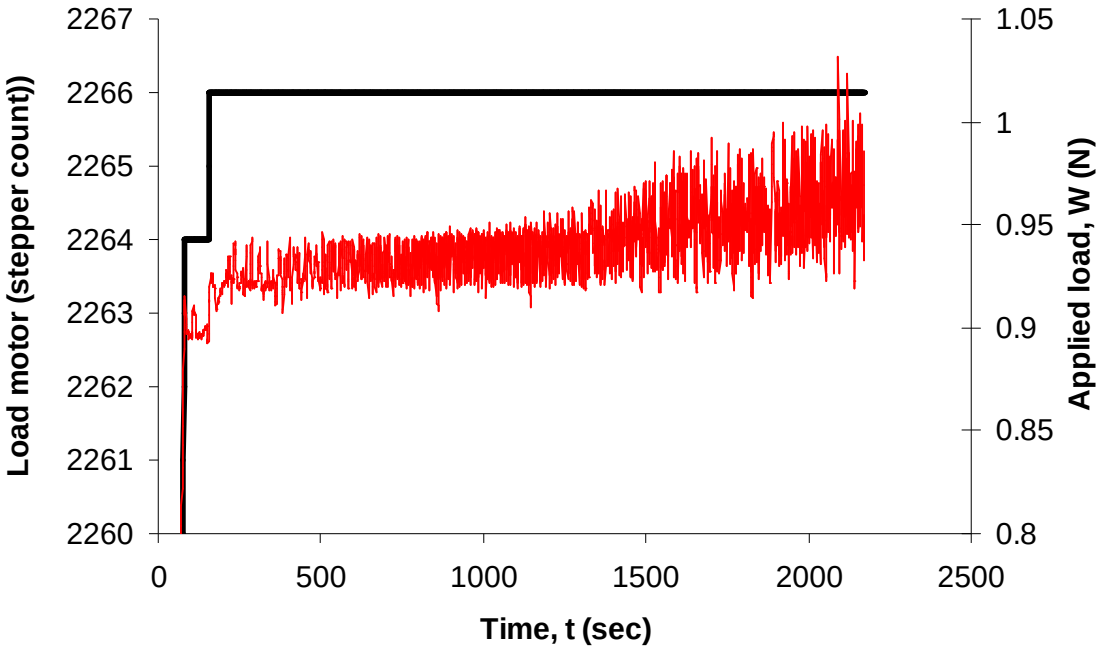

Figure 3.4. Load motor step position (black) and strain gauge load reading (red) across test period. For an elastomer/steel tribo pair, lubricated with glycerol under 1 N applied load, across an entrainment speed range of 0.001 to 1 m s^{-1}.

The test conditions for Fig. 3.5 were the same as Fig. 3.4 except the contact was lubricated with water. Under these conditions the contact will have been operating in the boundary and mixed lubrication regimes. Again an average applied load of *ca* 0.92 N is observed which fits within the preset load tolerances. A relatively constant load was maintained throughout the test. However, unlike the example above, the applied load can be seen to slowly decrease towards 0.9 N. Each time the load converges on this value, the limit of the preset load tolerances, the load motor step count increases. This occurs 6 times within the test period. A possible cause for the change in load is wearing of the elastomer surface. As with the example above, an error of *ca* 6 % would be induced in the calculated friction coefficient if the input load is used instead of the actual load. The feedback loop between the strain gauge and load motor allow for the applied load to be adjusted during testing, correcting any error arising from changes in specimen geometry.

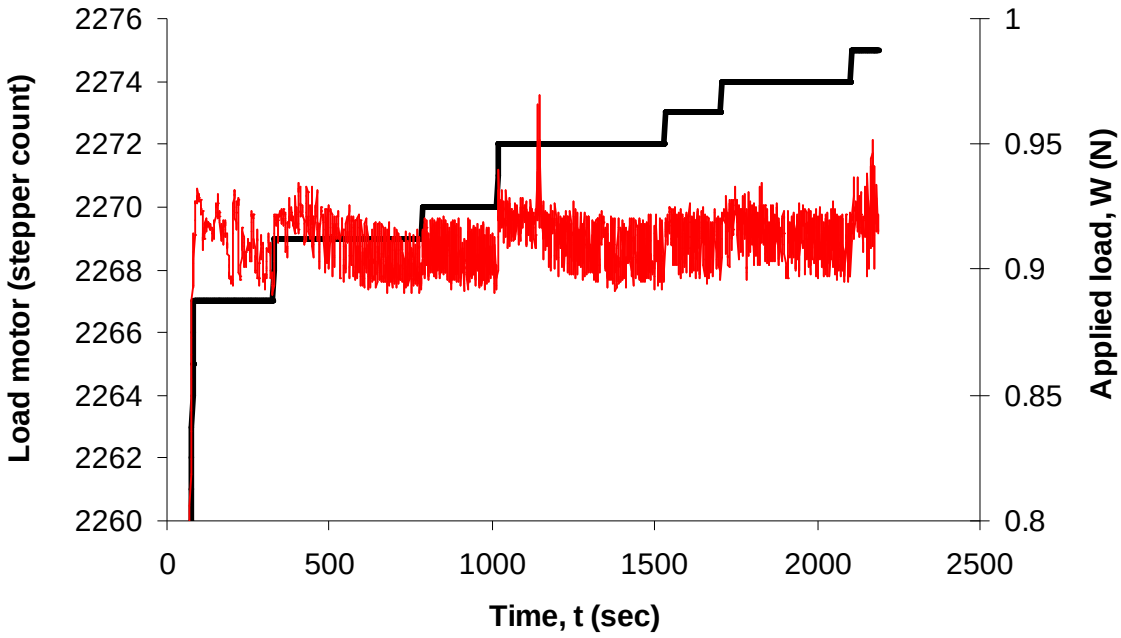

Figure 3.5. Load motor step position (black) and strain gauge load reading (red) across test period. For an elastomer/steel tribo pair, lubricated with water under 1 N applied load, across an entrainment speed range of 0.001 to 1 ms^{-1}.

3.3.4. Software modifications

When operating in Bi-directional mode, the MTM takes four measurements or 'steps' to calculate the sliding and rolling friction coefficient. For each step the contact is loaded and un-loaded, but the load for the first step is carried through for each of the three subsequent steps. This can create an error in the calculated friction coefficient if the actual applied load varies across the four steps. As shown above, there is often an error between desired load and the actual load. To reduce this error the software was modified so that the applied load for each step was recorded and the friction coefficient for each step was calculated before giving an average friction coefficient value. The friction coefficient values for each step were, also, used to calculate the sliding and rolling friction components.

Improvements were also made to the way the MTM records friction force and applied load for each step. Friction force and applied load were measured over a set time period, which means at high speeds a load will be taken over a number of ball rotations. However, at low ball speeds (< 25 mms^{-1}), loads were recorded over a fraction of ball rotation. This restricted the MTM to high speed investigations only, not suitable for this project. Low speed studies could be carried out but large amounts of scatter were present in the results. The software logging rate has now been changed to log over at least one complete revolution at low speeds. The logging rate is calculated to obtain 200 points over 5 revolutions of the ball (or revolutions of the disc when operating in 'pin on disc' mode). There is, however, a time limit of 2 s which means the traction is logged over less than one revolution at speeds lower than 9 mm s^{-1}. This new logging system is summarised in table 3.1.

Table 3.1: *Logging rates across speed range.*

Ball speed (mm/s)	**Number revs logged**	**Notes**
> 135	5	Standard logging rate
< 135, > 9	1	New feature
< 9	Less than 1 – Log Rate mini = 35 pts/s	Example: for 5 mm/s, data logged over 0.5 revs

3.4. Experimental preliminaries

3.4.1. Test lubricants

Table 3.2 lists the main lubricants employed in this study and their dynamic viscosities at the test temperature. The lubricant viscosities were measured using a Stabinger Viscometer (Anton Paar, UK).

Table 3.2. *Dynamic viscosities of Test Lubricants*

Lubricant	Composition	Viscosity at 35 °C (Pas)
Water	**Demineralised water**	**0.00075***
GLY75	**75 wt.% Glycerol in water**	**0.017**
GLY	**Glycerol**	**0.382**
CS	**95 wt.% Pure Corn Syrup in water**	**2.45**

* The viscosity for distilled water was obtained from Douglas *et al.* [86].

All test lubricants are single phase and Newtonian in the range of shear rates between 1 to 1000 s^{-1}, which satisfies the test parameters. They were chosen to span a very wide range of viscosities. Lubricant viscosities were measured prior to testing, at test temperature, T = 35 °C. All water used for testing and in solutions was demineralised filtered water (Elga). Glycerol was supplied as 98 % pure grade (Sigma Aldrich), while the Corn Syrup was supplied by Unilever Ltd.

3.4.2. Material selection

For the majority of research into lubricated, compliant contacts, crosslinked polydimethyl siloxane (PDMS) is used as the soft substrate. PDMS is utilized as one or both of the contacting surfaces in the tribological contact to maintain low contact pressures and create the conditions for I-EHL to occur. One key property of PDMS is its ease of fabrication, which has contributed to its widespread use. Prior to crosslinking, PDMS can be cast into suitable moulds of almost any desired shape. Other attractive features of PDMS include its physiological inertness, availability, low unit cost, as well as its good thermal and oxidative stability.

PDMS is a polymer with an inorganic backbone consisting of alternating silicon and oxygen atoms, with each silicon bearing two methyl(-CH_3) groups. The introduction

of functional groups into PDMS, which partly replace the methyl moieties, as well as the utilization of other functional siloxanes, enables the formation of a silicone elastomer via chemical crosslinking. Since crosslinked PDMS elastomers exhibit inherently weak mechanical properties, so reinforcing fillers such as silica are usually incorporated in commercial silicone rubbers. To be able to compare measurements taken in this investigation to earlier work by de Vicente *et al.* [18], the PDMS used in this study is the same. The PDMS was supplied by NDA Engineering Equipment Limited (UK), as a white sheet, 4.5 mm thick. Topographical analysis of the surface using a scanning electron microscope (SEM), Fig. 3.6, reveals a complex structure due to the presence of the filler material. Through spectrum analysis of the SEM images, the filler was identified as magnesium oxide, which had previously been quoted, incorrectly to be titania crystals [25].

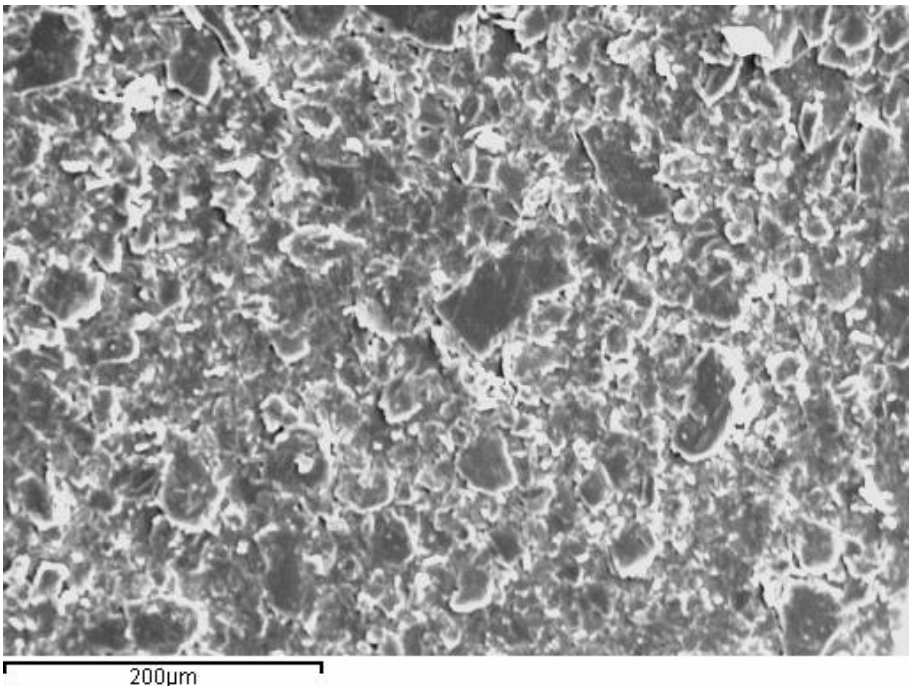

Figure 3.6. SEM image of PDMS used for MTM testing.

The effect of elastic modulus on the frictional characteristic in a lubricated compliant contact is investigated in chapter 4, where PDMS plus two other polymers are used to give a wide range of elastic moduli. The two other polymers were Low-density

Polyethylene (LDPE) and Polycarbonate (PC). Both polymers were supplied in sheet form, 4.5 mm thick, by eSheet Ltd (UK).

LDPE is a thermoplastic polymer, derived from Polyethylene, consisting of long chains of the monomer ethylene. LDPE was originally prepared some fifty years ago by the high pressure polymerization of ethylene. Its comparatively low density arises from the presence of a small amount of branching in the chain (on about 2% of the carbon atoms). This gives a more open structure than a wholly linear structure. LDPE is chemically inert, insolvent at room temperature in most solvents and has a good resistance to acids and alkalis, although exposure to light and oxygen results in loss of strength and loss of tear resistance. All of this makes LDPE a useful and widely-used plastic, for example in squeeze bottles or plastic bags.

Polycarbonate is another thermoplastic consisting of long-chain linear polyesters of carbonic acid and dihydric phenols, such as bisphenol A. Polycarbonate consists of two phenyl groups and two methyl groups bonded to a carbon molecule. The presence of the phenyl groups on the molecular chain and the two methyl side groups contributes to molecular stiffness in the polycarbonate. This stiffness has a large effect on the physical properties of polycarbonate. First, attraction between the phenyl groups of different molecules contributes to a lack of mobility of the individual molecules. This results in good thermal resistance but relatively high viscosity (*i.e.*, low melt flow) during processing. The inflexibility and the lack of mobility prevent polycarbonate from developing a significant crystalline structure. This lack of crystalline structure (the amorphous nature of the polymer) allows for light transparency. Polycarbonate is naturally transparent, with the ability to transmit light nearly that of glass. It has high strength, toughness, heat resistance, and excellent dimensional and colour stability.

The main mechanical properties and sources of the three polymers are listed in table 3.3, along with their average surface roughness values. Material property values for LDPE and Polycarbonate were taken from ref. [87]. The surface roughness of all three polymers was determined using a Wyko optical interferometer (Veeco, UK).

Measurements were taken in the VSI mode and the camera was setup with a X20 objective lens. Images were 640 x 450 pixels, which equates to a field of view of *ca* 575 x 430 μm. No filtering was used during all measurements.

Table 3.3. *Material properties of test polymers.*

Polymer (Source)	**Young's Modulus, E (GPa).**	**Poisson's Ratio, υ**	**Surface roughness, R_a**	**Peak to valley height**
PDMS (NDA Engineering Equipment Limited, UK)	**0.005***	**0.49 [16]**	**790 ± 100 nm**	**2 μm**
LDPE (eSheet Ltd)	**0.227**	**0.4**	**65 ± 10 nm**	**150 nm**
Polycarbonate (eSheet Ltd)	**2.38**	**0.36**	**25 ± 5 nm**	**750 nm**

* Denotes values obtained by DMA analysis at 35 °C.

The three polymers were selected to span several orders of magnitude of elastic modulus while creating the correct conditions for I-EHL to occur. Figure 3.7 shows the test parameters positioned within a hydrodynamic lubrication regime map for a circular contact. This map, taken from [4], identifies the four regimes of hydrodynamic lubrication in terms of two variables, the non-dimensional viscosity parameter, g_V and the non-dimensional elasticity parameter, g_E defined by;

$$g_V = \frac{\overline{G}\,\overline{W}^3}{\overline{U}^2} \tag{3.4}$$

$$g_E = \frac{\overline{W}^{\frac{8}{3}}}{\overline{U}^2} \tag{3.5}$$

where $\overline{G} = \beta E'$ and β is the lubricant pressure viscosity coefficient and the dimensionless operating parameters are defined by Eqs. (2.5) and (2.6). A value of β of 0.5×10^{9} Pa^{-1} was assumed for all test fluids [31].

It can be seen that, so long as $U\eta$ is large enough to generate a thick film, the polymer discs should operate in the isoviscous-elastic regime for almost all conditions tested. At the highest $U\eta$ values, PC and LDPE operate within the isoviscous-rigid regime. As the contact moves towards the I-R regime it is believed that the minimum film thickness moves from the rear of the contact to the side-lobes, until it operates fully within the I-R regime, where the central and minimum film thickness will be equal [31].

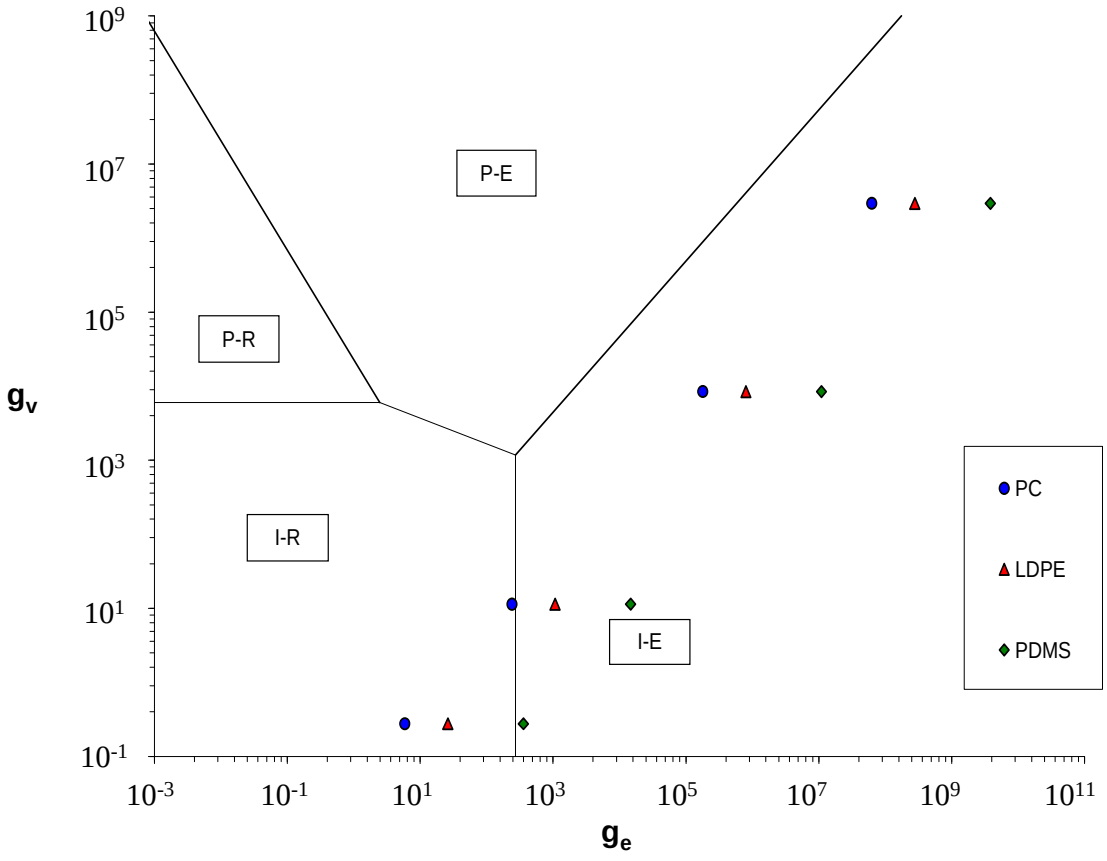

Figure 3.7. Fluid lubrication regime map showing range covered in the experimental measurements. The labelled regions represent the lubrication regimes Piezoviscous-rigid, P-R, Piezoviscous-elastic, P-E, Isoviscous-rigid, I-R and Isoviscous-elastic, I-E.

3.4.3. Determination of viscoelastic properties

The viscoelastic properties of the polymers employed in this study were measured using a general viscoelastic evaluation method, Dynamic Mechanical Analysis (DMA). A Tritec 2000 DMA (Triton Technology Ltd.) was used to measure the viscoelastic properties of the test polymers. The polymer sheets were cut into rectangular samples, 3 x 3 mm cross section and 10 mm in length. A sample was then mounted in an environmental chamber, with a temperature range from -150 °C to 400 °C. The maximum load for this system is 10 N and maximum driveshaft travel is 1 mm. The Tritec 2000 DMA has a built-in cryogenic cooling capability which is extremely simple to use and has low liquid nitrogen consumption. In addition, the Tritec 2000 DMA has an optical window as standard which allows the sample to be viewed throughout the experiment (Fig. 3.8). All tests were carried out in tension deformation mode, mounted in the standard horizontal orientation.

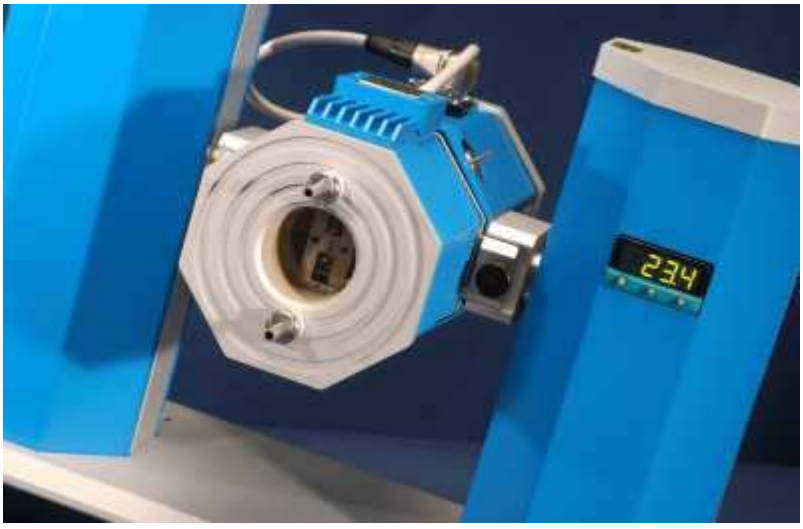

Figure 3.8. The Tritec 2000 DMA

DMA works by applying an oscillating force to a sample of material and measuring the resulting displacement. The sample deforms under the load and from this the stiffness of the sample can be determined and the sample's elastic properties can be calculated. By measuring the time lag in the displacement compared to the applied force, the damping properties of the material can also be determined.

The frequency range of interest for the polymer samples used in this investigation was between 0.5 to 3000 Hz (see chapter 4.2.4 for explanation). However the Tritec 2000 DMA employed was limited to low frequency measurements of 0.01 to 50 Hz. To determine Young's modulus and tan delta values at higher frequencies, a time-temperature conversion technique can be used [88-90]. Above the glass transition temperature, T_g, the stress relaxation and the creep behavior of amorphous polymers obey the Time Temperature Equivalence Principle, (TTEP) [91]. This states that a viscoelastic material's time and temperature response are equivalent to the extent that property data at one temperature can be superimposed upon data taken at a different temperature, merely by shifting curves. In the 1950s Williams *et al.* [92] demonstrated the validity of this principle and showed that, with their model (WLF), that it is possible to convert elastic data at widely different temperatures to a single curve spanning many decades of frequency or time at some reference temperature. This is done via a shift factor (which is an integrated form of the Arrhenius equation) to transpose a higher temperature mechanical response profile to an equivalent longer time behavior at a lower temperature. This equation is:

$$log a_T = \frac{-C_1(T - T_o)}{C_2 + (T - T_o)} \tag{3.6}$$

where a_T is the acceleration factor and log a_T is referred to as the "shift factor" which is a function of temperature but not a function of time. C_1 and C_2 are constants that vary from polymer to polymer, T is the actual temperature of experiment, and T_o is the temperature of interest (designated as the reference temperature or, as often used, the glass transition temperature T_g). Tanner [93] notes that the WLF model is widely applicable to amorphous polymers in the range T_g to T_g + 100 °C. The glass

transition temperatures for the polymers employed in this investigation were -120, -105 and 145 °C for PDMS, LDPE and PC respectively. The temperature of interest in this investigation was 35 °C; therefore, all three materials lie somewhat outside of the range suggested by Tanner. Despite this, an extrapolation method was applied to data from frequency sweeps (0.1 – 50 Hz) at 35 °C, and then used to predict the elastic modulus and loss tangent at high frequencies. Results from this part of the investigation are described in chapter 4.

3.5. Basic Stribeck curves

Figures 3.9(a) and (b) show sliding and rolling friction coefficient respectively, plotted on a log-log friction coefficient *versus* entrainment speed for all the lubricants tested with PDMS. Tests were carried out at an applied load of 3 N, over an entrainment speed range of 5 to 1200 mm s^{-1}. There is little apparent correlation between the various test lubricants. However, if the same friction coefficients values are plotted against the product of entrainment speed and dynamic viscosity, $U\eta$, it can be seen that they collapse to form single curves. This is shown in Figs. 3.10(a) and (b), with the main lubrication regimes superimposed. The sliding friction plot now resembles the highly-recognisable Stribeck curve.

At speeds greater than $U \approx 600$ mm s^{-1}, it was found that the MTM ball became unstable and started to bounce, which caused the coefficient of friction to drop off in the isoviscous-EHL regime. This decrease in friction coefficient is seen in both the sliding and rolling results. Due to this mechanical limitation, entrainment speeds analysed were limited to a range of 5 to 600 mm s^{-1}.

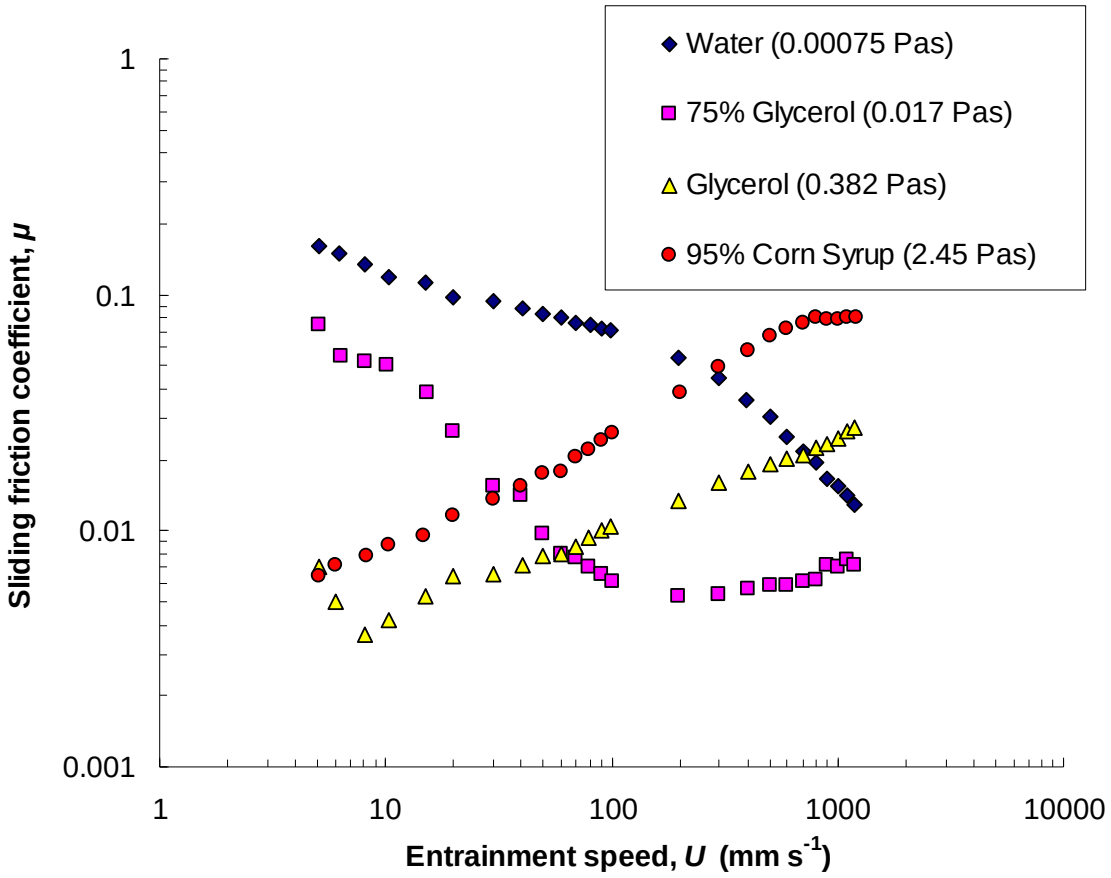

Figure. 3.9(a) Plot of log (sliding friction coefficient) versus log (entrainment speed) for a range of different viscosity lubricants at 50% SRR with a PDMS disk

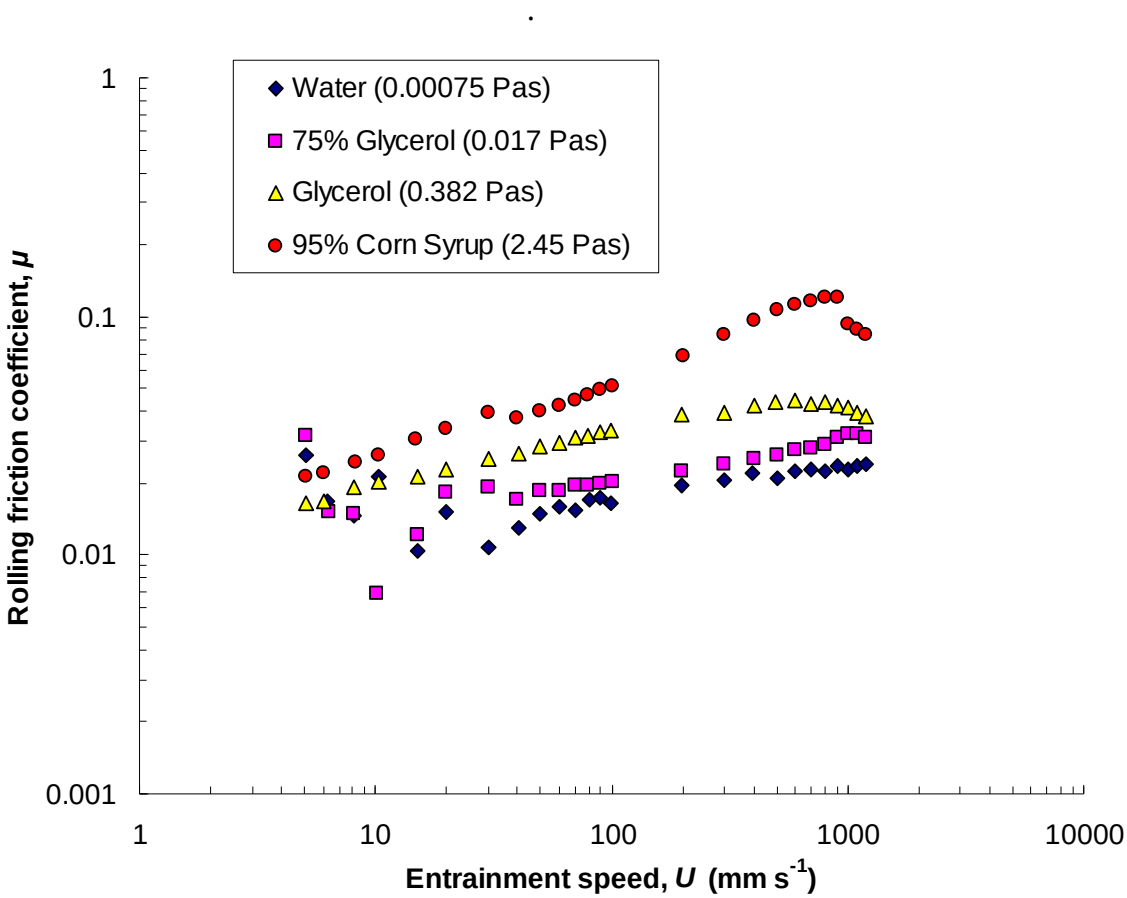

Figure. 3.9(b) Plot of log(rolling friction coefficient) versus log(entrainment speed)) for a range of different viscosity lubricants at 50% SRR with a PDMS disk.

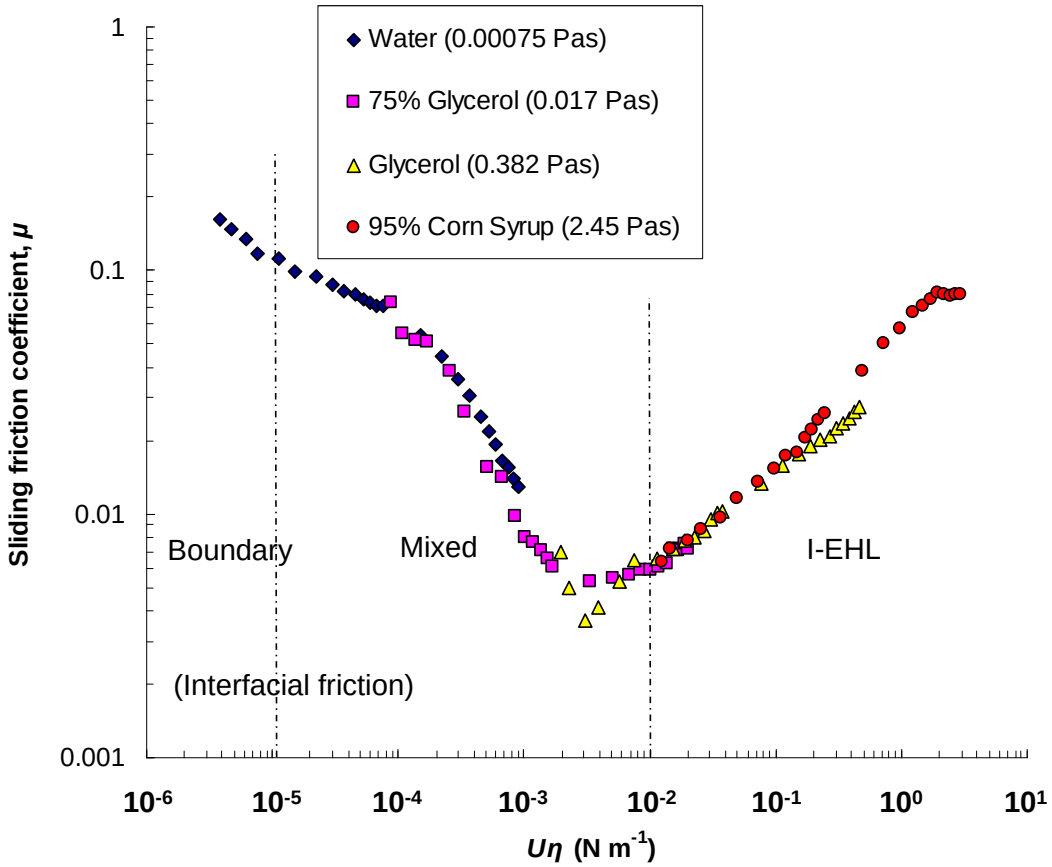

Figure. 3.10(a) Plot of log(sliding friction coefficient) versus log(entrainment speed x viscosity) for a range of lubricants at 50% SRR, with a PDMS disk.

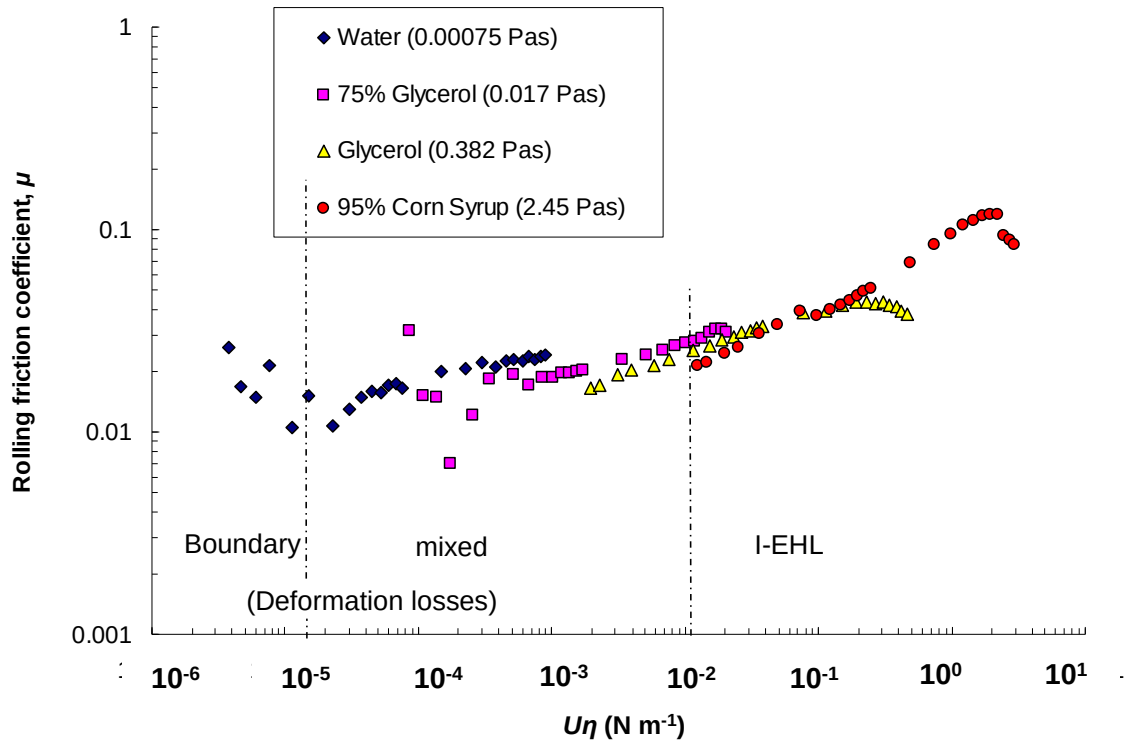

Figure. 3.10(b) Plot of log(rolling friction coefficient) versus log(entrainment speed x viscosity)) for a range of lubricants at 50% SRR, with a PDMS disk.

Chapter 4

Influence of load and elastic modulus on the rolling and sliding friction

In this chapter the influence of both applied load and elastic modulus on the friction in a lubricated, compliant contact between rubbing surfaces is investigated. Friction measurements are made over a wide range of entrainment speeds and lubricant viscosities and processed to generate separate sliding and rolling Stribeck friction curves. Further analysis of the applied load demonstrates the effect of loading frequency on the rolling friction within the boundary and mixed lubrication regime.

Work presented in this chapter can be found in; Myant C, et al. "Influence of load and elastic properties on the rolling and sliding friction of lubricated compliant contacts". Tribology International 43 (2010) 55–63. doi:10.1016/j.triboint.2009.04.034

4.1. Test conditions and procedure

The purpose of these MTM investigations was to determine the effect of applied load and the elastic modulus of the contacting materials on the sliding and rolling friction coefficient over a range of operating conditions. The required information, extracted from the MTM, was the friction force measured as the lateral force on the MTM ball. The results allow the accuracy and robustness of numerical predictions made by de Vicente *et al.* [31] to be verified. To enable comparison between experimental measurements and theoretical predictions made by de Vicente *et al.*, the same test conditions, lubricants and contacting materials were employed. A secondary objective was to demonstrate the effect that loading frequency has upon the rolling friction coefficient, due to the viscoelastic nature of the compliant substrate.

The tribological contact was formed between a stainless steel ball and an elastomer disc. The ball was a MTM standard test ball (AISI 440) 19.05 mm in diameter, provided by PCS Instruments. The surface roughness, *Ra*, of the steel ball used in the study was 10 ± 2 nm. To investigate the effect of applied load, the ball was loaded against a PDMS disc at four applied loads of 0.5, 1, 3, and 5 N. The MTM preset load tolerance was set to ± 0.05 N for all tests. To investigate the effect of elastic modulus, LDPE and PC were also tested under 3 N applied load. All tests were carried out at a fixed temperature of 35 ºC, and in mixed sliding-rolling conditions with a fixed SRR of 50%. As discussed in chapter 3, due to a mechanical limitation to the MTM friction testing was limited to an entrainment speed range of 5 to 600 mm s^{-1}.

The MTM discs were created by punching, for PDMS, and cutting, for LDPE and PC, the required size and shape from polymer sheets. Details of the polymers are given in chapter 3. All discs were 46 mm diameter and 4.5 mm thick. These were clamped on top of a supporting, stainless steel disc (Fig. 3.3). To reduce the variation in surface roughness values between the different polymer discs (listed in

table 3.3), the LDPE and PC were roughened. This was done using a large particle-size rubbing compound (Farécla Products Ltd). Surface roughness values where determined using a Wyko optical interferometer (Veeco, UK). These are summarised in table 4.1.

Table 4.1: *Surface topography properties of test specimens.*

Polymer	**Surface roughness, R_a**	**Peak to valley height**
PDMS	790 ± 100 nm	2 μm
LDPE	520 ± 30 nm	1.7 μm
PC	440 ± 50 nm	1.2 μm

There was a small difference in the R_a values between the three polymers. However, the I-EHL regime was the main lubrication regime of interest. Within this regime the surfaces are fully separated and then the surface roughness should have little bearing on the overall friction coefficient.

The test protocol was as follows:

- A new polymer disc was used for each test and was cleaned by successively rinsing in distilled water, 2% wt. sodium dodecylsulphonate solution and distilled water, followed by immersion in isopropanol in an ultrasonic bath for three minutes.
- The polymer discs were naturally hydrophobic and were used in this state.
- The steel ball was ultrasonically-cleaned in toluene, followed by acetone.
- The test rig was then assembled and ~ 40 ml lubricant added to completely immerse the disc.
- Temperature was stabilized while rotating the disc and ball in a no-load condition.

- Load was then applied and friction measured at a series of entrainment speeds, beginning from a low value and increasing this in stages.

4.2. Results and Discussion

The entrainment speed was varied while the slide-roll ratio was held fixed. This produced mixed sliding rolling conditions. As described in chapter 3, by varying the relative speeds and directions of ball and disc it was possible to separate the sliding and rolling friction contributions at any test conditions. The results below are discussed in terms of sliding and rolling friction separately, in subsequent sections.

4.2.1. Sliding friction results

Friction tests were carried out on a PDMS disc at loads of 0.5, 1, 3 and 5 N to explore the influence of applied load. Figure 4.1.a) shows that sliding friction was strongly dependent on applied load across all lubrication regimes, including the I-EHL regime, as predicted by Eq. (2.8). The solid lines in Fig. 4.1.a) show the predictions of this equation at each applied load. The elastic modulus of PDMS was taken to be 5 MPa for all loads and entrainment speeds. This gave a reduced elastic modulus of 13.2 MPa and Hertz radii of 0.81, 1.02, 1.48 and 1.76 mm for loads 0.5, 1, 3 and 5 N respectively. The agreement between prediction and experiment was quite good. In practice, friction coefficient in the fluid film regime appears to depend on $\sim W^{-0.5}$ as shown in Fig. 4.1.b). This relatively large exponent suggests that a considerable proportion of the friction arises from outside the Hertzian region [31].

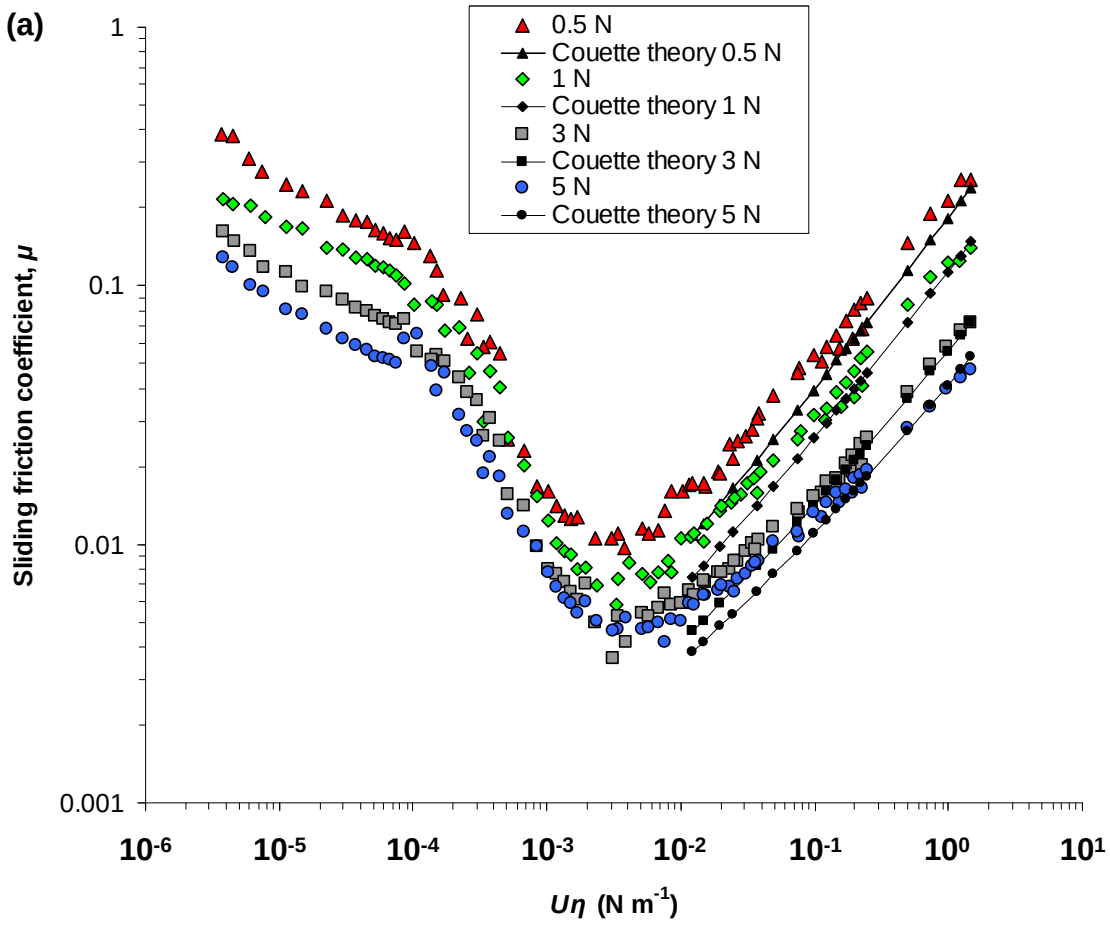
(a)
0.5 N
Couette theory 0.5 N
1 N
Couette theory 1 N
3 N
Couette theory 3 N
5 N
Couette theory 5 N
Sliding friction coefficient, μ
1
0.1
0.01
0.001
10-6
10-5
10-4
10-3
10-2
10-1
100
101
Uη (N m-1)

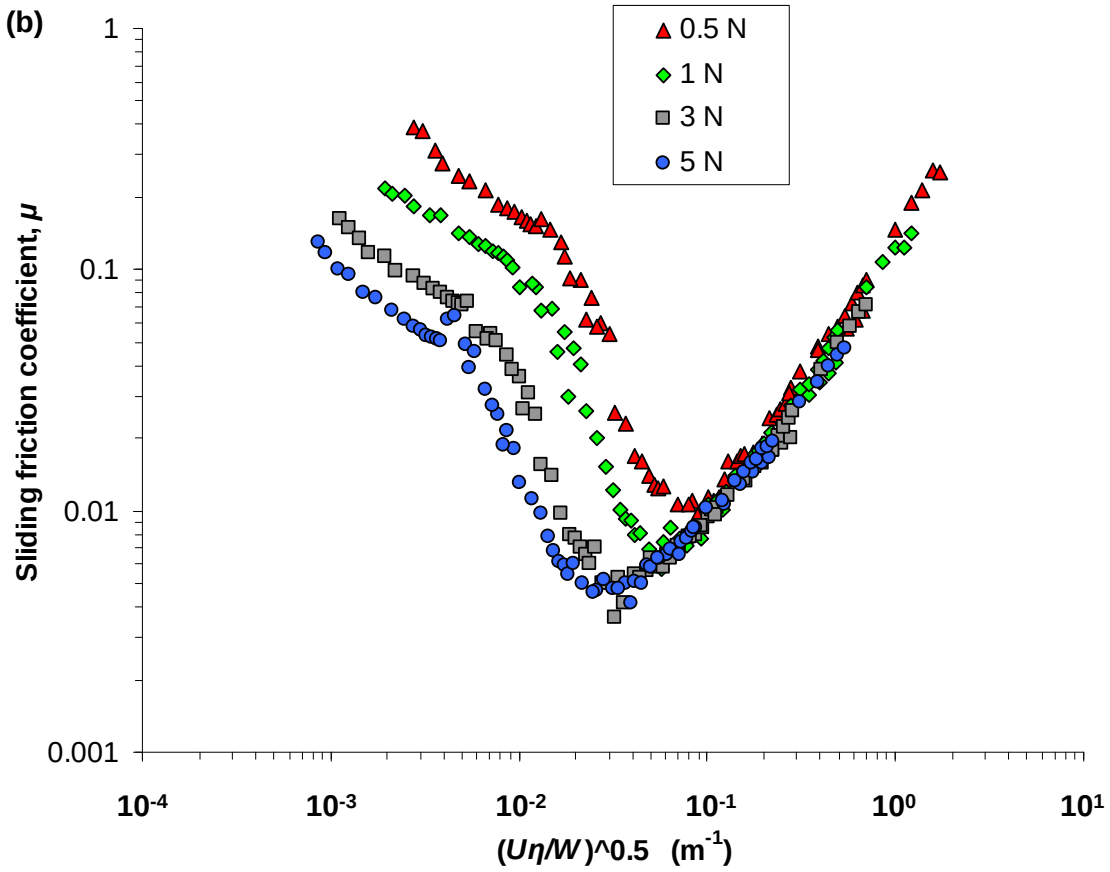

Figure 4.1 (a) and (b) Influence of load on sliding friction coefficient. Solid lines show theoretical predictions of Couette friction coefficient from Eq. (2.8).

In the boundary and mixed lubrication regimes, the friction coefficient increases with decreasing load. This is as expected for highly compliant surfaces, where the area of contact is determined by elastic conformity rather than plastic deformation at asperities. The theoretical Hertz area of contact is proportional to $W^{2/3}$. Thus, assuming the friction force is proportional to the real area of contact and that this is proportional to the Hertzian area, the friction coefficient $\mu = F/W$ will be proportional to $W^{2/3}/W$, i.e. $\mu \propto W^{-1/3}$. Figure 4.2 shows the experimentally-measured influence of load on the sliding friction coefficient in the boundary ($U\eta$ = 10^{-6} to 10^{-4}) and mixed ($U\eta$ = 10^{-4} to 10^{-3}) lubrication regime. A power law gradient of -0.55 and -0.46 was obtained for boundary and mixed regimes respectively. Considering the limited load range examined, these indices are not too dissimilar to

those expected. Their higher magnitude may indicate that the sliding friction coefficient is still influenced by asperity interaction even within a highly compliant contact.

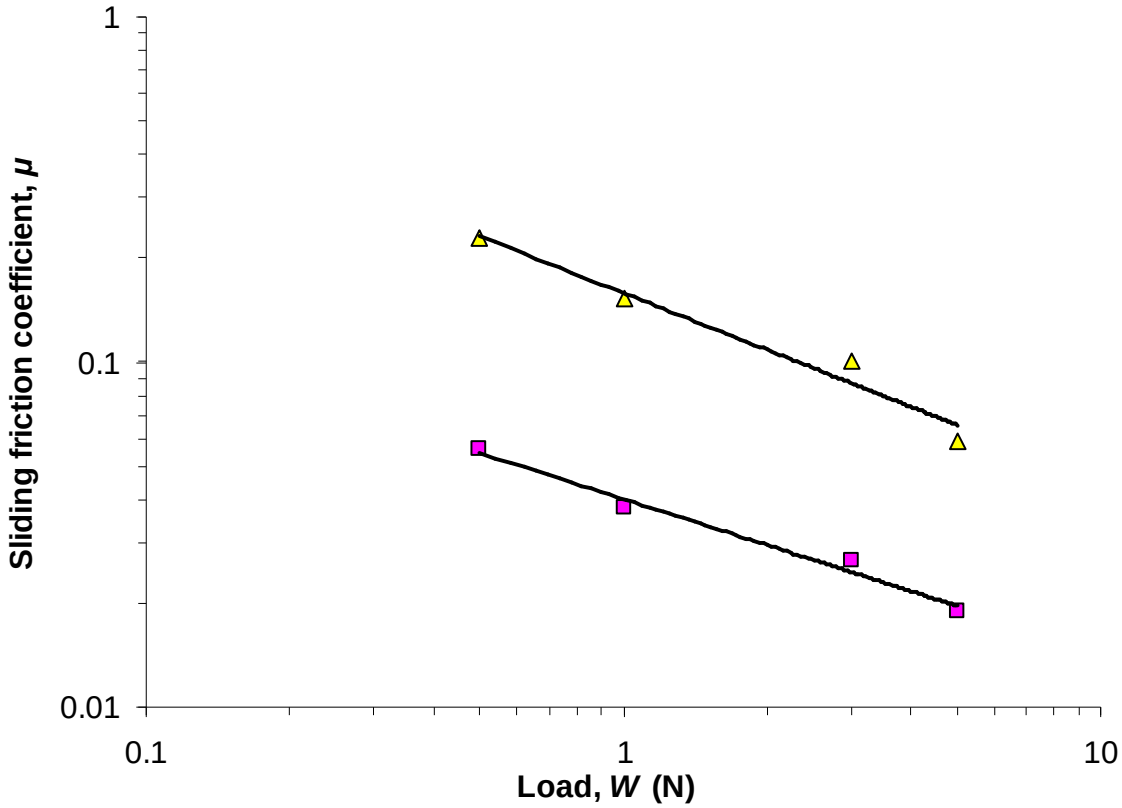

Figure 4.2 Load versus sliding friction coefficient in the boundary (triangles) and mixed (squares) lubrication regime. Solid lines show power law lines of best fit.

Friction tests were also carried out at a constant applied load of 3 N with all three polymers discs listed in table 4.1, to explore the influence of elastic properties on sliding friction. Figure 4.3 shows the sliding friction results for the three polymers at 3 N applied load, together with the isoviscous-elastic Couette friction coefficients predicted from Eq. (2.8) plotted as dashed or solid lines. In the I-EHL regime, surface roughness has little or no effect on the sliding friction coefficient. However, within the boundary and mixed lubrication regimes the surface interactions (such as surface physical-chemical interactions, surface roughness, elastic properties etc.) affect the friction coefficient. Bongaerts *et al.* [25] and de Vicente *et al.* [31] investigated the effect of surface roughness on a steel-PDMS tribo-pair and showed

that as surface roughness increases, boundary friction coefficient decreases. This is to be expected as the real area of contact decreases with increasing surface roughness, this trend is observed in Fig. 4.3. However, at greater surface roughness values, where mating of surfaces are possible, then an increase in real contact area may occur, thus a resultant increase in the friction coefficient would be expected.

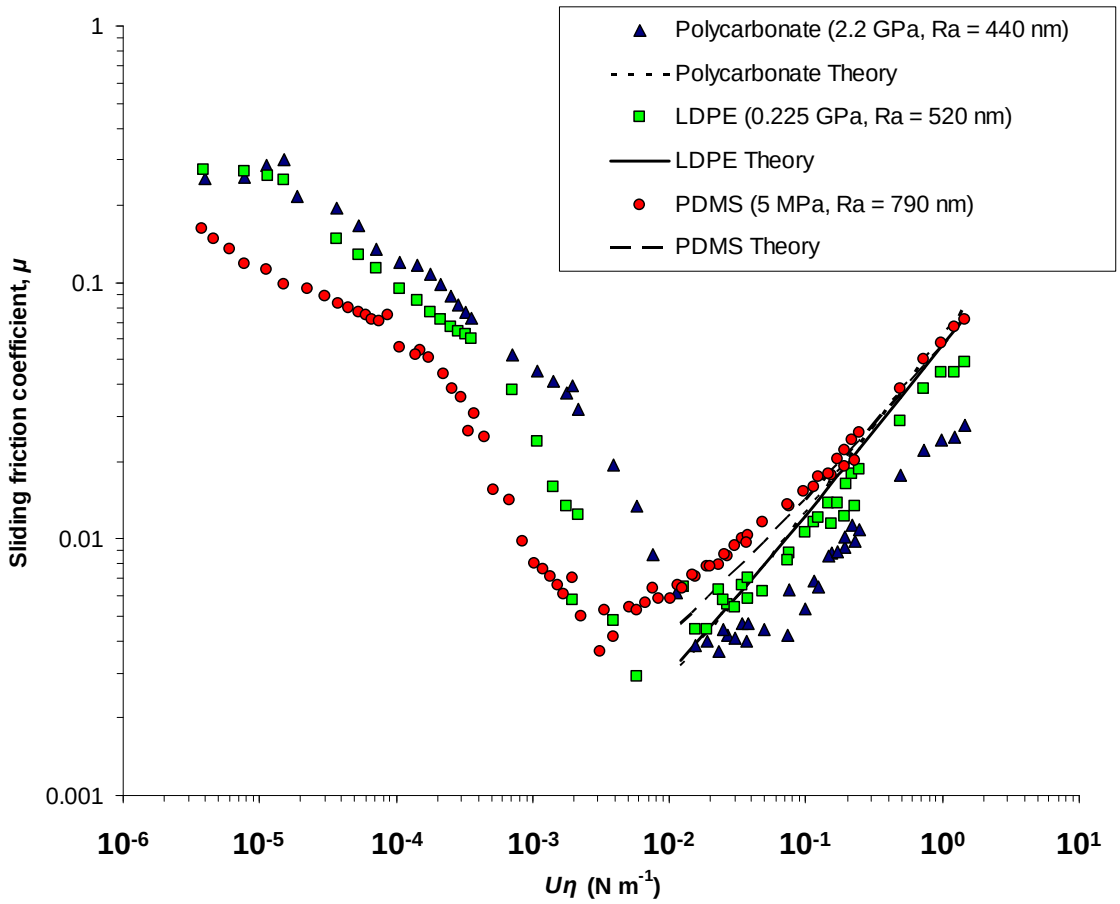

Figure 4.3. Influence of elastic modulus on sliding friction coefficient. Solid and dashed lines show theoretical predictions of Couette friction coefficient from Eq. (2.8).

Both Bongaerts *et al.* and de Vicente *et al.* also showed that as the surface roughness increases, the minimum in the Stribeck curve shifts to larger $U\eta$ and the minimum friction coefficient increases. In Fig. 4.3 the value of the minimum friction coefficient was only marginally affected by the surface roughness and the opposite behaviour is observed, where the minimum in the Stribeck curve shifts to lower $U\eta$

values. This disagreement in trends could be due to the influence of elastic modulus; while the PDMS is rougher than the other two surfaces, this is balanced by it being much more compliant.

Surprisingly, within the isoviscous-elastic regime, at $U\eta$ values greater than 10^{-2}, the friction for the three substrates differs markedly. It is apparent that hydrodynamic friction coefficient increases with reduced elastic modulus. This differs from the predictions of Eq. (2.8), as shown by the solid and dashed lines, which suggest negligible influence of elastic modulus. This difference is unlikely to arise from any wetting or roughness differences, since Bongaerts *et al.* [25] showed that these did not influence the hydrodynamic regime for PDMS (surfaces).

4.2.3. Rolling friction results

Figure 4.4.a) shows the rolling friction results for the tests on PDMS at 0.5, 1, 3, and 5 N applied load. In Fig. 4.4.b) the rolling friction coefficient results for the same tests are given. The figures appear to suggest that within the boundary and mixed lubrication regime the contact obeys Amonton's first and second law of friction.

In Fig. 4.4.b) for $U\eta$ values greater than 10^{-2} in the I-EHL regime, the rolling friction coefficient plots at different loads begin to diverge from one another. Within the I-EHL regime the ball and disk surfaces are no longer in contact. Surface interaction no longer creates friction between the ball and disc, which, instead, originates from hydrodynamic forces generated by the lubricant flowing through the contact. These hydrodynamic forces increase with increasing film thickness. These forces do not increase linearly with applied load so the friction coefficient diverges with increasing load, Fig. 4.4.b).

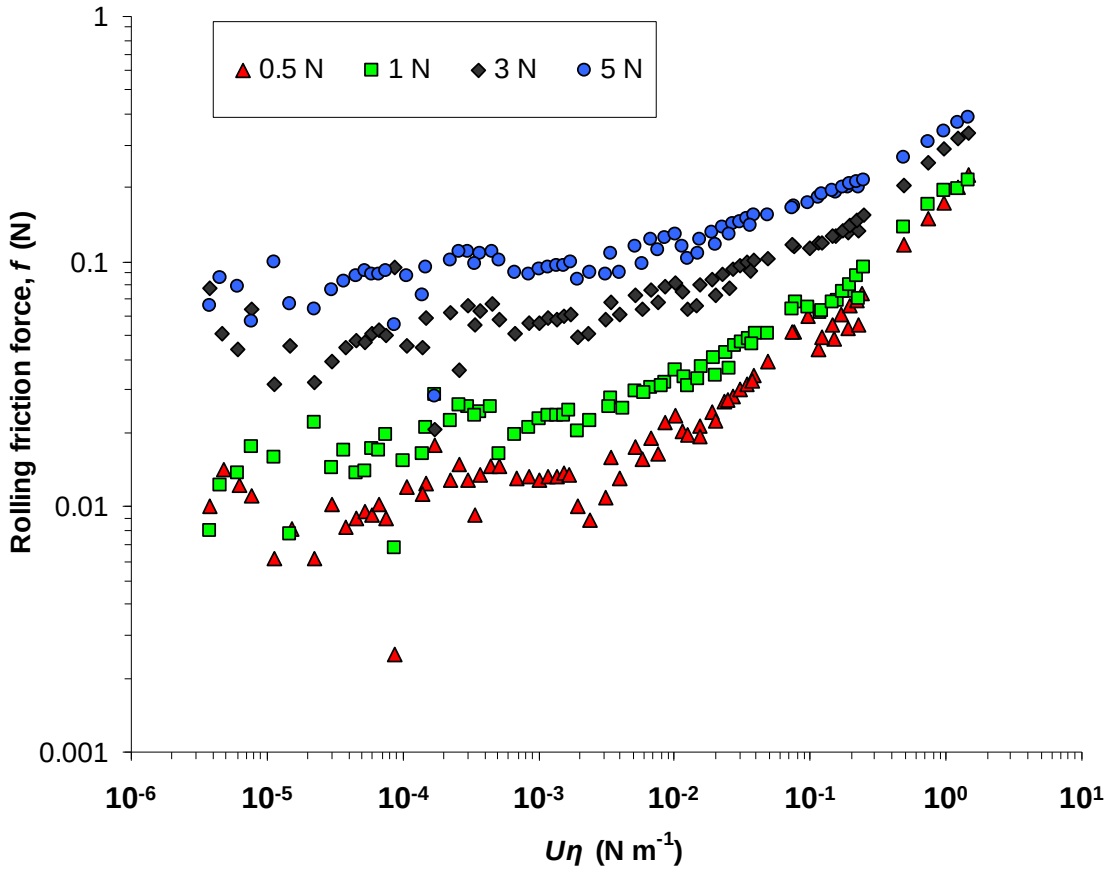

Figure 4.4.a). Influence of load on rolling friction force.

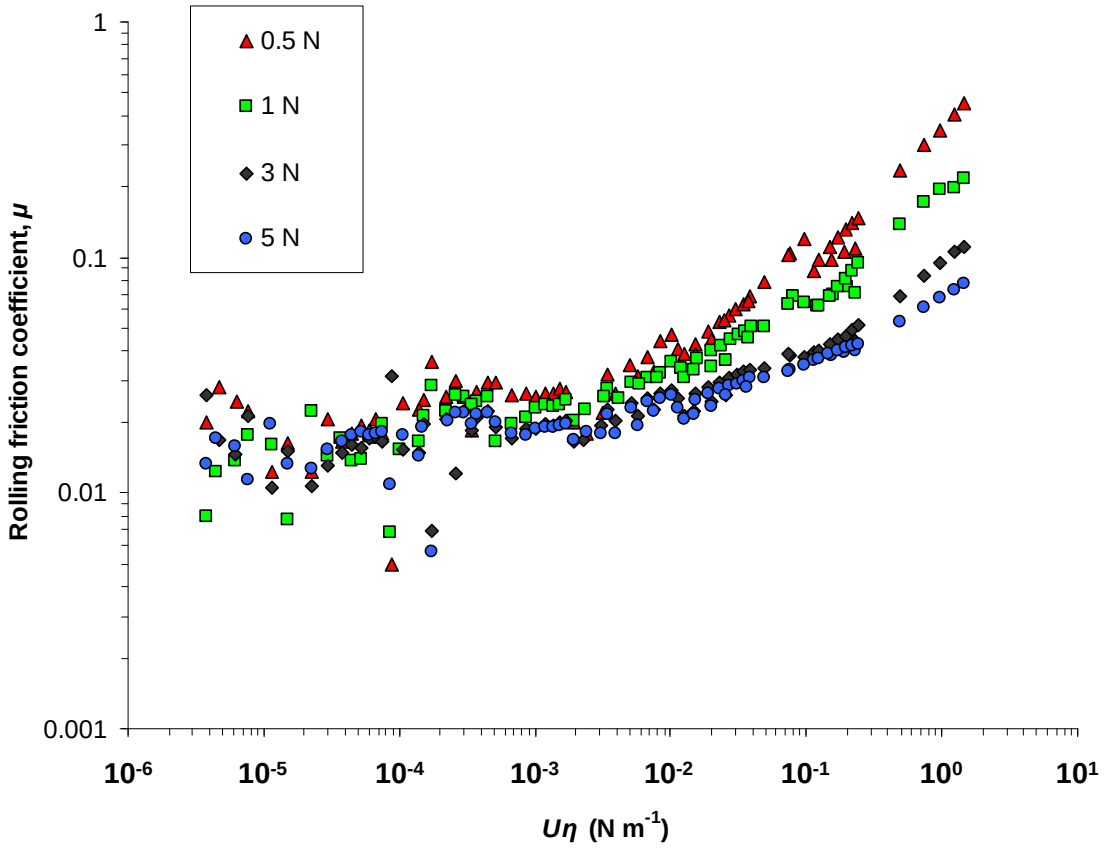

Figure 4.4.b). Influence of load on rolling friction coefficient.

Within the mixed and boundary lubrication regimes, friction originates primarily from deformation losses in the soft substrate. Greenwood *et al.* [80] predicted, and also showed experimentally, that for a dry rolling contact between a metal sphere and rubber flat, the friction increases linearly in proportion to Wa. Since a is proportional to $W^{1/3}$ we should expect the rolling friction to be proportional to $W^{4/3}$, in conditions where rolling friction rises primarily from deformation losses. For the $U\eta$ values suggested in Fig. 3.13.b), the friction values in Fig. 4.4.a) give a power law gradient of 0.95, shown in Fig. 4.5, which was some way below the predicted value. The discrepancy is likely to be due to the presence an active lubricant, although the boundary lubrication properties of water are known to be poor [25].

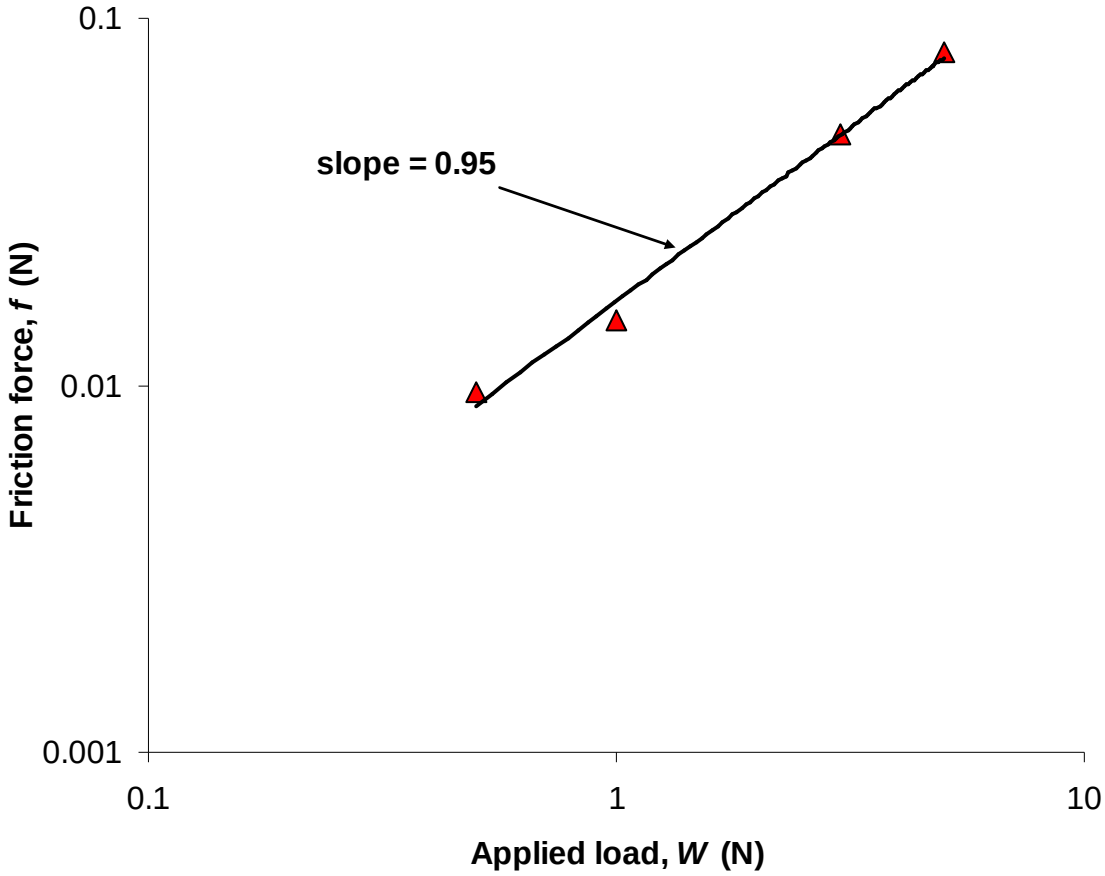

Figure 4.5. Logarithmic plot of frictional force against applied load within the boundary lubrication regime. Solid black line shows power law fit.

Figure 4.6 shows the combined theoretical rolling friction values predicted from theory according Eq. (2.13) at 5 and 0.5 N applied load, plotted as a solid and a dashed line respectively. As described earlier in chapter 3 the loss tangent, tan δ, was measured for all applied loads using a DMA apparatus. The applied load had negligible effect on the response of the PDMS in the DMA; constant values of 0.15 and 2 were used for tan δ and k respectively, for all applied loads. This gives a loss factor, α, of 0.94 for all applied loads.

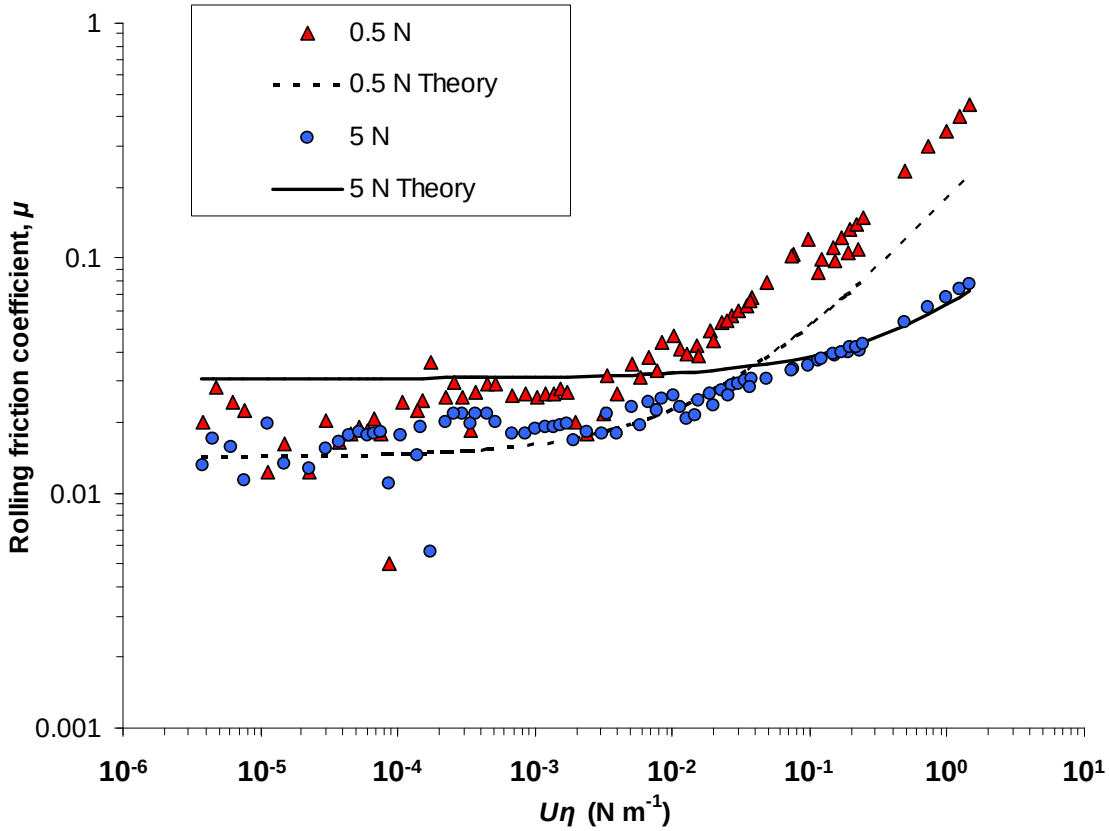

Figure 4.6. Influence of load on rolling friction coefficient. Solid and dashed lines show theoretical predictions of Poiseuille friction coefficient from Eq. (2.13).

Since a is proportional to $W^{1/3}$ it follows that the rolling friction coefficient is proportional to $W^{1/3}$. Assuming tan δ and k to be constant and identical for all loads, a factor of 10 change in applied load would, according to Eq. (2.12), roughly double the rolling friction coefficient in the boundary and mixed lubrication regimes. This prediction is shown in Fig. 4.6. However, the experimental data shows, for the same $U\eta$ range, a negligible change in the boundary and a small decrease in friction coefficient in the mixed lubrication regime with increasing load.

The tan δ value of 0.15, used so far in this investigation, is twice as large as the one given by de Vicente *et al.* [18] for the same PDMS type. This discrepancy is probably due to two different DMA apparatus being used. De Vicente *et al.* used a Rheometrics RDAII in torsional deformation mode, whereas a Tritec 2000 DMA in tension mode was used in the current study. A lower loss tangent will decrease the

overall friction coefficient so using the tan δ value given by de Vicente *et al.* will give a better fit at 5 N but a worse fit at 0.5 N applied load. A tan δ value of 0.2 and 0.1 is found to give a good fit between experimental and theoretical plots for 0.5 and 5 N applied loads respectively. De Vicente *et al.* achieve a good fit between experimental and theoretical plots for 3 N applied loaded, using a tan δ value of 0.07. However, Bongearets *et al.* [25] showed that there was an error in the applied load due to a mechanical fault in the MTM; the real load was 1.3 N. If the correct load is used to determine the friction coefficient, this leads to a considerable disagreement between experiment and theory, with the predicted friction coefficient from de Vicente's I-EHL model [31] being below the experimental values (see Fig. 4.7).

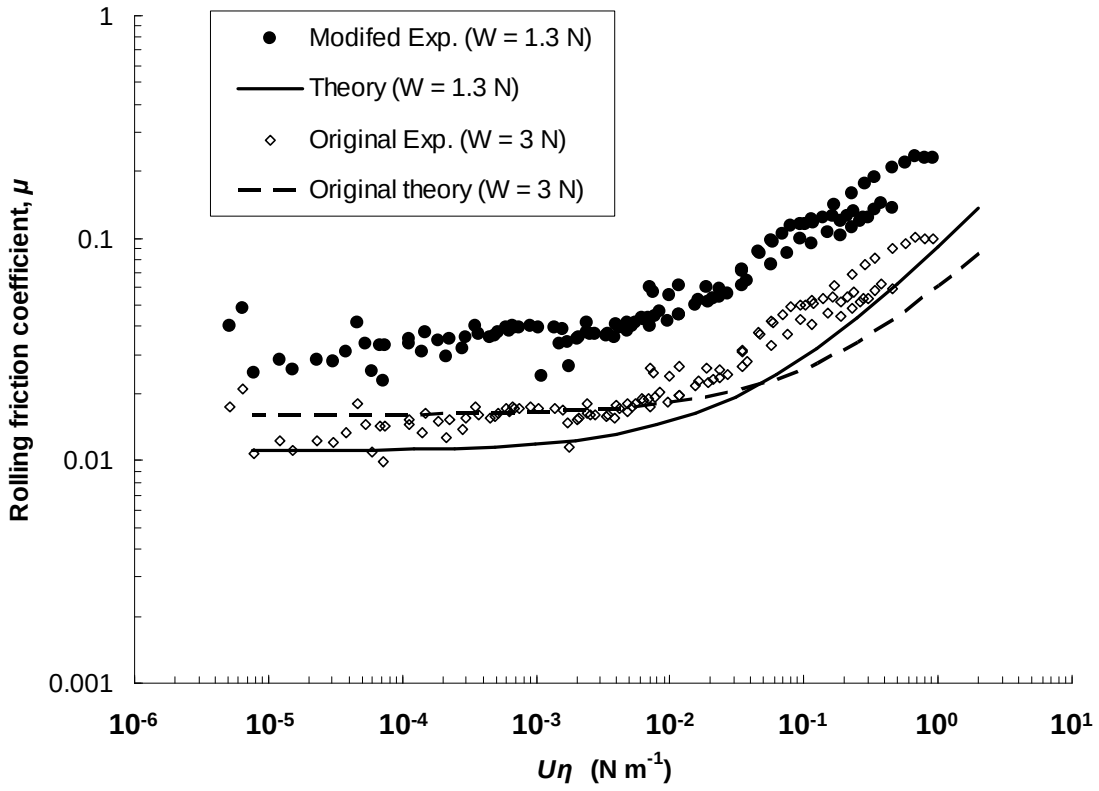

Figure 4.7. Plot of log(rolling friction coefficient) versus log(entrainment speed x viscosity) of De Vicente et al. original (hollow circles) and corrected (solid circles) experimental data. Solid and dashed lines show theoretical friction coefficients for original and corrected loads respectively.

Amonton's 2nd law of friction states that, for a dry contact (boundary), the friction force is independent of the apparent area of contact. Therefore, it would follow that, for the boundary rolling friction coefficient due deformation energy losses, to be independent of the contact size and load, the loss factor, α, must also be proportional to the applied load. We know from DMA measurements of PDMS that E and $tan\ \delta$ change with respect to frequency and temperature. However, load appears to have negligible effect on DMA results. Therefore, it is suggested that, for the tribological contact of interest, $tan\ \delta$ and E are constant across the load range. However, experimental results suggest that deformation losses are independent of a. This leaves one other possibility; that k is not constant for all loads. A value of k = 1.3 and 2.7 give a good fit between experimental and theoretical plots for 5 and 0.5 N applied load respectively. This is still within the limits quoted in the past literature [80].

Figure 4.8 compares the rolling friction results for the PDMS, LDPE and PC samples at 3 N applied load with the total rolling friction coefficient predicted from theory according Eq. (2.13), the data plotted as solid lines. As before, the loss tangent and elastic modulus were measured for each material using a DMA apparatus. A constant tan δ value of 0.15, 0.08 and 0.02 was used for PDMS, LDPE and PC respectively. Values for elastic modulus are given in table 3.3 and a value of k = 2 were used for all polymers.

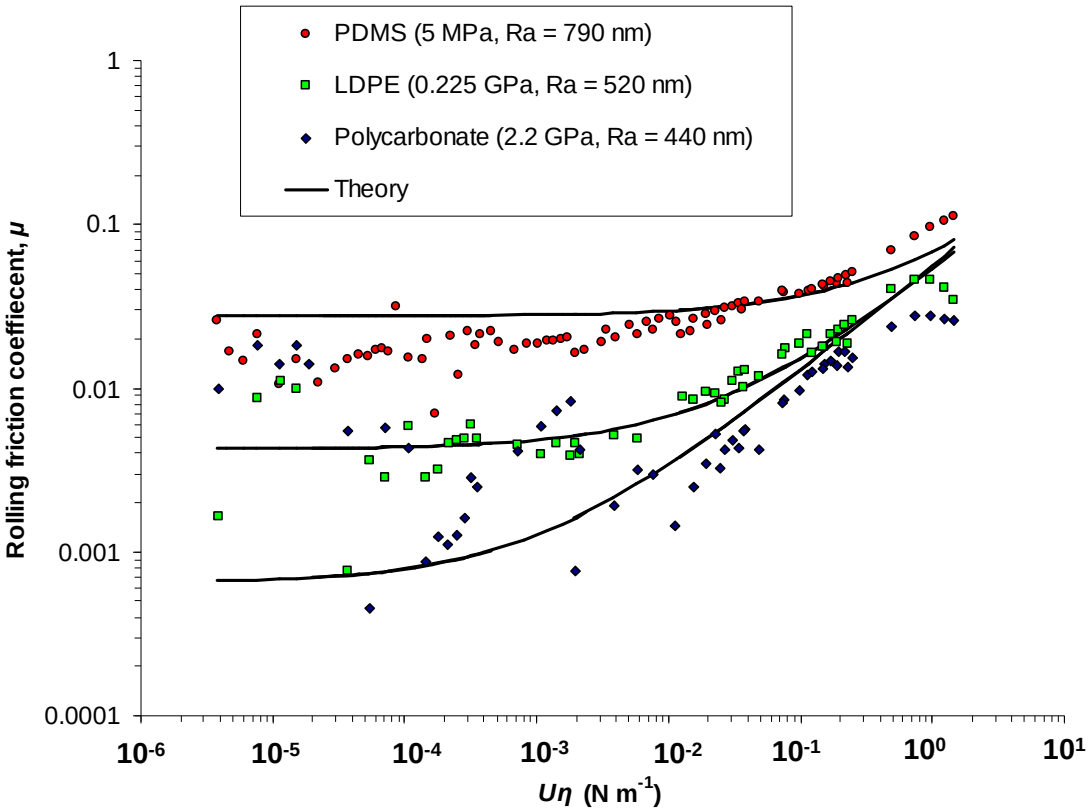

Figure 4.8. Influence of elastic modulus on rolling friction coefficient. Solid lines show theoretical predictions of Poiseuille friction coefficient from Eq. (2.13).

The results show considerable scatter, especially at very low friction values which are at the limits of the MTM measurement capability. There are, however, clear differences in the values of friction coefficient for all the polymers at low $U\eta$, as predicted by the theoretical plots. As described above, rolling friction coefficient within the mixed and boundary lubrication regimes originates primarily from deformation losses in the soft substrate. Greenwood and Tabor [79] showed experimentally that within these regimes, rolling friction coefficient is roughly proportional to a/R. At 3 N applied load, the predicted Hertzian contact radii for PDMS, LDPE and PC are 1.48, 0.41 and 0.19 mm respectively. Since a is proportional to $E'^{-1/3}$ and R is constant and identical for all polymers, provided α is constant, μ_{def} (Eq. 2.11) will depend up the ratio $E'^{-1/3}/R$. Due to the scattered nature of the experimental results within the boundary and mixed lubrication regimes it was not possible to see if this relationship holds.

As $U\eta$ increases the friction coefficient becomes dominated by the lubricant flow and surface interactions decrease. At high $U\eta$ values the curves converge as friction becomes determined solely by Poiseuille losses. This is the opposite trend observed in Fig. 4.4.b) as suggested by Eq. (2.8).

4.2.4. Effect of Loading Frequency

Greenwood *et al.* [79,80] noted that over a moderate range of strains and deformation rates, the quantity α, is roughly constant for a given rubber. Up until now all theoretical predictions for rolling friction coefficient have assumed this. However, the range of strains and deformation rates covered in this investigation are far greater than those used by Greenwood *et al.* It can be observed that the series of friction measurements obtained with different viscosity fluids in Figs. 4.4.a) and 4.4.b) do not exactly join together. This is more clearly seen in Fig. 3.13.b) where the different fluids are shown using different symbols. There appears to be an increase in rolling friction as entrainment speed rises, independent of the fluid viscosity. This rise may be related to an increase in energy dissipation load frequency and this would be represented as a change in the quantity α.

Loading frequency, Ω, can be described as the rate at which each contact area is loaded and un-loaded as the disk passes under the MTM ball; in other words,

$$\Omega = {u_d}/{2a} \tag{4.1}$$

where u_d is the disk speed and a the theoretical Hertzian contact radius. As indicated in Fig. 4.9 results from DMA analysis of the PDMS used in this investigation showed that the mechanical properties of the soft substrate depend on the frequency of deformation. The applied load has negligible effect on the response of the PDMS in the DMA, but, as loading frequency is increased, the elastic modulus and loss

tangent increases. This is probably why, for a frequency range at the same $U\eta$ value, a resultant increase in rolling friction coefficient is observed.

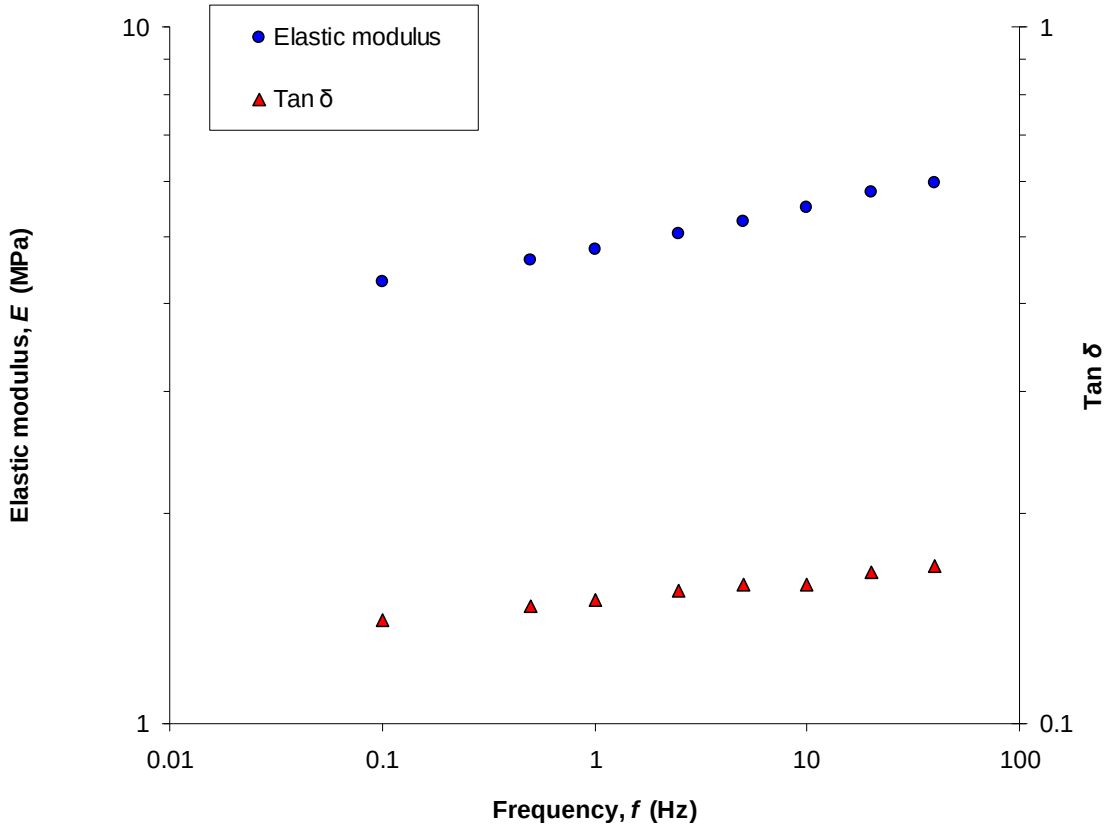

Figure. 4.9 Plot of log (elastic modulus) and log (loss tangent, tan δ) versus log (loading frequency) for PDMS at 3 N applied load.

Figure 4.9 shows DMA analysis of elastic modulus and loss tangent, respectively, for PDMS at 3 N applied load. By fitting a power law model to Fig. 4.9 values for elastic modulus at high loading frequency can be calculated:

$$E = k.f^{n} \tag{4.2}$$

k and n are the elastic modulus power-law coefficient and index respectively. The use of a power law model is justified by the observation that the elastic modulus was linear on a log-log scale. The same principle was applied for the loss tangent:

$$\tan\delta = C.f^{z} \tag{4.3}$$

where C and z are the loss tangent power-law coefficient and index respectively. A good fit was found for $k = 5.5\text{x}10^{6}$, $n = 0.06$, $C = 0.11$ and $z = 0.06$.

Figure 4.10 shows the results for rolling friction of PDMS at 3 N applied load. The rolling friction contribution predicted from theory according Eq. (2.13) is plotted as solid lines. Using Eqs. (4.2) and (4.3) the resultant high frequency values for E and tan δ (in turn E' and a) are used to recalculate the total rolling friction, in Eq. (2.13). It can be seen that a closer fit was achieved when the dependence of the elastic modulus and loss tangent on loading frequency were applied to Eq. (2.13). There still appears to be a further component of the measured rolling friction, which occurs only in the full-EHL regime and increases with $U\eta$. The origin of this is as yet uncertain. The effect is not likely to be due to viscoelasticity of the PDMS because the latter showed quite small variation in loss tangent over the frequency range of interest. As shown in Fig. 4.10 the changes in the viscoelastic properties of the PDMS are negligible within the I-EHL regime.

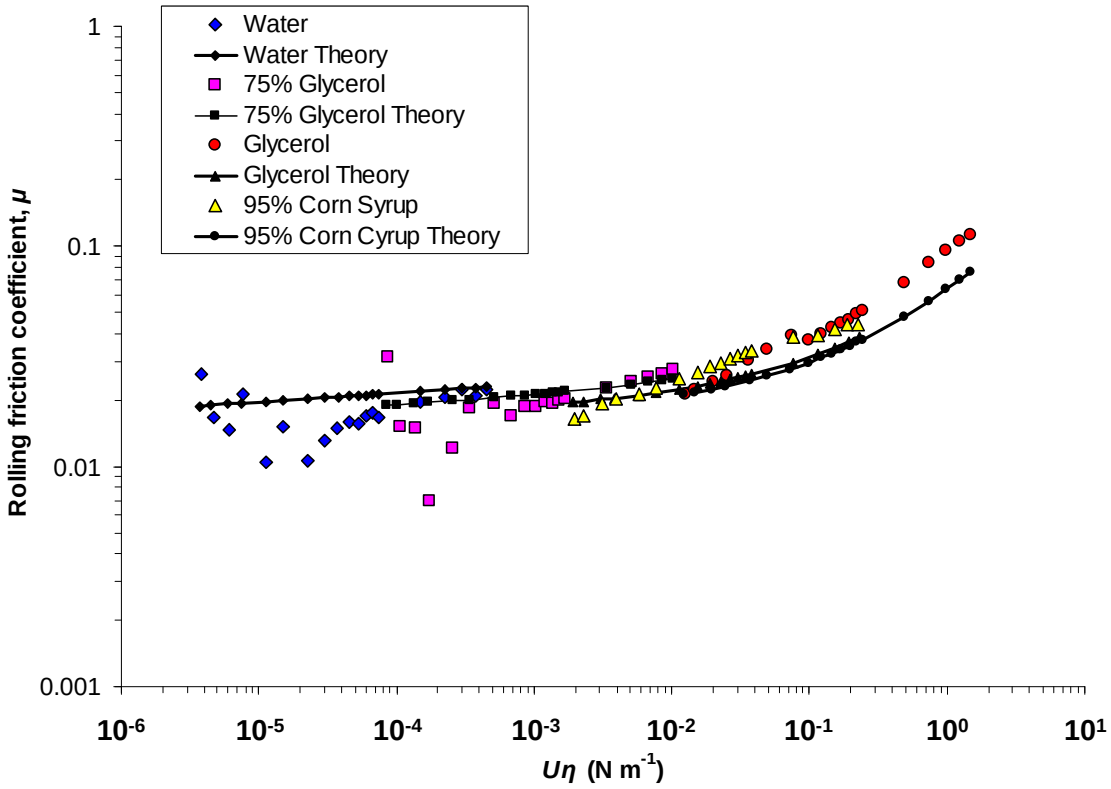

Figure 4.10 Plot of log(rolling friction coefficient) versus log(entrainment speed x viscosity) for a range of lubricants at 50% SRR, with a PDMS disk (R_q= 790 nm) at 3 N applied load. Solid lines show theoretical predictions of Poiseuille friction coefficient from Eq. (2.13), with changes in elastic modulus and loss tangent due to loading frequency applied.

4.3. Conclusions on effect of load and elastic modulus on friction

A ball on disc apparatus has been used to study the effects of load and substrate elasticity on the friction of rolling-sliding, lubricated, compliant contacts. This was performed by varying the applied load on a PDMS disc, and using three different polymer discs with elastic moduli varying across three orders of magnitude at a constant load of 3 N. Separate rolling friction and sliding friction 'Stribeck' curves

have been measured and the results from the study have been used to validate the numerical models developed by de Vicente *et al.* [31] in the I-EHL regime.

The measured influence of load on the isoviscous-elastic sliding friction coefficient for all three polymers agrees quite closely with numerical predictions in the I-EHL regime. However, the numerical models do not predict the I-EHL rolling friction coefficient accurately as a function of applied load.

The elasticity of the substrates has contrasting effects on the sliding and rolling friction. Two trends are observed in the I-EHL regime. While experimentally it was found that the sliding friction coefficient increases with decreasing elastic modulus, the models predict that there should be a negligible effect due to the elastic modulus. However, for rolling friction, the friction coefficient converges towards a constant value of ~ 0.1 at high entrainment speeds. This is not surprising as deformation losses will become negligible, at high $U\eta$ values, in comparison to those associated with Poiseuille flow. Consideration of the frequency dependence of the deformation energy losses in the substrates has enabled the rolling friction coefficient to be predicted reasonably accurately, especially within the mixed and boundary lubrication regimes.

Chapter 5

Interferometric system for thin film measurement

This chapter describes the first of two experimental techniques used in this study to measure lubricant thin film thickness in a compliant contact. Optical interferometry has become a standard technique for measuring lubricant film thickness in 'hard', metallic contacts. In this chapter, this procedure is adapted to meet the requirements of poorly reflective contacting materials, where one or both materials have a low elastic modulus.

5.1. Introduction:

The measurement of lubricant film thickness values within a compliant contact is a challenging problem for several reasons [8]:

- Lubricant film thickness covers a wide range of values; the required measuring range is from fractions to the hundreds of microns.
- Contact size is considerably larger than in non-compliant tribological contacts.
- Polymer materials are poor electrical conductors and poor reflectors of light.
- Coating soft surfaces with reflective layers is not trivial as the latter are either prone to wear or influence the compliance and surface properties significantly, or both.
- Many soft components have a high roughness compared to surfaces usually investigated with established techniques. They are also very difficult to smooth.

Notwithstanding these difficulties, when designing components for use in lubricated, compliant, contacts, the liquid film thickness is a significant parameter, so it is important that solutions are found to the issue listed above. Currently there exist very few techniques for measuring lubricant film thickness within compliant lubricated tribological contacts. Optical interferometry [68,69,71], magnetic resistance [8], laser induced fluorescence [7] and Raman spectroscopy [19] have all been used successfully. However, each of these has limitations and difficulties. As of yet there is no established technique for routinely obtaining film thickness data from a soft contact.

This chapter describes a technique for measuring lubricant film thickness between soft deformable surfaces under low-load/low-pressure conditions using optical interferometry.

5.2. Measuring technique:

The basic principles and concepts of interferometry are well documented and can be found in many texts. The application of interferometric techniques for investigating lubricant behaviour in a tribological contact is well established. A good description of the different techniques and their principles is given by Gohar [2] and Westlake [58].

5.2.1. Requirements

The overall goal is the measurement of lubricant film thickness in a compliant contact under low load, low pressure conditions. The film thickness measurements are to be obtained from image-intensified interferograms captured under monochromatic light. This particular application demands certain requirements of the interferometric system. Firstly, the fringe order must be determined directly from the interferograms. Secondly, the fringes should be closely spaced and form a continuous pattern which will enable the thickness at intermediate fringe positions to be calculated. Thirdly, a new interferometric system must be established to produce good quality interferograms from poorly reflective surfaces.

The objective was to design an interferometric system which would fulfil these requirements and, at the same time, satisfy the necessary conditions for obtaining clear and well-defined fringes. To obtain clear interference fringes, certain interferometric principles must be considered. These are presented and discussed in conjunction with the choice of interferometric system.

5.2.2. Monochromatic or two beam system

When a monochromatic source is used and only two beams interfere the system is described as being 'two beam'. The interference fringes formed by this system are based on the 'division of amplitude' of the incident wave [56]. The incident light wave from the source is divided by partial reflection on the bottom surface of the glass. The resulting wave fronts maintain their original width but have reduced amplitudes.

The principle of light refraction states that a ray of light will change direction when it crosses an interface of two materials with differing refractive indices. Secondly, light reflects partially from surfaces that have a refractive index different from that of their surroundings. Gohar [94] explains the interferometric system by considering the tribological contact in Fig. 5.1. The incident rays A_1 and A meet the lubricant surface at B_1 and B, at an angle of incidence *i*. The ray A_1B_1 refracts at angle *i′* to C_1, reflects to B and emerges together with the reflected part of ray AB. Further reflections and emergences from these two rays occur along the glass window, but these need not be considered at present.

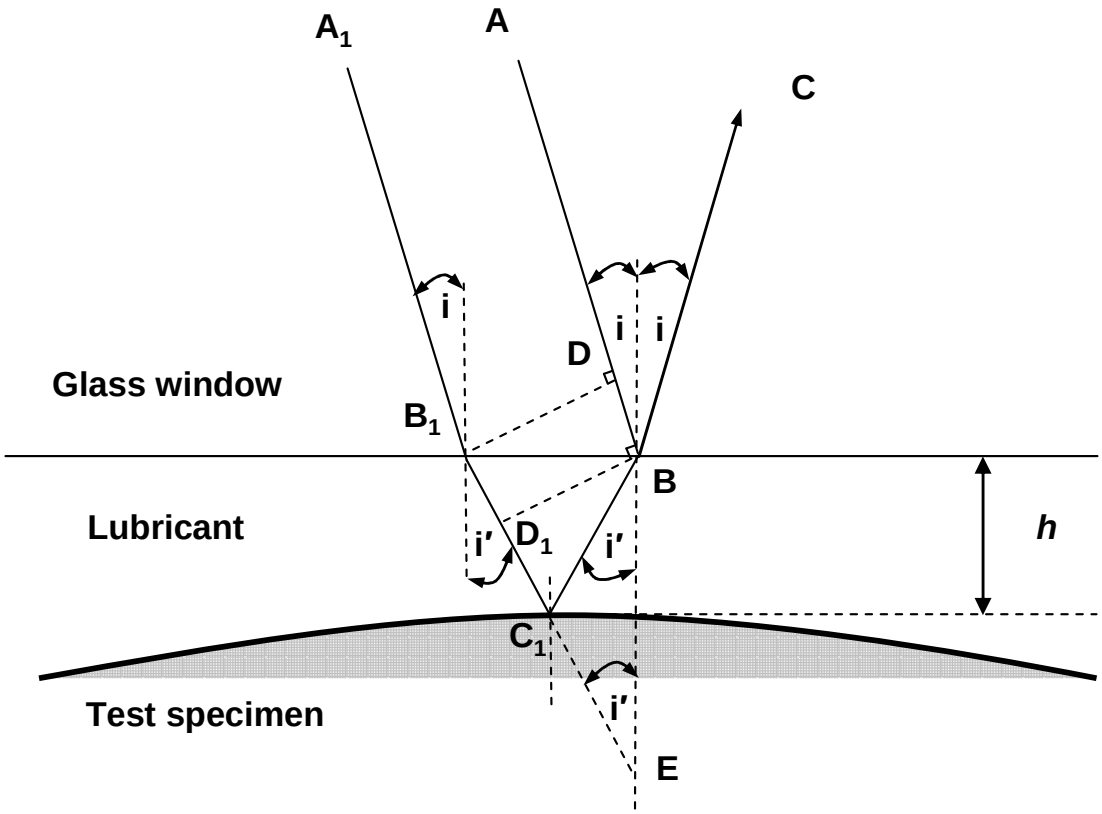

Figure 5.1 Principle of Two-beam optical interferometry

The phase difference of A_1B_1 and AB stays constant with respect to DB_1, where D is the foot of the perpendicular from B_1. The time for B_1 to reach D_1 in the film is the same period for D to reach B. Therefore the path difference, δ, in the medium is B_1E-B_1D_1, where $B_1D_1 = DB$ and $B_1C_1 = C_1E$.

The resulting intensity at this point depends on the phase difference between the rays. If they are nearly in phase they 'constructively' interfere, giving rise to an intensity which is greater than the sum of the two rays acting separately. Conversely, if the rays are nearly out of phase, they 'destructively' interfere, giving rise to an intensity which is less than the sum of the two rays acting separately.

The phase difference depends on the 'optical' path difference between the two rays which for normal incidence is $2nh$ where n is the refractive index of the medium (lubricant) and h is the physical gap (lubricant film thickness). There is also often a phase change in reflection at either one or both of the reflecting surfaces. A

correction, Φ, must then be added to the path difference. For oblique incidence the path difference can be shown to depend on the cosine of the angle *i′*. Thus, the path difference between the rays A_1B_1 and AB becomes:

$$\delta = 2n_{\text{lub}\,e}B_1E - B_1D_1 + \Phi \tag{5.1}$$

Then from geometrical considerations:

$$\delta = 2n_{\text{lub}\,e}h\cos i' + \Phi \tag{5.2}$$

Constructive interference occurs when the path difference is equal to an integral number of wavelengths, $N\lambda$. From Eq. (5.2) the general condition is given by;

$$N\lambda = 2nh\cos i' + \Phi \tag{5.3}$$

Bright fringes are produced from constructive interference. N is called the 'fringe order' and can take on integer values of 0, 1, 2,…. Destructive interference occurs when $\delta = (N + 0.5)\lambda$. Therefore, when

$$(N + 0.5)\lambda = 2nh\cos i' + \Phi \tag{5.4}$$

dark fringes are produced.

If λ, cos *i′*, and Φ are constant, the fringe order will depend on the optical path difference 2*nh*. These fringes are called 'fringes of equal thickness' which, according to the system in Fig. 5.1, are localized on the lower glass surface.

The nature of the fringes produced by two identical interfering rays will be broad, with a spacing equivalent to $\lambda/2$ between adjacent maxima and minima. Using fringes alone it is not possible to resolve fine detail as their width has a masking effect. An additional system to measure lubricant film thickness for values less than

$\lambda/4$ was devised by Roberts *et al.* [68]. Here grey scale data between fringes on an interferogram are interpolated to give detailed film thickness results.

5.2.3. Fringe visibility

The clarity of fringes is usually described by their 'visibility'. Michelson [95] defined visibility as;

$$V = \frac{I_{\max} - I_{\min}}{I_{\max} + I_{\min}} \tag{5.5}$$

where I_{max} and I_{min} are respectively the maximum and minimum intensities of the fringes. When I_{min} = 0 the visibility equals a maximum of the fringes. When I_{max} = I_{min} the visibility is zero and no fringes are seen at all.

If the rays EF_2 and $E'F_3$, in Fig. 5.1, are 'coherent' (*i.e.* in phase and of the same frequency), the resulting intensity of interference fringes will depend on the individual intensities, I_1 and I_2 respectively, of the two rays and their path difference, δ, according to Fresnel's classical formula;

$$I = I_1 + I_2 + 2\sqrt{I_1}\sqrt{I_2}\cos\frac{2\pi\delta}{\lambda} \tag{5.6}$$

Maximum intensity occurs when $\cos\frac{2\pi\delta}{\lambda} = 1$, and minimum intensity occurs when $\cos\frac{2\pi\delta}{\lambda} = -1$. Thus,

$$I_{\max} = I_1 + I_2 + 2\sqrt{I_1}\sqrt{I_2} \tag{5.7}$$

$$I_{\min} = I_1 + I_2 - 2\sqrt{I_1}\sqrt{I_2} \tag{5.8}$$

The visibility is;

$$V = \frac{2\sqrt{I_1}\sqrt{I_2}}{I_1 + I_2} \tag{5.9}$$

which has a maximum of unity when the intensities are equal ($I_1 = I_2$). For this case, the intensity distribution follows a $\cos^2$ law according to $I = \cos^2 \frac{\pi\delta}{\lambda}$. Equal intensities are achieved by controlling the reflectivities of the surfaces.

For visible interference fringes to be obtained, the interfering rays must be mutually coherent. That is the phase difference of the interfering rays must be constant. This condition is satisfied if the two rays emitted by the source at A, are in phase, have the same frequency, and are continuous over the path difference.

The degree of coherence, γ, allows Fresnel's formulae for I_{max} and I_{min} can be written as;

$$I_{\max,\min} = I_1 + I_2 \pm 2\sqrt{I_1}\sqrt{I_2}\gamma \tag{5.10}$$

For mutually coherent beams, γ reaches a maximum of one, and for non-coherent beams γ falls to a minimum of zero. The visibility of the fringes then becomes a function of the degree of coherence,

$$V = \frac{2\sqrt{I_1}\sqrt{I_2}}{I_1 + I_2}\gamma \tag{5.11}$$

which will reach a maximum when the two beams have equal intensities and are mutually coherent. As the path difference, δ, increases, the degree of coherence, γ,

and hence visibility, *V*, decreases. Therefore, interference fringes can only be seen over a finite thickness.

Wedeven [56] gives an alternative explanation for the decrease in visibility with path difference which is compatible with the theory of partial coherence. The length of the wavetrains emitted by a source is related to the inverse of the bandwidth. All sources have a finite spectral bandwidth, *i.e*. the emitted light waves are composed of a mixture of wavelengths. In this respect no source is truly 'monochromatic'. If the source emits various wavelengths, the fringes formed by the shorter wavelengths will be closer together than those of longer wavelengths. At zero path difference the fringes formed by the various wavelengths coincide. As the path difference increases, the dark fringes of the shorter wavelengths begin to overlap the light fringes of the longer wavelengths (and *vice versa*). This confusion of fringe position causes a decrease in visibility. The rate at which the visibility decreases as *h* increases depends on the bandwidth of the source. Clear or visible fringes can only be obtained over large thicknesses if the bandwidth is sufficiently narrow. However, very wide bandwidths can be tolerated if the thicknesses to be measured are small. This is important in that it allows a greater choice of light sources and spectral distributions to be used.

Duo-chromatic and white light interferometry techniques take advantage of the overlapping wavelengths to improve fringe visibility. If the spectral distribution consists of a group of shorter wavelengths and a group of longer wavelengths, at a particular thickness the dark fringes from one group overlap the light fringes of the other. As the thickness is increased further, the dark and light fringes of both groups will coincide. The resulting visibility rises and falls in a periodic manner. This system creates greater accuracy in determining fringe order and position. However, as the spectral distribution is increased, the measureable range of film thickness decreases.

The range of obtainable film thickness values is related to the coherence, size and quality of the illuminating light source. Compliant contacts tend to form thicker film

thicknesses than stiff contacts; therefore a monochromatic interferometric system lends itself to investigating compliant contacts.

5.2.4. Reflecting surfaces

The quality of the fringes and the accuracy of the measurements taken with the interferometer depend primarily on three conditions of the reflecting surfaces.

The first is the surface finish. The intensity of a fringe will change from a maximum to a minimum (or *vice versa*) if the optical gap changes thickness by $\frac{\lambda}{4n}$. It is therefore important that the surfaces in contact conform locally to a mean elevation which is less than $\frac{\lambda}{4n}$. In other words the test surfaces must have an optically smooth surface finish [70].

The second condition concerns that of geometry. If meaningful measurements of elastic deformation are to be obtained, it is essential that the deviation from a perfect surface geometry is small in comparison with the deformation due to pressure. The manufacture of spherical balls of low elastic modulus with an optically smooth surface finish and geometrical shape is not a trivial matter. It is primarily for this reason that the experimentation presented here is limited to a point contact.

The third condition is that of reflectivity. For monochromatic interferometry, maximum fringe visibility is obtained when the intensities of the two beams are equal (*i.e.* $I_1 = I_2$). Similar intensities can be achieved by controlling the reflectivity of the surfaces. High reflectivity is not a necessary requirement of two-beam interferometry. It is possible to obtain fringes of good visibility with surfaces of very low reflectivity (and hence high absorption and/or transmission) provided that $I_1 \approx I_2$. This is not, however, a very efficient use of the total light input [56].

To obtain fringes of high visibility it is most important that the reflectivities of the two contacting surfaces are compatible in making the intensities of the two interfering rays similar ($I_1 \approx I_2$). For normal incidence, the reflectivity, R, at an interface between two non-magnetic materials follows Fresnel equation;

$$R = \left(\frac{n_1 - n_2}{n_1 + n_2} \right)^2 \tag{5.12}$$

where n_1 and n_2 are the refractive indices of the two media.

The commonly-used 'hard' or metallic contact between a steel ball and plain glass disk coated with a semi reflective chromium layer is used in most standardised optical systems for measuring lubricant film thickness [39]. Wedeven [56] measured the reflectivity, R, and absorption, A, for each surface/interface within the standard optical contact. These are shown schematically in Fig. 5.2. Values were obtained from measurements taken with the experimental light source, a standard base oil (n = 1.55) and a photocell.

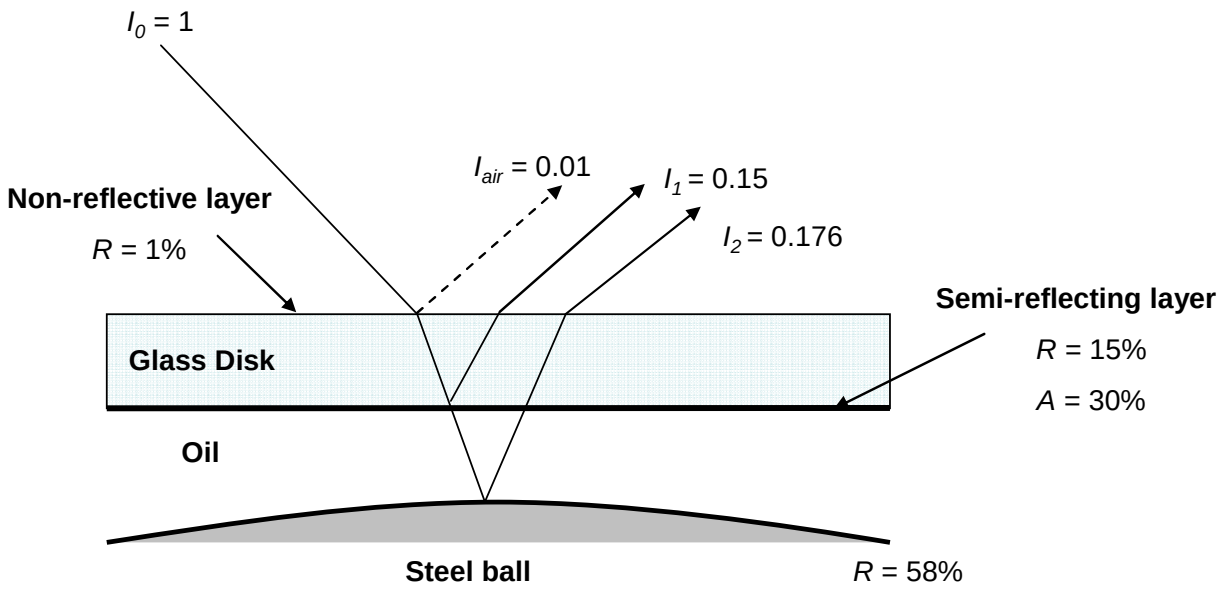

Figure. 5.2. Reflectivity of surfaces and resulting intensities of interfering rays. Wedeven [56].

The reflectivity of the steel ball was found to be 78 % in air and about 58 % in oil. The glass race was specified to have a chromium layer of 15 % reflectivity, measured from the glass/chromium side when oil is placed on the back surface. The chromium layer is added to increase the reflectivity at the glass/oil interface and thus balance the intensities of I_1 and I_2 to create fringes of good visibility. The absorption of the chromium layer was deduced from the measurements of transmission and reflectivity of the glass disc. The free electrons in the metal film cause a rather high absorption of 30 %. The high absorption is not detrimental to the fringe visibility for two-beam interferometry, provided that $I_1 = I_2$, but it does reduce the utilization of the total light input.

The reflection from the air/glass interface (ray AB or A_1B_1 in Fig. 5.1) is calculated to be ≈ 4 %. To reduce the reflectivity at the air/glass interface, Wedeven coated the upper surface of the glass with a non-reflecting film, magnesium fluoride (n = 1.38). The glass was coated to a thickness of $\frac{\lambda}{4n}$ where λ corresponds to a wavelength approximately in the middle of the visible spectrum of the illuminating light. Incident light reflects off the air/MgF_2 interface and the MgF_2/glass interface. Both reflections are from a 'rare-to-dense' medium since the index of refraction of MgF_2 is less than plain glass (n = 1.52). This causes a phase change of π to occur for both reflecting interfaces. The rays reflecting from the MgF_2/glass interface travel through the film twice, thus making the path difference between the two reflecting interfaces equal to one-half wavelength; this is the condition for destructive interference. The non-reflecting film does not destroy the light but redistributes it. Therefore, the decrease in reflectivity accompanies a corresponding increase in transmission. The refraction of MgF_2 and glass are not exactly correct to establish interfering rays of equal intensity, so the reflection is not totally suppressed. Also, the film is less effective for those wavelengths which are not near the middle of the visible spectrum. The film is, however, effective in reducing the reflection to about 1 %.

The intensities of the two interfering rays shown in Fig. 5.2 can be calculated as:

$$I_1 = I_0(R_{glass/lube} + A) \tag{5.13}$$

$$I_2 = [(1 - I_1)R_{lube/sample}] - [(1 - I_1)R_{lube/sample}.(R_{glass/lube} + A)] \tag{5.14}$$

where A is the absorption of the semi-reflective layer. The intensities of I_1 and I_2 are nearly equal; from Eq. (5.11) a visibility of 0.996 is calculated.

For the optical contact in the current study, the steel surface is replaced with PDMS which is poorly reflective, calculated to be 0.048 % in glycerol (n = 1.47). One way to increase the reflectivity of the PDMS is to sputter its surface with a reflective coating. A number of different coatings were trialled, these included; gold, aluminium and chromium. However, the addition of reflective coatings was not successful, as they were prone to wear or influenced the compliance and surface properties significantly. At this point, however, it is important to remember that to achieve fringes of good visibility it is not necessary to have interfaces of high reflectivity. Therefore, instead of coating the PDMS with a reflective material, the reflectivity of the other interface must be reduced. This is achieved by using a glass surface without a reflective coating. Plain BK7 glass has a calculated reflectivity of 0.024 % in glycerol. The subsequent visibility is *ca* 97 %. However, intensity will be extremely low so some form of image-enhancing camera will be required to capture the interference images.

For Wedeven's contact, the initial reflection from the top surface of the glass disk is of limited importance due to its weak intensity compared to the interfering rays from within the contact. The reflection would lower the intensity of I_1 and I_2 slightly, but have a negligible effect on the visibility. However, due to the low reflectivity of the PDMS and the lack of a semi-reflective layer, I_1 and I_2 are now less than 1 % for a compliant PDMS/glass contact. The air/glass reflected light, which may reach the image plane, will greatly dilute the image and therefore reduce fringe visibility. Although MgF_2 is effective at reducing the reflection it is still too large for the current system. Roberts *et al.* [68] introduced an Abbe prism to replace the flat glass

disc. The illuminating beam was then moved to a non-normal incidence to the contact area, so the amount of scattered light received by the detector was greatly reduced. This is shown schematically in Fig. 5.3.

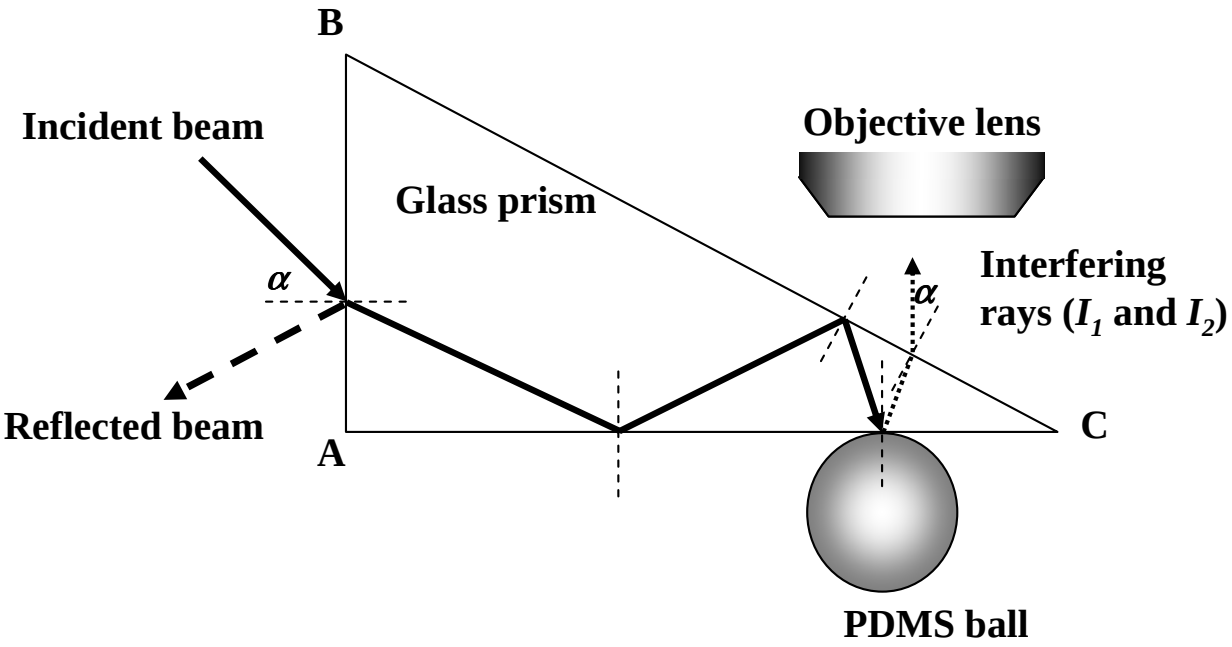

Figure 5.3 Tribological contact of interest

The Abbe prism consist of a block of glass forming a right prism with 30°-60°-90° triangular faces. A beam of light enters face AB, is refracted and undergoes total internal reflection from face AC and BC, and enters the contact about three quarters of the way along the face AC from A. Here, a portion of the light is reflected from the glass surface while the remainder passes through a lubricant film to be reflected back from the ball surface. The two rays interfere at the reflecting surface AC and the resulting light is refracted on exiting face BC before being detected. To ensure that total internal reflection occurs at faces AC and BC, an initial angle, α, of 23° is calculated from Snell's law. From the design of an Abbe prism this gives an exit angle equal to α. By rotating the prism and incident beam (in the plane of the diagram) around point A on the face AB, the interfering rays can be guided vertically upwards into the objective lens. In the current study, Roberts' Abbe prism approach is developed further to study lubricant film thickness in sliding, lubricated compliant contact.

Using Eqs. (5.12), (5.13) and (5.14) the intensities for I_1 and I_2 for the PDMS/transparent surface separated by lubricant can be calculated for a range of lubricant refractive indices so that the fringe visibility can be calculated using Eq. (5.11). Assuming the interfering light rays are mutually coherent, $\gamma = 1$, the calculated visibilities for the BK7 glass prism, high refractive index glass ($n = 1.93$), sapphire ($n = 1.77$) and diamond ($n = 2.2$) against PDMS are shown in Fig. 5.4. Predictably the visibility falls to zero at the refractive indices of the PDMS and the transparent surface. Maximum visibility is obtained at a mid point between the two solid media. It can be seen that an optical window made from BK7 glass will produce the most visible interference fringes for aqueous solutions, which commonly have a refractive index between 1.3 and *ca* 1.4. However, some oils have a higher refractive index. To investigate the lubricant film thickness in an oil lubricated compliant contacts an optical window should be made of sapphire to produce visible interference fringes. The range of lubricant refractive indices best suited to sapphire are $1.48 < n < 1.64$.

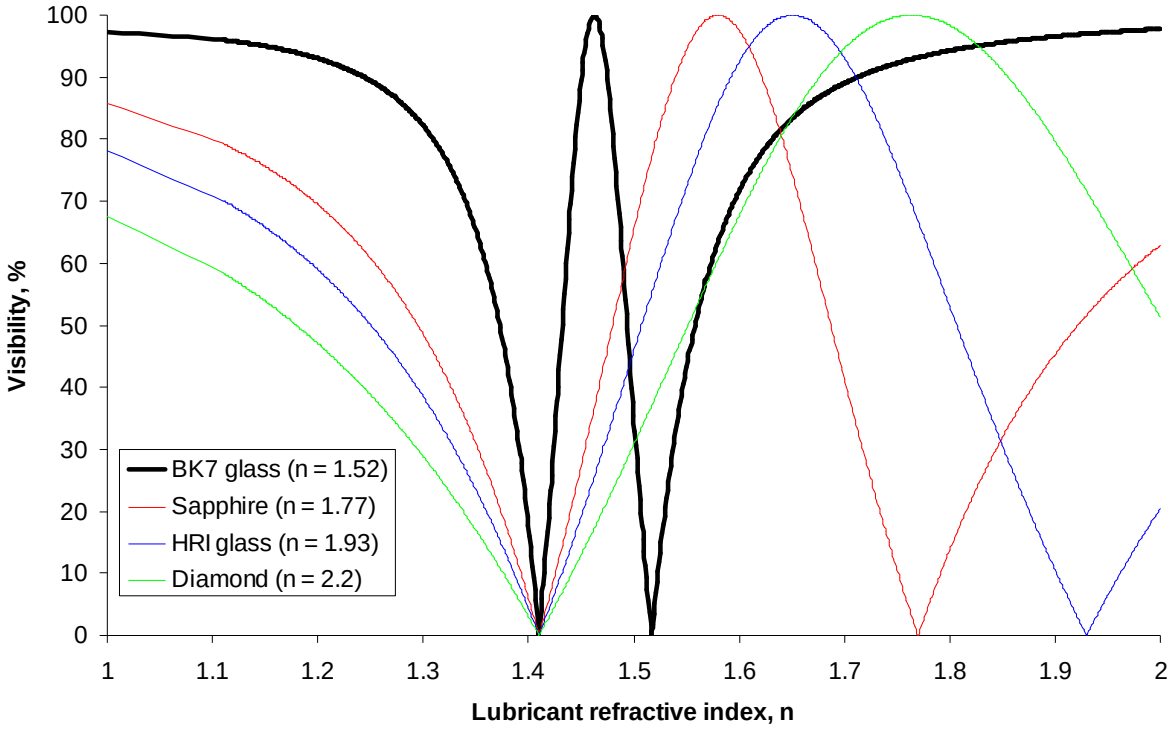

Figure 5.4. Fringe visibility versus lubricant refractive index for BK7 glass, HRI glass, Sapphire and Diamond prisms Refractive index of PDMS = 1.43.

5.3. Apparatus:

The experimental apparatus presented here provides a system whereby the film thickness in a lubricated, compliant contact can be measured using optical interferometry.

There are two primary mechanical variables associated with the lubricant film thickness and profile shape; entrainment speed and applied load. The mechanical system is designed so that these can be varied and controlled. To obtain a stable and steady film thickness the system must also be free of vibration.

5.3.1. Arrangement:

The complete experimental arrangement is shown schematically in Fig. 5.5. The tribological contact consists of a rotating elastomer ball pressed against a transparent optical flat. The optical window is a plain BK7 glass prism (Edmunds Optic, UK), which is naturally hydrophilic and was used as supplied. The prism has a Young's modulus of 65 GPa, Poisson's ratio of 0.24 and refractive index of 1.517. The prism is kept stationary while the ball rotates, so the system operates in pure sliding conditions.

The PDMS test ball is mounted on a horizontal drive shaft within the sample pot and loaded against the prism from below to allow optical access of the contact. Lubricant is entrained into the contact by test specimen rotation; the lubricant level for each experiment was filled to such a level to ensure liquid entrainment, *ca* 40 ml.

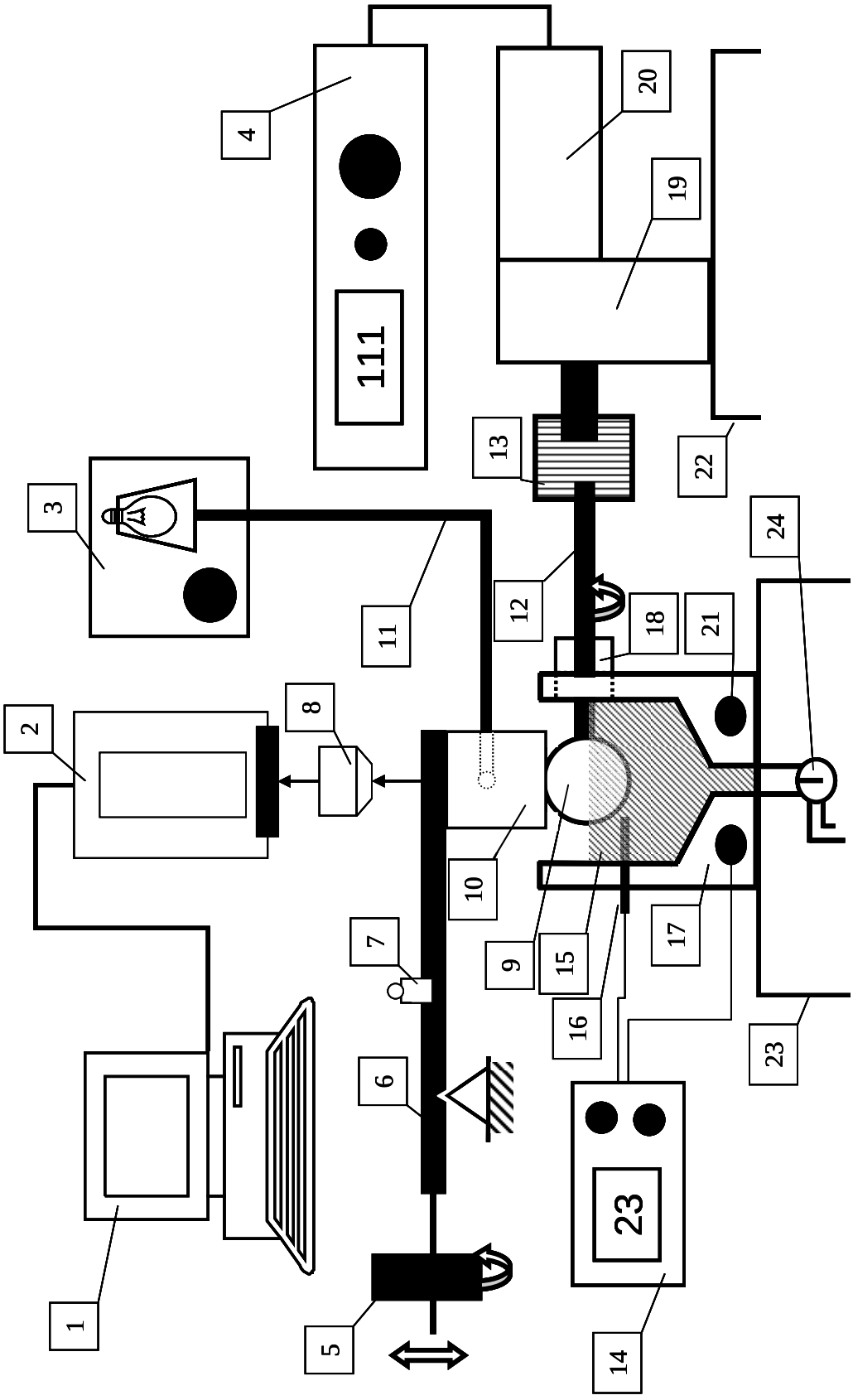

Figure 5.5. Schematic representation of experimental apparatus

Table 5.1. *Key for Fig. 5.1.*

1. Computer	9. Compliant test specimen	17. Sample pot
2. EM Camera	10.Optical window	18. Bearing house
3. Monochromatic light source	11. Light guide	19. Reduction gear box
4. Motor controller	12. Ball drive shaft	20. Ball motor
5. load beam balance	13. Coupling	21. Heating element
6. dead weighted load beam	14. Temperature control unit	22. Drive motor and gear platform
7. Calibration weights	15. Lubricant reservoir	23. Specimen, optical and load platform
8. Objective lens	16. Temperature sensor	24. Lubricant drain valve

5.3.2. Drive system

The experimental specimen is driven by an electrical motor connected to a 100:1 reduction gear box. To reduce vibrations that may interfere with film thickness measurements, the motor is directly connected to the reduction gear box *via* a bevel gear and mounted on to a separate pedestal from the specimen platform. The electric motor is a DC permanent magnet servo motor (Electro-craft Corp, UK). The motor acts as its own tachometer and changes in torque are detected by a bridge circuit which match the voltage to the control regulator. The motor speed is manually controlled by adjusting the input voltage to the regulator.

The motor and reduction gear box combination allows for a low entrainment speed range of 1 μm s^{-1} to 3 mm s^{-1}. The entrainment speed, *U*, is defined as;

$$U = \frac{u_b + u_d}{2} = \frac{u_b}{2} \tag{5.15}$$

where u_d is the speed of the glass window, in this case $u_d \equiv 0$. The ball speed, u_b can be calculated by;

$$u_b = \frac{u_m}{60}.gr.2.\pi.r_b \tag{5.16}$$

where u_m is the motor speed in rpm, gr the reduction gear box ratio and r_b the radius of the test specimen.

Low entrainment speeds were required to keep lubricant film thickness within measurable levels, as film thickness approaches 2 μm visibility of fringes is lost. Internal friction and torque losses, which may cause errors in entrainment speeds, are assumed to be negligible due to the high torque output of the reduction gear box. The greatest motor rotational speed required is 600 rpm which achieves an entrainment speed of *ca* 3 mm s^{-1}. At greater entrainment speeds, vibrations from the motor caused a pulsing motion in the contact, creating difficulty in obtaining true and accurate results.

5.3.3. Heating and sample pot

Two cartridge heating elements (RS, UK) provide indirect heat transfer to the lubricant. The heating elements are installed within the sample pot. To improve conductivity between the contacting surfaces, the heating elements are coated with a commercially-available heat transfer compound. The lubricant temperature is monitored *via* a temperature sensor within the lubricant bath. The sensor feeds back to a controller where the desired temperature can be inputted. The system allows lubricant temperature to be accurately controlled within ± 0.1 °C. A maximum temperature of 150 °C can be achieved and the lowest temperature is limited to room temperature *ca* 22 °C.

5.3.4. Test specimens: creation and properties

Test samples were fabricated from a component silicone kit (Sylgard 184, Dow Corning Corporation, USA). The PDMS is supplied as a two part silicone elastomer kit, a base and a curing agent. The test specimens in this thesis were a 'near' spherical PDMS ball created using a 'candle dipping' process. Uncured PDMS is layered onto a 19 mm diameter stainless steel ball until a coating of 1-2 mm in thickness is created. It is assumed that the steel substrate has negligible effect the mechanical properties of the PDMS layer, the implications of which are discussed further in chapter 6.4. The PDMS is transparent so reflections from within the specimen or the metallic sample mounting will interfere with the signal of interest. An opaque filler was therefore added to the PDMS to prevent this by absorbing any non-reflected light. Only a small amount is required for this to be achieved and 0.5 wt % Carbon black (Fluffy, Cabot, UK) was added to the uncured PDMS solution. The refractive index of the CB-filled PDMS was measured as 1.43 using an Abbe 60 refractometer (Bellingham and Stanley Ltd). PDMS samples were created according to the instruction manual of the manufacturer (Dow Corning). A base to curing agent mass ratio of 10:1 was used for all elastomer samples. The PDMS and CB solution was thoroughly mixed by hand and foams generated during mixing were removed by a vacuum. Once free of bubbles, the steel ball was dipped into the mixture and placed into an oven. The thin layer of PDMS cured rapidly at 150 °C within *ca* 3-5 minutes. The ball was then dipped into the PDMS mixture again and placed back into the oven. This process was repeated until the steel surface was no longer visible and the PDMS is *ca* 1.5 mm thick. The specimen was then placed in the oven overnight at 75 °C.

Surface analysis of the CB filled PDMS specimens were carried out using a Wyko optical interferometer (Veeco, UK). Measurements were taken in the VSI mode and the camera was setup with a X20 objective lens. Images are 640 x 450 pixels, which equates to a field of view of *ca* 575 x 430 μm. No filtering was used during all

measurements. A smooth surface finish of R_a = 70 ± 10 nm was achieved. These values satisfy the optical requirements of the experimental technique.

An SEM image of the PDMS surface is shown in Fig. 5.6. The CB particles can be seen to have conglomerated together during the curing process and to protrude from the PDMS surface.

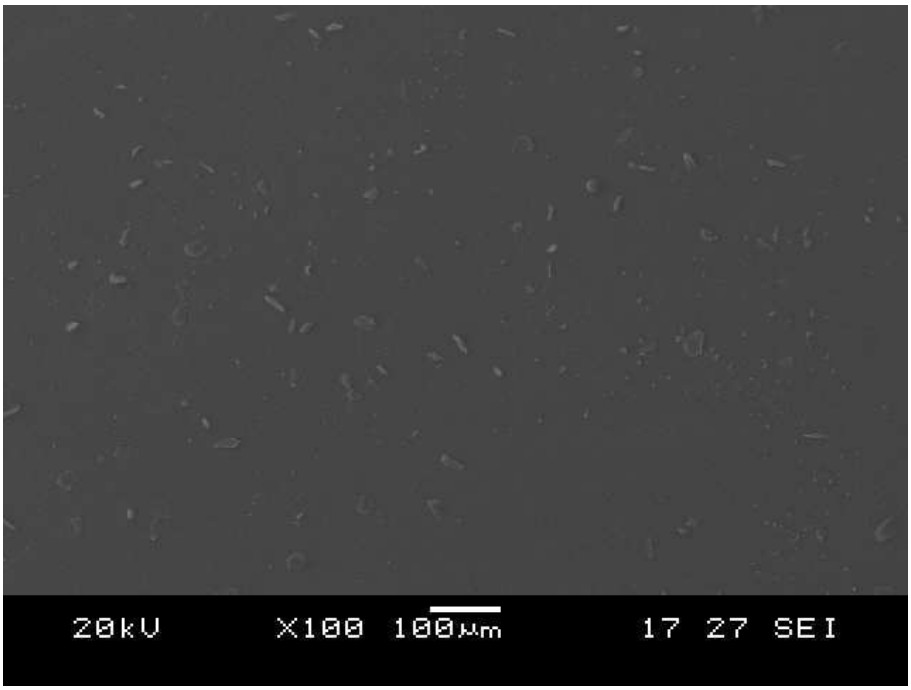

Figure 5.6. SEM image of CB filled PDMS test specimen. CB particles can be seen on the surface of the PDMS.

PDMS is a viscoelastic material. Therefore, the mechanical properties vary depending on test conditions, *i.e.* loading frequency or temperature. The concentration of filler has a large effect on the resultant elastic modulus. This has led to a number of elastic moduli of PDMS being reported in the literature; 2.4 MPa by Bongaerts *et al.* [25] when no filler was used and 4.1 MPa by de Vicente *et al.* [31] when MgO pigment was present in the PDMS. From dynamic mechanical analysis (DMA, Triton, UK), under test conditions appropriate to the contact studied, an elastic modulus of 3.8 MPa was obtained for the CB-filled PDMS. A Poisson's ratio of 0.49 was assumed for all tests [18].

5.3.5. Test lubricants

Table 5.2 lists the main lubricants employed in this study and their dynamic viscosities at the test temperature.

Table 5.2. *Dynamic viscosities of Test Lubricants*

Lubricant	Composition	Viscosity at 22 °C (Pa s)
GLY	95 wt.% Glycerol in water	0.38
SFO	Sunflower oil	0.053

Two test lubricants were used, a 95 % glycerol/water solution (GLY), η = 0.38 Pas and lab grade sunflower oil (SFO), η = 0.053 Pas, supplied by Unilever (Colworth). These were selected as they possess the same refractive index, n = 1.47, but differ in dynamic viscosity range by an order of magnitude. The refractive indices of both lubricants were measured at atmospheric pressure using an Abbe 60 refractometer (Bellingham and Stanley Ltd.). Under the test conditions used, the contact pressures were assumed to be too low (less than 1 MPa) to have any significant effect on the refractive indices of the test lubricants. Based on their refractive indices, the calculated fringe visibility for both lubricants was 96 %.

Glycerol is hygroscopic in nature, to limit possible errors in viscosity a 5 wt.% solution water in glycerol was preferred to pure glycerol. Since its viscosity is far less sensitive to small changes in water content than pure glycerol [96] and it is also much less hygroscopic.

Both the lubricants studied were single phase and Newtonian over the range of shear rate from 1 to 1000 s^{-1}, which spans the test parameters. The viscosities of the test lubricants were measured using a Stabinger Viscometer (Anton Paar, UK) prior to

testing. The test temperature was T = 22 ± 2 °C. The water used in the GLY solution was demineralised filtered water (Elga) while glycerol was supplied as 98 % pure grade (Sigma Aldrich, UK).

5.3.6. Microscope and image capture

The interference fringes were observed through a microscope, adjustable along three axes. A magnification of 5X was found to be convenient for observing both the Hertzian region and inlet/outlet lubrication across the range of test loads. An Olympus MDplan 5 with a numerical aperture of 0.1 and 19 mm working distance was used for all tests.

No eyepiece is needed for the experimental setup as a live image feed is given through the digital camera. Due to the poor reflectivity of the contacting surfaces an image-intensifying camera was needed to capture the interferograms. Images were captured using a Rolera MGi B/W EMCCD camera (QImaging, UK). The Rolera has a 14 bit senor dynamic range (16384 levels of distinguishable difference) offering high resolution of intensity levels. Images were captured at a series of entrainment speeds, beginning at a low value and increasing in stages. Images were captured as 16 bit tif files, in a 512x512 array. Due to the memory intensive nature of the camera, image sequences over 100 MB in size were captured and transferred to a PC. Connection to the PC was achieved via IEEE 1394 FireWire cable, which is capable of large data transfer at high speeds.

5.3.7. Light source

Contacts were illuminated with monochromatic (λ = 625 - 635 nm) light. An adapted fibre optics light source (Ealing), 12V AC supply, fitted with a size MR16 lamp and 150W Halogen bulb, was used for all experiments. To produce monochromatic light the bulb was replaced with a 20 W LED (TruOpto, UK). The AC supply was switched to DC and smoothed using a series of large capacitors and diodes. The light was guided to the glass prism via a fibre optic cable, resulting in a highly coherent beam of red light.

5.3.8. Loading system

For 1 N-order loads used in friction work, the contact area becomes too large to capture with the imaging system used in this investigation. Therefore, a loading system that can accurately apply and maintain a constant low load was needed. Load was applied to the test specimen through the prism by means of a dead weighted lever arm, shown schematically in Fig. 5.7. A balance weight is attached to the outer end of the lever arm upon a screw thread. The lever arm is pivoted on a knife edge which is vertically adjustable. This combination allows the prism to be lowered onto the contact under zero load or 'just touching' conditions. The 'record needle' style balance also produces a constant load, as the load arm can adjust to any misalignments in mechanical parts and eccentric behaviour in the sample rotation at low speeds, assuming low friction in the knife edge pivot.

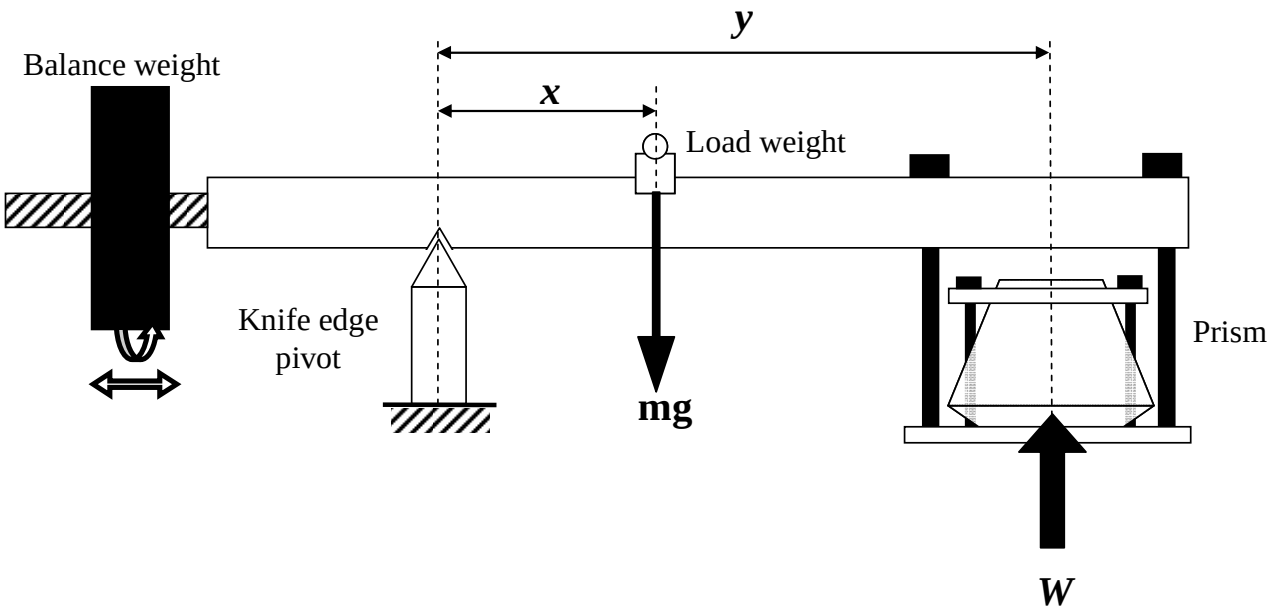

Figure 5.7 schematic of loading system (not to scale).

Taking moments around the knife edge pivot, the applied load can be calculated as;

$$W = \frac{mg.x}{y} \tag{5.17}$$

where x is the distance from the pivot point A and the centre of the calibration mass, m. y, the distance between pivot point A and the centre of the optical window and g is the gravitational constant (g = 0.98 m s^{-2}). With this system the normal load can be varied in increments of 1 mN.

5.3.9. Calibration

In a hard/metallic interferometric system, the absolute thickness corresponding to each fringe of the systems must be determined by calibration. This is necessary because of phase changes associated with the metallic reflections of the steel ball and the semi-reflective chromium layer. In the current, compliant contact, due to the

absence of any reflective coatings on either contacting surface it is assumed that there will be no anomalous phase changes in the tribological contact of interest.

If zero thickness gives black interference, corresponding to zero reflected light intensity (minimum), then an optical gap of λ/4 will give bright interference of high intensity (maximum). This is only true if the phase change is equal to 180° at the liquid rubber interface. To obtain precise determination of this phase change, ellipsometric measurements were carried out by Roberts [72] who found that the phase change was between 0.5° to 2° less than 180°. However, these measurements were made for a single surface in air and not the contact pair in liquid. Photometric measurements, in this investigation and by Tabor *et al.* [68], showed that, for the tribological contact, the light reflected from the interface has, within the sensitivity of the apparatus, zero intensity. This implies that the effective phase change is virtually 180°.

The zero film thickness fringe colour (maxima or minima) is determined at the beginning of each test run. For a compliant contact, such as the one used in the present study, rapid approach of the surfaces traps a 'bell' of liquid in the centre of the contact and the entrapped lubricant is squeezed out over time under static conditions [67,72]. To achieve an accurate calibration the contact was therefore left for 10 minutes before the interferogram was captured, and the zero film thickness level obtained.

5.4. Conclusion on interferometry method

a) The system discussed here has been designed to meet the requirements of obtaining good fringe visibility despite the low reflective nature of the elastomer surface, using low power monochromatic illuminating light. The reflectivities of the contacting surfaces must be balanced in such a way that they provide interfering rays of similar intensity (i.e. $I_1 = I_2$). By removing the semi-reflective

chromium layer used in the more common, metallic interference studies, this is possible. The introduction of a prism in place of a glass disc to move the illuminating light to a non-normal incidence reduced the surface reflections and back scatter from outside the contact.

b) Fringe intensity changes from maximum to minimum (or vice versa) when the thickness changes by $\frac{\lambda}{4n}$. Therefore, to obtain fringes of high visibility, the contacting surfaces must be optically smooth. In other words they must have a surface roughness less than $\frac{\lambda}{4n}$. Surfaces less than *ca* 100 nm in surface roughness are therefore required for the system used here. The glass prism and PDMS samples satisfy this condition.

c) The type and method of illumination required to give good fringe visibility is a function of the experimental film thickness range. For lubricated, compliant, contacts the range of film thickness values is large. Monochromatic interferometry is best suited to this requirement.

d) A sufficient degree of coherence between the interfering beams must be maintained over the required film thickness range. Beyond these boundaries the visibility will fall and eventually interference will be lost.

Chapter 6

An investigation of lubricant film thickness in sliding compliant contacts

In this chapter film thickness results are presented for two simple Newtonian fluids. Film thickness measurements were made using the monochromatic optical interferometric technique discussed in the previous chapter. Film thickness maps and profiles across a range of applied loads and entrainments are shown. Pressure profiles are also presented and discussed. Film thickness maps are compared to a theoretical model.

The work in this chapter can be found in: Myant C, Fowell M, Stokes J R, Spikes H A. "Film thickness study for lubricated, compliant, contacts". doi: 10.1080/10402001003693109

6.1 Test conditions and procedure

The experiments described here were conducted using the experimental method described in chapter 5. A pure sliding compliant contact, consisting of a rotating CB-PDMS ball loaded against a plain glass prism was used. Two lubricants were tested; glycerol (GLY) and sunflower oil (SFO). All tests were carried out at room temperature (T = 22 ± 2 °C) under three different applied loads of W = 3, 35 and 50 mN. A small lubricant entrainment speed range of U = 0 to *ca* 1.5 mm s^{-1} was investigated.

Before each test the ball was cleaned by rinsing in distilled water and then a solution of 2% wt. sodium dodecylsulphonate in distilled water, followed by immersion in isopropanol in an ultrasonic bath for at least three minutes, and finally by immersion in deionised water in an ultrasonic bath for at least three minutes. The glass prism was ultrasonically-cleaned in isopropanol, followed by Analar acetone.

Once the test rig was assembled *ca* 60 ml lubricant was added to partially submerge the ball. Load was then applied and interferograms taken at a series of entrainment speeds beginning from a low value and increasing this in steps.

6.2 Interference images to film thickness maps

A series of typical, cropped, low-speed interferograms obtained in this study are shown in Fig. 6.1.a), b), c), and d). These were taken at U = 0.02, 0.25, 0.33, 1.31 mm s^{-1} respectively, all at an applied load of W = 3 mN, lubricated with GLY. Lubricant flows along the x axis from left to right. Interferograms were captured as 512x512 pixel arrays, with a calibrated pixel size of 3.2 μm giving a full field of view of 1.64x1.64 mm. The monochromatic system shows good detail in film shape

and it can be seen that, for all the images, the minimum film thickness occurs at the lubricant outlet.

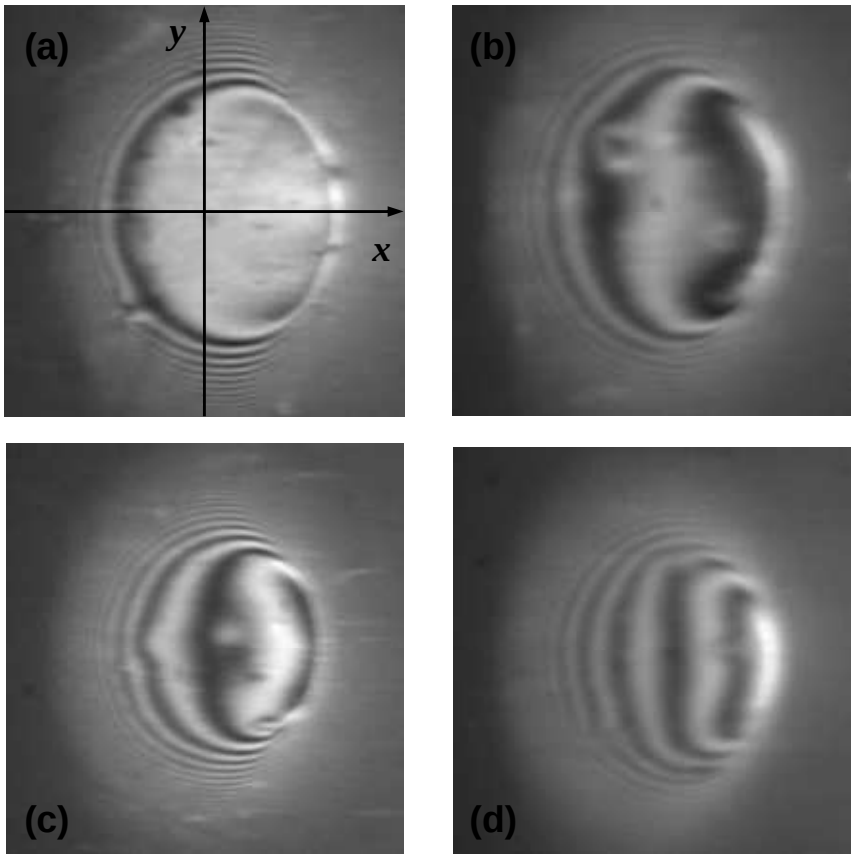

Figure 6.1. Interferograms of the tribological contact under 3 mN applied load, lubricated with GLY. At U = 0.02, 0.25, 0.33 and 1.31 mm s^{-1} for images (a), (b). (c) and (d) respectively. Images are ca 0.6x0.6 mm is size. Lubricant flows from left to right, in the x direction.

Film thickness maps were extracted from Figs. 6.1.a) to d) by image analysis and are shown in Figs. 6.2.a) to d). A full *x-y* coordinate map of the fringe positions, number and intensity was built up for each image. To do this, columns with less than one full fringe and all intensity data outside the first and last fringes detected were filtered out. The minimum fringe number, it's position and film thickness value were inputted from which all film thickness values are then calculated. The minimum film thickness fringe was used as the datum point due to the certainty in its location. The minimum film thickness value was obtained by manually counting

fringe changes at the rear of the contact from zero entrainment speed upward. For film thickness values between maxima and minima values, the grey scale intensity was used to interpolate between points. This was similar to the procedure used by Roberts *et al.* [68]. By including all grey scale data, the correct shape of the contact could be obtained, in particular the shape and extent of the outlet constriction. Another benefit of this technique is that surface roughness can also be plotted. The system can only count upward changes in phase; therefore to avoid confusion between phase changes due to asperities, areas of the image can be selected that are to be ignored during fringe mapping. This allows asperities to be initially ignored and then re-inserted during interpolation of grey scale data. Before a final film thickness map of the contact area was produced, any spurious fringes which have formed as a result of asperities or dirt/interference detected beyond the main contact region, were removed. Any columns within the contact area where no fringes are detected are assumed to be the average of their immediate neighbours.

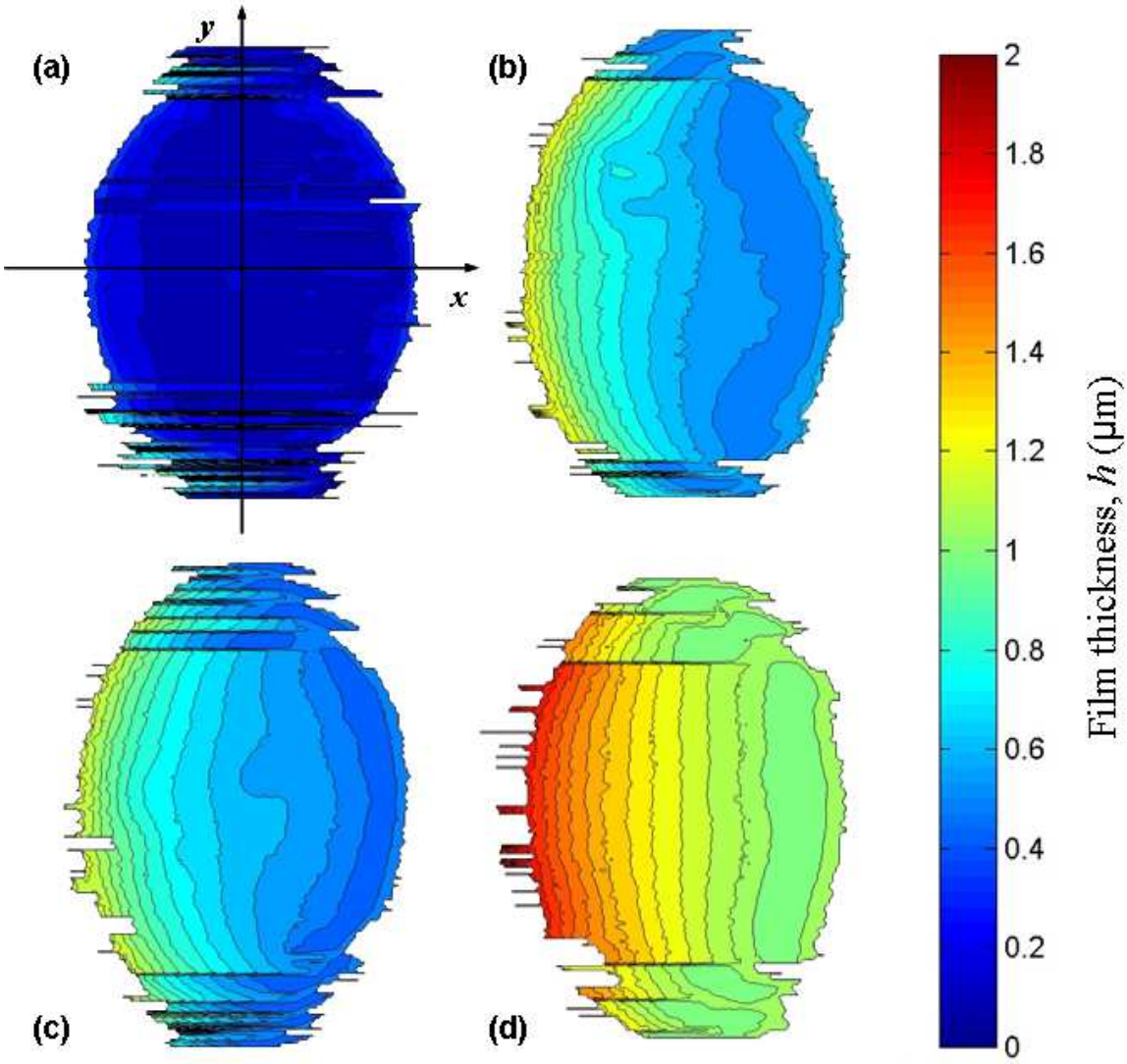

Figure 6.2. Film thickness maps of the tribological contact under 3 mN applied load, lubricated with GLY. At U = 0.02, 0.25, 0.33 and 1.31 mm s^{-1} for images (a), (b), (c) and (d) respectively. Lubricant flows from left to right, in the x direction. Film thickness is expressed as RGB intensity, values indicated in the colour bar to the right of the figure.

For each case in Figs. 6.1 and 6.2, the minimum film thickness occurs directly behind the centre of the contact. At low values of *U*, two regions of minimum film thickness occur, close to the centre line and at the sides. Although this is not clearly shown in the film thickness maps because of the coarseness of the grey scale analysis, it is suggested in the interferograms. These side lobes have been predicted

numerically by Hamrock and Dowson [97] and demonstrated experimentally by Roberts *et al.* [68].

6.3 Results

6.3.1 Effect of Load

Film thickness profiles along the x axis (in the entrainment direction at $y = 0$), were obtained by the same method as that used to create film thickness maps discussed above. Profiles of the tribological contact lubricated with GLY at similar entrainment speeds, for three different applied loads, are presented in Figs. 6.3.a), b) and c). The minimum film thickness position was used as a universal reference point to compare the plots. The central contact point was not used as no externally-based geometrical reference system was available during experimental testing. This is the case for all subsequent figures. The profiles show details of film shape and, in particular, the minimum film thickness located in the outlet region. Surface topography and asperities are also visible from interpolation of grey scale intensity between fringes.

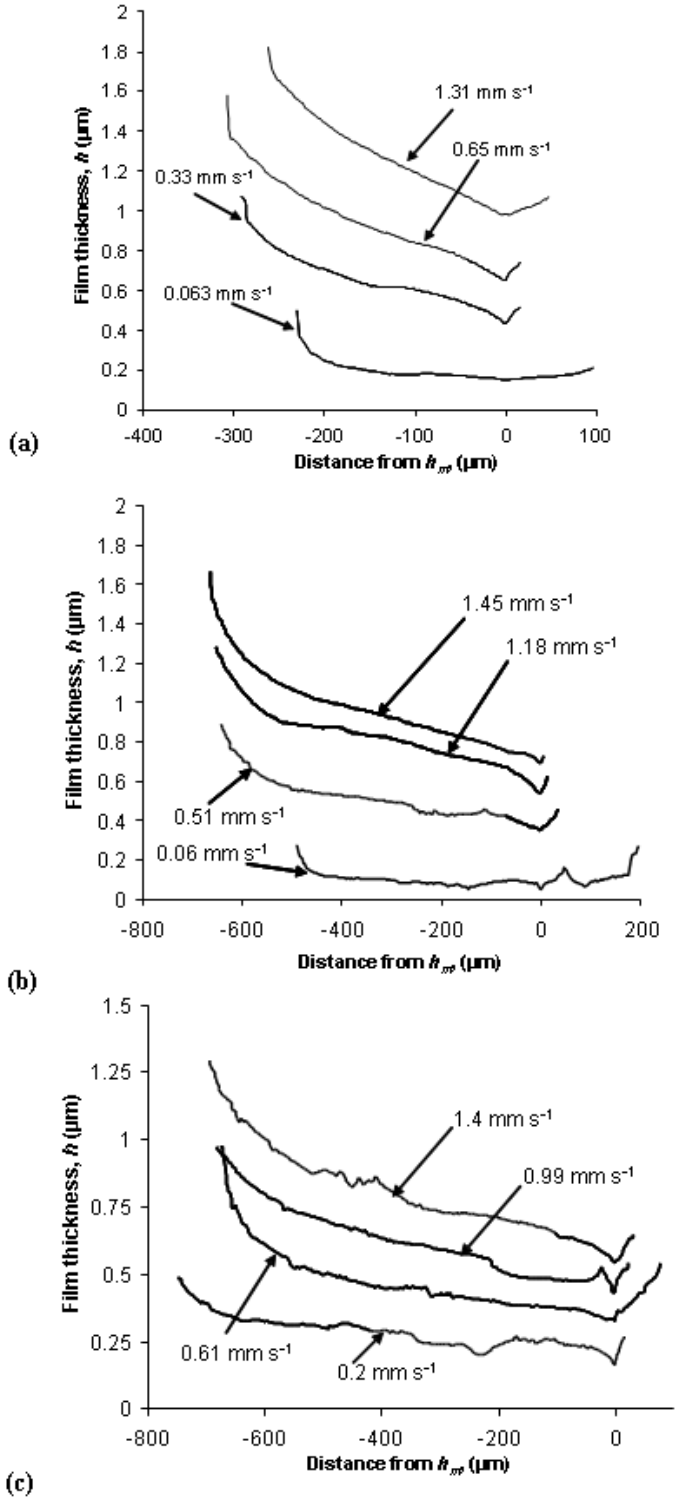

Figure 6.3. Film thickness profiles for GLY at applied loads of (a) 3 (b) 35 and (c) 50 mN.

GLY profiles show some variation in contact size; this was most notable at 50 mN load, Fig. 6.3.c). In profiles at U = 0.2 and 0.61 mm s^{-1}, the contact size appears to vary by about *ca* 100 μm. This suggests a possible error in load of 1 to 2 mN may be occurring. The contact size at 3 mN load, shown in Fig. 6.3.a), appears to vary by *ca* 40 μm, while at 35 mN load, contact size variation appears to be negligible. This may be a result of vibrations in the test apparatus, and illustrates the sensitivity of I-EHL lubricant films to load, unlike piezoviscous-EHL.

As load was increased, noise in the profile plots also increases. The larger contact size raises the likelihood of asperities being present. Asperities do appear to be present in a number of the profiles, most notably for profiles at low film thickness values; however this would not cause noise along the entire profile. At higher loads, surface roughness effects may be more visible due to the lower film thickness values. Film thickness values were below the peak to valley height of 1 ± 0.2 μm, however they were still above the roughness, R_a.

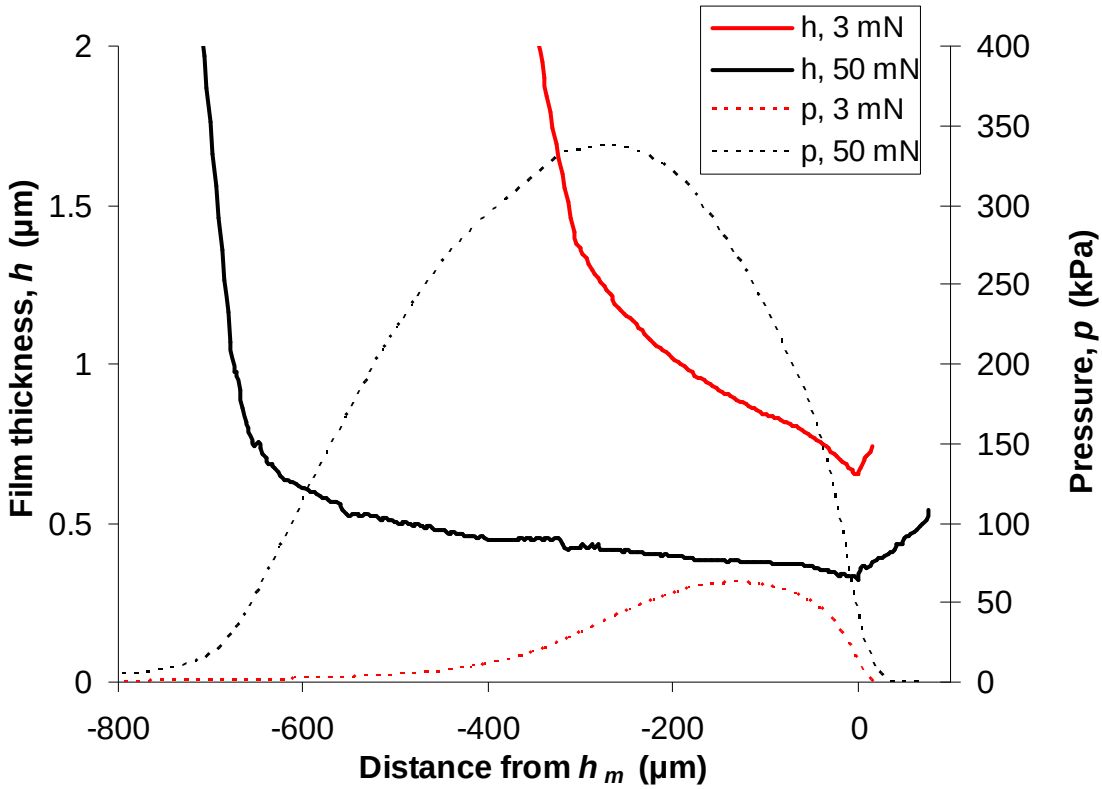

Figure 6.4 Film thickness (solid lines) and pressure (dashed) profiles for W = 3 mN and 50 mN, at U = 0.65 and 0.61 mm s^{-1} respectively, for tribological contacts lubricated with GLY.

Figure 6.4 compares film thickness and pressure profiles, along y = 0, for the tribological contact lubricated with GLY under 3 and 50 mN applied load. Film thickness profiles were taken from Fig. 6.3.a) and (c) at similar entrainment speeds of 0.65 and 0.61 mm s^{-1}, respectively. To calculate the pressure profiles, the film thickness profiles obtained from interferometric measurement were extended to five times the Hertzian radius on the inlet side. This was achieved by assuming the contact profile returns to the radius of curvature of the ball at radii outside the measured interferometric profiles. The pressure profiles were calculated by an inverse method based on inputting the experimentally-measured film thicknesses to a numerical Reynolds equation solver as described by Cameron [98]. The solver discretised the domain using finite differences and any pressures below the gauge pressure were set to the gauge pressure. Film profiles at the same applied load show similar areas under the pressure curves, as expected.

In Fig. 6.4, it can be seen that the maximum pressure occurs just downstream of the centre of the contact for the low load case. However for the high load case, the maximum pressure occurs closer to the Hertzian centre. This was predicted by Hamrock and Dowson [97]. For an order of magnitude change in the applied load there is a considerable change in the pressure profile of *ca* 6 times p_{max}. However there is a less significant change in the film thickness profile, only a change of *ca* 2.5 *h*.

Figure 6.5.a) and b) show the central and minimum film thickness values respectively, for applied loads of 3, 35 and 50 mN for the tribological contact lubricated with GLY. Theoretical predictions from Eqs. (2.3) and (2.4) are also shown as solid or dashed lines. In hard, metallic contacts, the central film thickness, $h_{c,}$ is normally positioned on a flat plateau region bounded by the horseshoe shaped constriction, making it a significant value as it describes a large proportion of the contact. For compliant contacts h_c is less significant, due to the exit constriction being restricted to the rear of the contact, *i.e.* not developing side lobes and the majority of the contacts forming a hydrodynamic wedge. Therefore the position of the h_c, was simply defined as the middle of the detected profile.

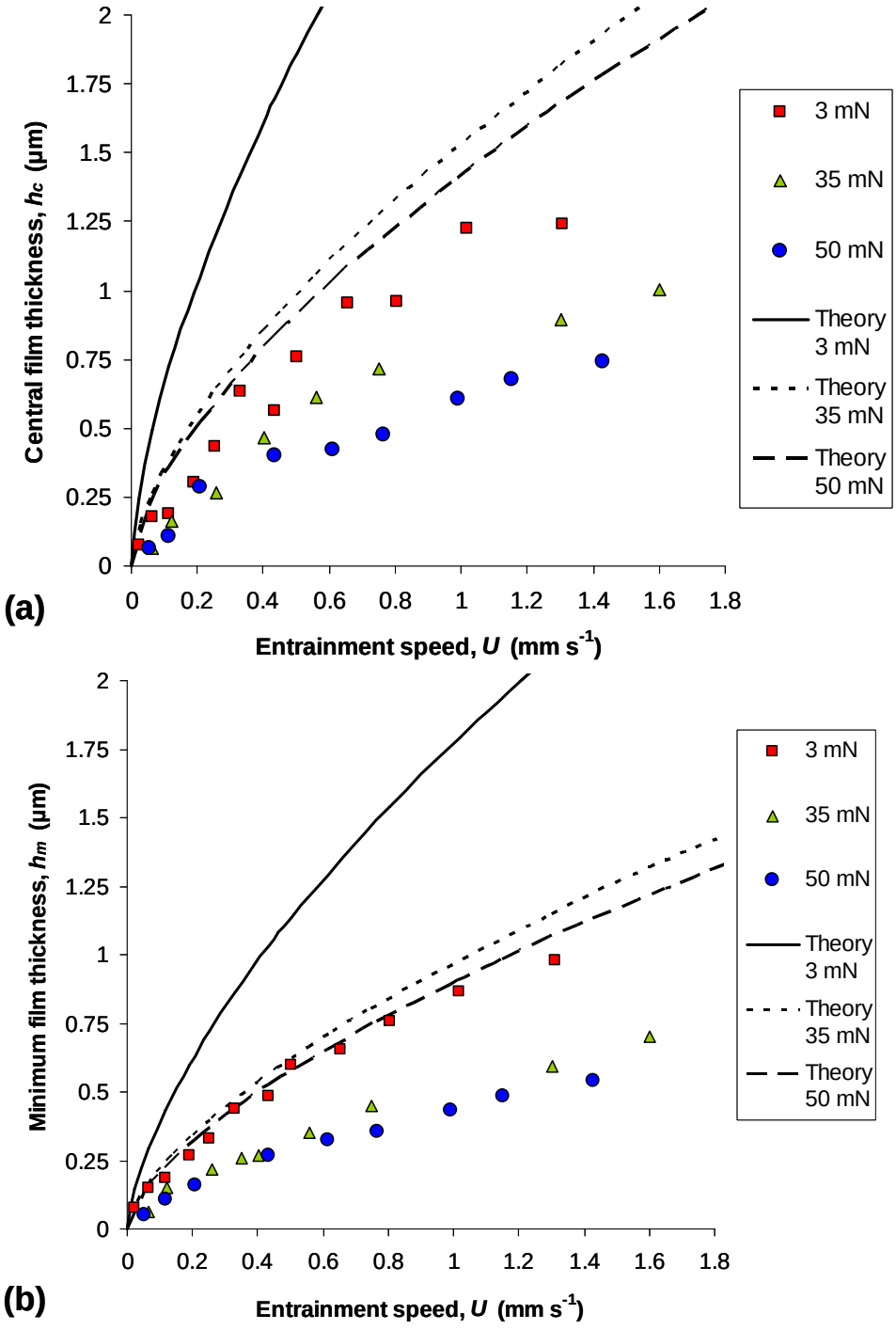

Figure 6.5. Measured (a) central film thickness and (b) minimum film thickness values at W = 3, 35 and 50 mN for the tribological contact lubricated with GLY, across the entrainment speed range of 0 to 1.8 mm s^{-1}. Theoretical predictions from Eqs. (2.3) and (2.4) are also shown as solid or dashed lines.

It can be seen in Fig. 6.5 that theoretical predictions for central and minimum film thickness are somewhat larger than the experimentally obtained values. Previous investigations into the liquid film thickness of compliant contacts lubricated with GLY, carried by Bongearts *et al.* [19], also observed lower experimental values than theoretically predicted. This discrepancy between numerical predictions and experimental values was ascribed to a drop in the lubricant viscosity as a result of thermal effects and the hygroscopic nature of glycerol. Good agreement with Eqs. (2.3) and (2.4) was achieved for GLY by using a lowered effective viscosity of 0.15 Pas. For such a viscosity drop in GLY to occur a temperature rise of *ca* 10 °C must take place, or an increase in the water concentration of *ca* 10 % [96]. Individually these seem unlikely, although a combination does seem possible.

Bongaerts *et al.* [19] suggested that the required rise in temperature may be caused by the illuminating light. It was not possible to measure the temperature within the contact, only bulk lubricant temperature within the sample pot was monitored. No variation in this was observed. However, it seems unlikely for a change of more than a few degrees Celsius to occur as the light source is of low power/intensity.

It is also possible that shear heating of the lubricant in the contact might also result in a temperature increase and consequent reduction in effective viscosity. Due to its high viscosity, an increase of 10 °C in the test temperature will, for glycerol concentrations between 100 and 90 %, roughly half the lubricant viscosity [96]. An upper-bound estimate of the effect of such heating on temperature change, ΔT, can be estimated from a simple heat balance between the heat generated by shear and that removed by convection, assuming no heat conduction, *i.e*.

$$\dot{q} = \mu W u_s = m c_p \frac{\Delta T}{t} \tag{6.1}$$

where μ is the friction coefficient defined by Eq. (2.8), u_s the sliding speed, c_p is the specific heat capacity of the lubricant, m the mass of lubricant volume affected

($m = \pi a^2 h_a \rho$) and t the time taken for fluid to pass through the contact ($t = \frac{2a}{U}$). Where ρ is the density of the lubricant, a is the contact radius and h_a the average film thickness. Rearrangement gives;

$$\Delta T = \frac{\mu W u_s t}{\rho h A c_p} = \frac{2a\mu W SRR}{\pi a^2 \rho h c_p} \tag{6.2}$$

where *SRR* is the slide-roll ratio (ratio of sliding speed to entrainment speed = 2 for pure sliding).

For a density and specific heat of glycerol of 1250 kg/m^3 and 2400 J kg^{-1} K^{-1}, at W = 3 mN a = 0.18 mm and assuming an average film thickness of 1 μm at U = 0.65 mms^{-1}, as indicated in Fig. 6.3. Assuming the viscosity at the inlet, where the majority of the Couette friction arises, is the measured viscosity of 0.38 Pas, Eq. (2.8) gives $\mu \approx 0.1$. From Eq. (6.2) the subsequent temperature rise predicted for U = 0.65 mm s^{-1}, is *ca* 1.5 °C. However the actual value for temperature rise will probably be considerably less than this due to (i) heat conduction, (ii) the fact that Eq. (6.2) calculates the rise at the contact exit rather than the inlet where entrainment was established and (iii) the illuminating power was lower than that quoted due to it illuminating a larger area than the contact, so the power intensity over the contact was lower, and (iv) the power will be diminished by *ca* 4 % at each interface the light passes through (*e.g.* the lens surfaces). Even so, a temperature change of a few degrees within the contact seems possible, but insufficient to cause the observed discrepancy.

Bongaerts' other suggestion is that the glycerol in the test chamber, which is hygroscopic, will absorb water vapour from the atmosphere, lowering the fluid viscosity. To produce the apparent reduction in viscosity by dissolved water alone would imply a change on glycerol composition from 100% glycerol to *ca* 90% glycerol [96]. Such a large increase in water content seems unlikely. However, the relationship between glycerol and water content is non-linear. At high glycerol

purity a change of 1% in water concentration will produce a large change in viscosity. This coupled with other experimental errors may explain the discrepancy between experimental and theoretical values.

6.3.2 Influence of entrainment speed

Figure 6.6 shows central film thickness profiles at various entrainment speeds for SFO under 3 mN applied load. Profiles are taken in the direction of flow, at $y = 0$.

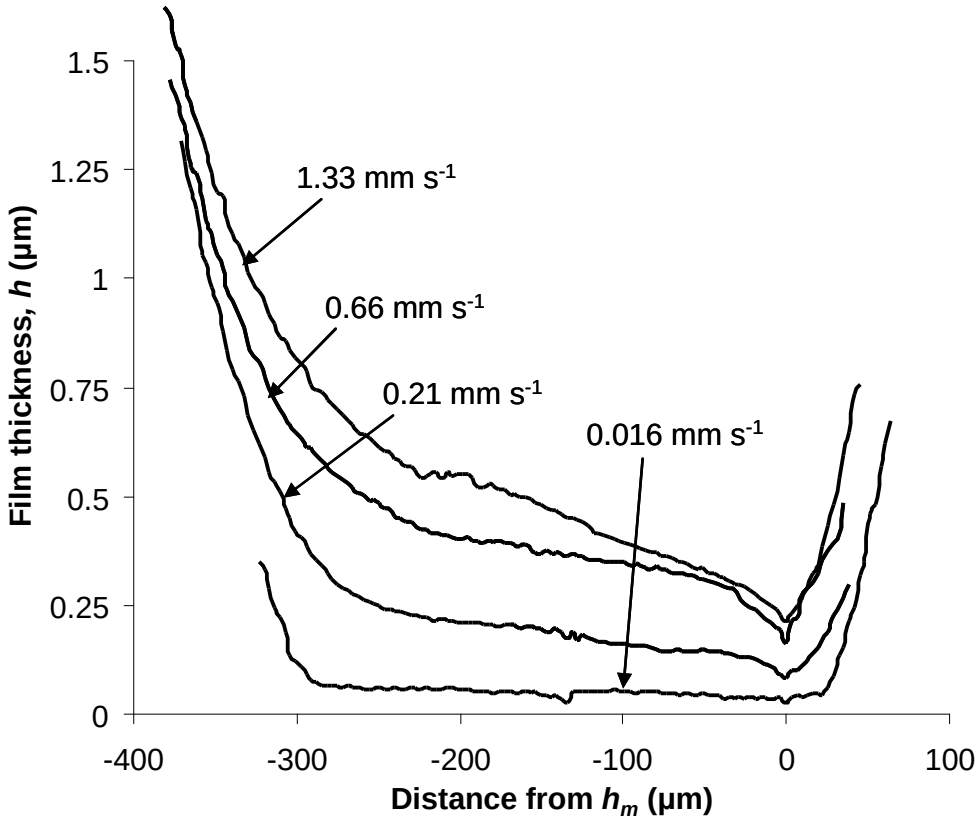

Figure 6.6. Film thickness profiles of the tribological contact lubricated with SFO, under 3 mN applied load at U = 0.016, 0.21, 0.66, 1.33 mm s^{-1}.

Compared to GLY there appears to be greater noise in the SFO plots. The test sample used may have been of a larger surface roughness. This is unlikely, however,

as noise is not present in results from Fig. 6.3 at similar values of film thickness for GLY. Since SFO and GLY were used as supplied, they may not necessarily be free of surface-active or micellar components or debris, which could build up within the contact area during testing and interfere with imaging. SFO is a natural product containing impurities, among which are surface active free fatty acids. This may have caused the difference in noise between the two test lubricants. Another possible reason for the difference in noise between images is errors/differences in focus.

Lubricant film thickness profiles for SFO at U = 0.66 and 0.21 mm s^{-1}, shown in Fig. 6.6, were used to calculate pressure profiles. The resultant pressure profiles along the centre line in the sliding direction are shown in Fig. 6.7. The pressure in the inlet region is greater for U = 0.66 mm s^{-1}. However, inside the contact, the values for the pressure are higher for the low speed case, U = 0.21 mm s^{-1}. As the entrainment speed and consequently the film thickness are reduced, the pressure approaches closer to the Hertzian profile. However even at the lower speed there is still a significant rise in pressure in the inlet region and the pressure profile remains skewed towards the exit region.

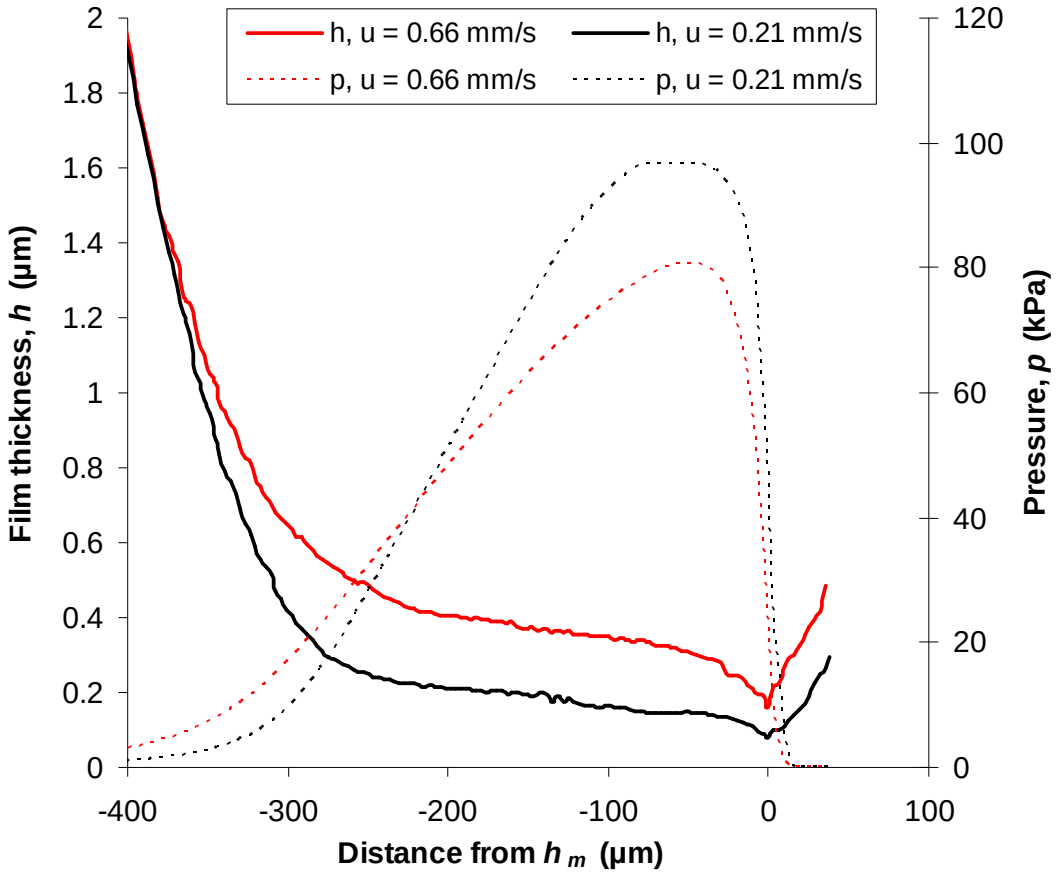

Figure 6.7. Film thickness (solid lines) and pressure (dashed) profiles for U = 0.66 (red) and 0.21 (black) mm s^{-1}, under 3 mN load.

6.3.3 Effect of viscosity

Figure 6.8 compares film thickness profiles and calculated pressure profiles for SFO and GLY, along y = 0, at 3 mN applied load. Profiles were taken from Fig. 6.3.a) and Fig. 6.6 at similar entrainment speeds of 0.65 and 0.66 mm s^{-1}, respectively. For the high viscosity fluid, GLY, the maximum pressure occurs near the Hertzian contact centre. The curved or near-hemispherical nature of the pressure plot is indicative of the wedge-shaped film thickness profile. However, for the lower viscosity fluid, SFO, the maximum pressure occurs just in front of the contact exit

region. For a one order of magnitude change in the viscosity there is a doubling of the maximum pressure and the film thickness.

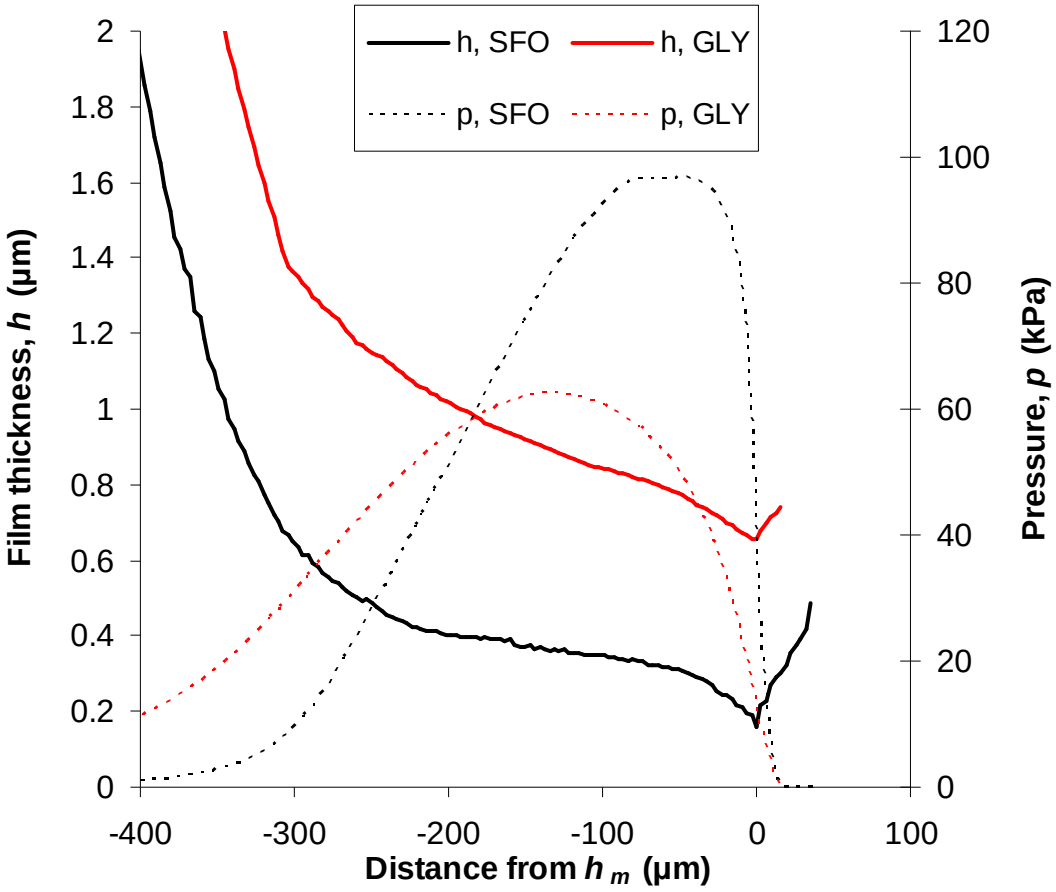

Figure 6.8. Film thickness (solid lines) and pressure (dashed) profiles for GLY (red) and SFO (black) under 3 mN applied load at ca U = 0.66 mm s^{-1}.

The pressure spikes found when dealing with materials of high elastic modulus [99] are not evident in these results for a low elastic modulus body in contact. The lack of a pressure spike is probably due to the lack of piezo-viscous effects of the fluid in the contact for compliant materials. This is in turn due to the fact that considerably less pressure is generated in a compliant contact than in a contact with high elastic modulus solids. This was predicted by Hamrock and Dowson [97].

It can be seen in Fig. 6.9 that both the experimentally measured GLY and SFO film thickness results are below the theoretical predictions. As discussed above, the

discrepancy in GLY has previously been ascribed to changes in the lubricant properties. However, SFO is not hygroscopic, nor is it subject to the same magnitude of change in viscosity with respect to temperature. A larger, unrealistic, temperature rise of 30 °C is needed to achieve the required change in viscosity for SFO [100]. This suggests that changes in lubricant properties is unlikely to be the main cause for the disagreement between theoretical and experimental film thickness values.

This leaves two possibilities; firstly it is possible that the contact was not fully-flooded. As stated at the beginning of the chapter, the sample pot is filled until the test specimen is partially submerged. Liquid is thus entrained into the contact by rotation of the PDMS ball. Due to the poor wetting nature of the PDMS surface lubricant may not flow back into the inlet track. This would reduce the inlet reservoir size and lower the overall film thickness. Starvation is investigated in chapter 8.

Secondly, the theoretical predictions may not be valid for the contact of interest, due to the low dimensionless speed and low parameters employed. Equations (2.3) and (2.4), generated from regression fits to numerical solutions by Dowson and Hamrock [97], were fitted to a range of values of $\overline{U}$ = 5x 10^{-9} to 5 x 10^{-8} and $\overline{W}$ = 0.2 to 2 x 10^{-3}. These predict somewhat larger film thickness values than the experimental measurements obtained in this study, over a range of values of $\overline{U}$ = 9x 10^{-12} to 5 x 10^{-9} and $\overline{W}$ = 3 x 10^{-6} to 5 x 10^{-5}. This may account for the disagreement between experimental and theoretical plots.

By varying the power law coefficients in Eqs. (2.3) and (2.4), the following best-fits were obtained, for both fluids, in all experimental conditions;

$$h_c = 3.3\overline{U}^{0.63}\overline{W}^{-0.13}R' \tag{6.3}$$

$$h_m = 2.8\overline{U}^{0.68}\overline{W}^{-0.20}R' \tag{6.4}$$

Equations (6.3) and (6.4) both show different dependencies on the speed and load parameters from Eqs. (2.3) and (2.4), which were derived from simulations of compliant contacts. It should be noted that a small change in the power law coefficients will produce a large change in film thickness values.

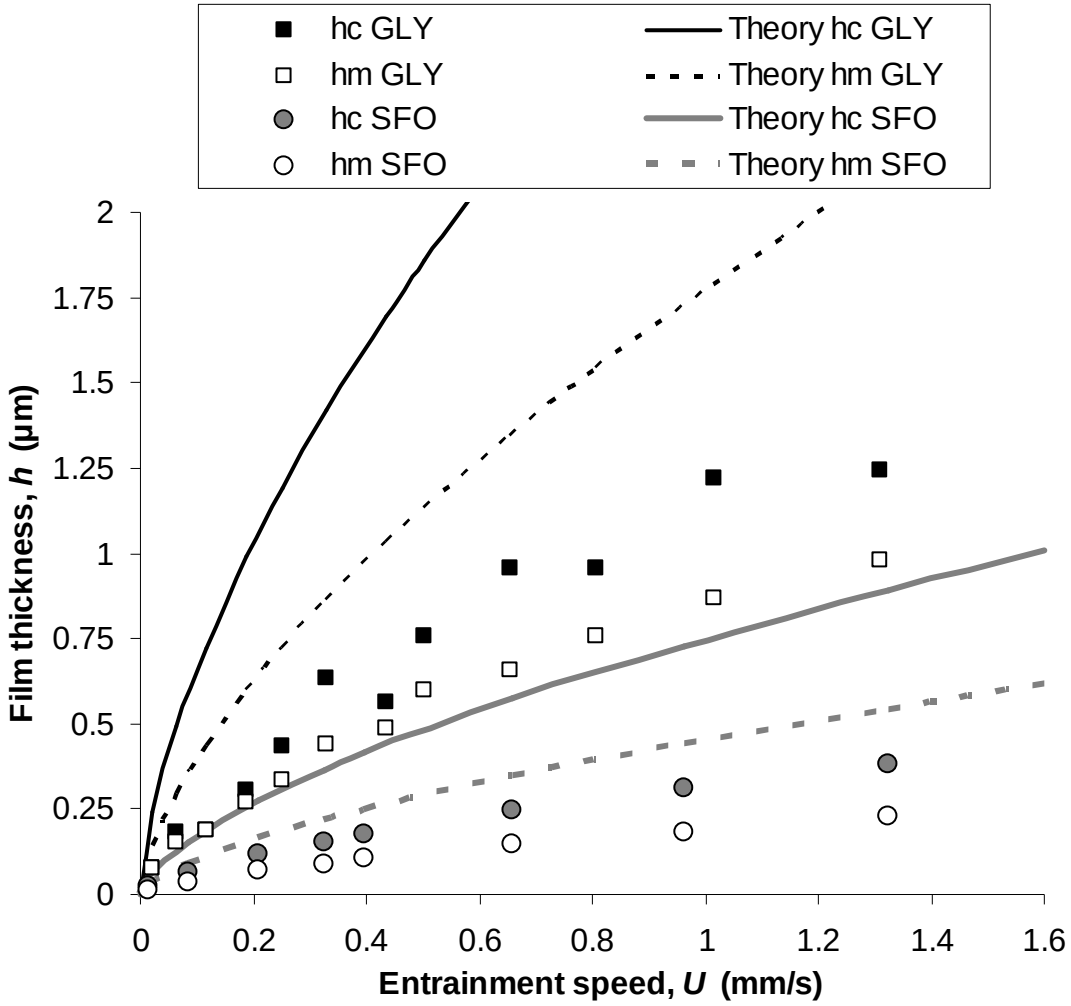

Figure 6.9. Measured central (solid) and minimum (open) film thickness values for GLY (squares), and SFO (circles) for the tribological contact under 3 mN applied load. Numerical predictions for central and minimum film thickness values, from Eq. (2.3) and (2.4) are plotted as solid and dashed lines respectively.

6.4 Theoretical profile shape

A full numerical solution for compliant EHL given by de Vicente *et al.* [31], was used for comparison with measured film thickness profiles. The solution approach was a standard finite difference one, with a 256x128 grid and Reynolds cavitation boundary conditions. Figure 6.10.a) shows the predicted film thicknesses obtained using de Vicente's model for the tribological contact of interest lubricated with SFO, at $W = 3$ mN and $U = 0.66$ mm s^{-1}. Compared to conventional EHL contacts, the 'horse shoe' outlet constriction, a characteristic of EHL contacts, is restricted to the exit, instead of extending towards the inlet region. In this I-EHL contact (Fig. 6.10.a) it can be observed that the film has a noticeable gradient within the Hertzian contact region, compared to conventional hard EHL contacts. In this way the film takes on a 'convergent wedge' shape similar to that used in many hydrodynamic bearings. It is likely that this 'wedge' is largely responsible for generating fluid pressure and therefore the load-carrying capacity of the contact.

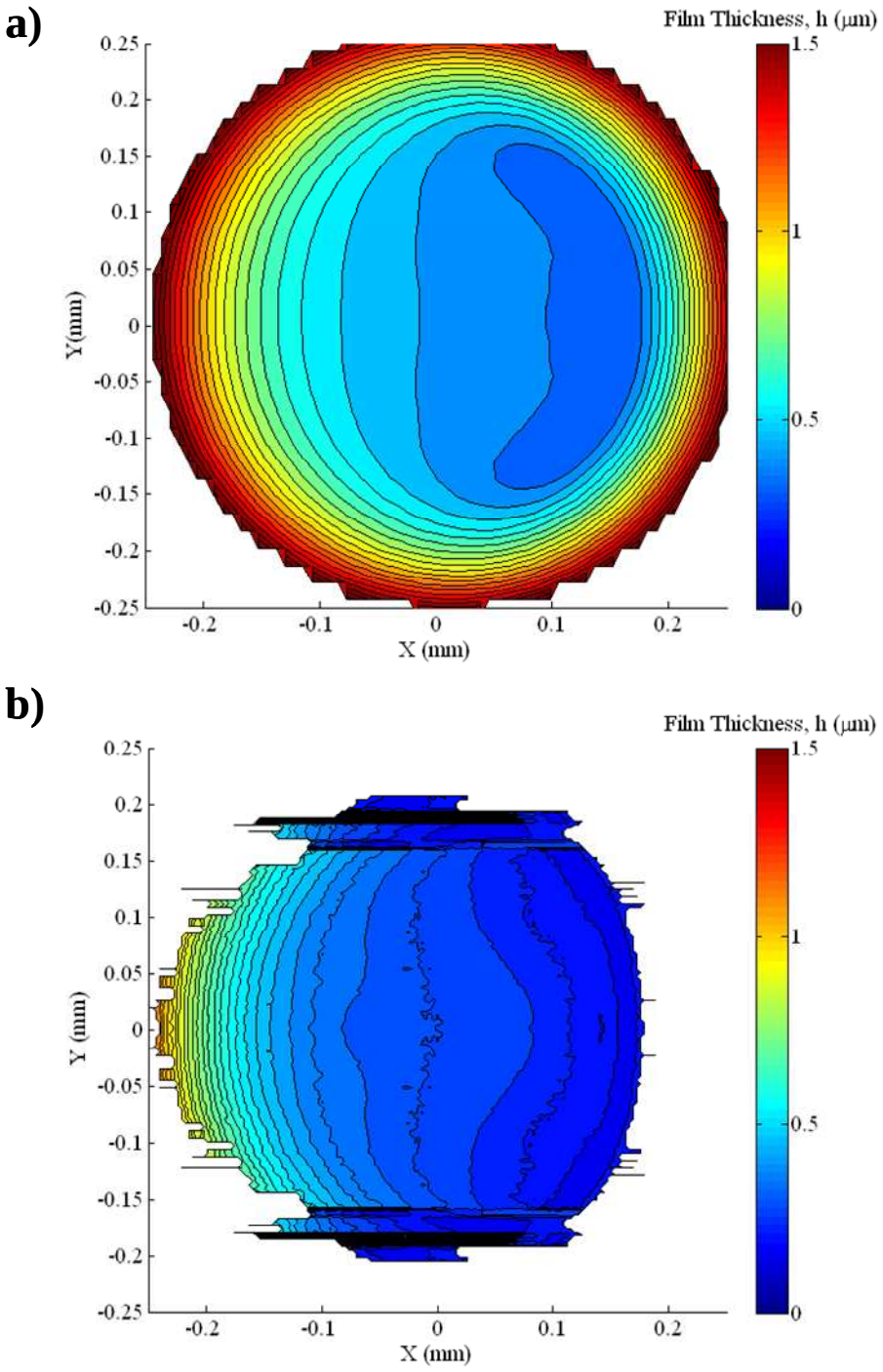

Figure 6.10. Film thickness maps of the tribological contact of interest under 3 mN of load and at U = 0.66 mm s^{-1}. a) de Vicente et al. model [31], b) Experimental result. Film thickness is expressed as RGB intensity values indicated in the colour bar to the right of the figure.

Figure 6.10.b) shows the corresponding experimental film thickness map for the tribological contact of interest lubricated with SFO, at $W = 3$ mN and $U = 0.66$ mm s^{-1}. It should be noted that the experimental result is symmetrical through $y = 0$. This is because only one half of the interference image was used in this case due to poor fringe quality in the left hand side and the left hand side shown is simply the mirror image of the right hand side. It can be seen that there is reasonable qualitative agreement with the theoretical results predicted by de Vicente's model. The experimental results show both a reduced horseshoe, which is limited to the rear of the contact, and a 'wedge' shaped film thickness profile within the Hertzian contact region. However quantitative agreement between absolute film thickness values was not achieved; the experiments showing a generally thinner lubricant film. This comparison is clearly shown in Fig. 6.11 where the central film thickness profiles are plotted. Across the main contact region the theoretical film thickness values are *ca* 0.075 μm greater than those experimentally measured. However, a larger difference, *ca* 0.2 μm, in the predicted and experimental minimum film thickness is observed. It would be expected that such differences in film thickness profiles, particularly the increased exit constriction of the experimentally measured profile, would lead to a skew in the pressure profile towards the outlet region. This, allied with the overall lower absolute film thickness, suggests higher local film pressures, all else being equal. Further comparison of the film thickness maps shows that the horseshoe present in the experimental result does not extend as far towards the bearing inlet. This would be likely lead to increased side leakage and require the film to adopt a more 'convergent shape'.

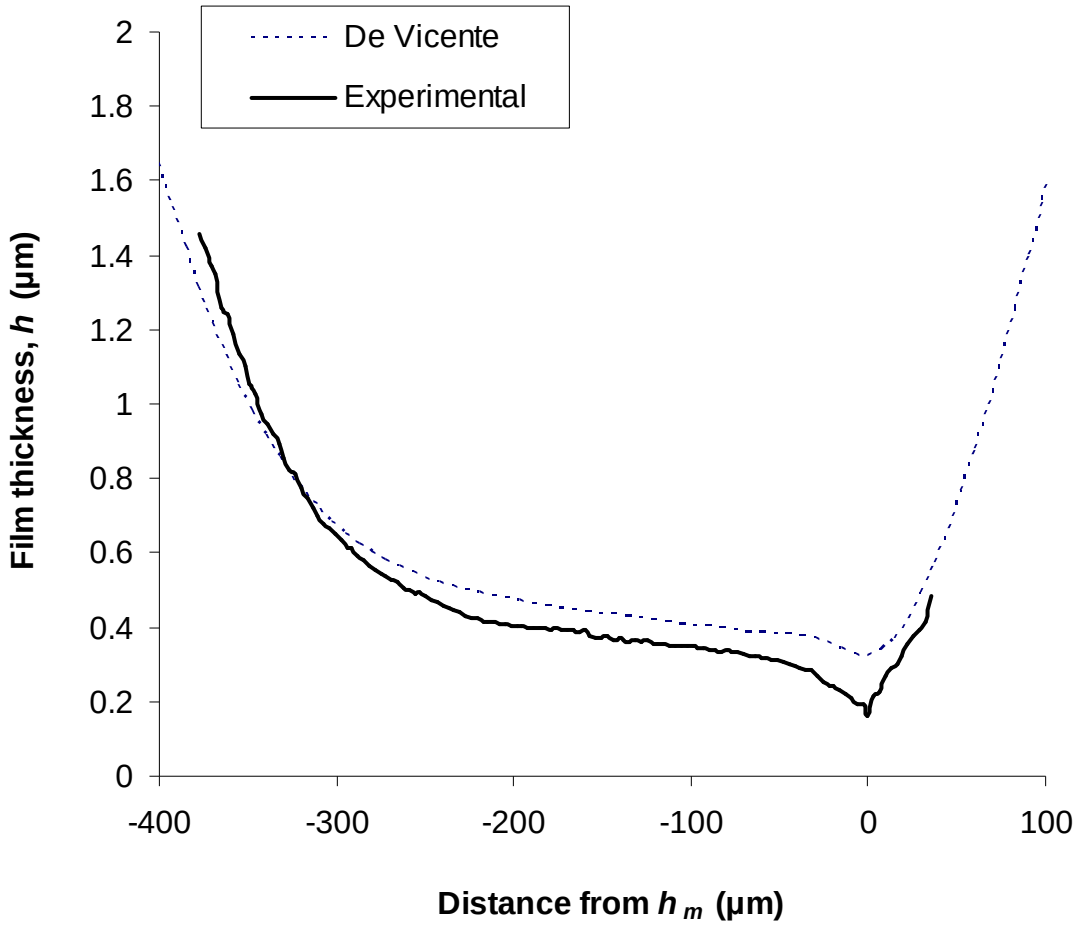

Figure 6.11. Measured film thickness profile (solid) and predicted film thickness profile (dashed) from de Vicente et al. [31], for the tribological contact of interest lubricated with SFO, at W = 3 mN and U = 0.66 mm s^{-1}.

One possible cause for the discrepancy between de Vicente's model and the experimental result is that the model assumes the contact comprises of a glass flat and PDMS ball. However, in this work, the ball is made of a PDMS layer on a steel substrate. The problem of elastic contact between non-conforming coated surfaces has received much attention over the years. It is important in such contacts to correct for the effect of the substrate and for coated surfaces, a new effective elastic modulus and thus contact size can be calculated [101]. The elastic mismatch between the coating and the substrate can be characterised by the Dundurs' parameters [102]. For the tribological contact of interest in the current study, the Dundurs' parameter values lie outside the limits set out by ref. [101]. This is, in

part, due to the large difference between elastic moduli of the contacting surfaces and the large coating thickness compared to the Hertzian contact size. However, Oliveria and Bower were investigating 'hard' coatings in line contacts, unlike the compliant coating in the current study. Meijers [103] and Liu *et al.* [104] give solutions for incompressible materials with Poisson's ratio, ν, up to 0.5, in line and point contacts respectively. Both show that if the coating thickness is large compared to the Hertzian contact radius, for $\nu = 0.5$, the substrate has negligible effect on the contact size.

However, the behaviour of the contacting surfaces will also depend on the nature of the attachment of the PDMS coating to the steel substrate [105]. There are various possibilities: the layer may maintain contact with the substrate at all points, but be free to slip without frictional restraint. This seems unlikely due to the low load, low pressure and slow entrainment conditions. On the other hand the layer may be bonded on to the substrate and thus slip may occur when the shear traction at the interface exceeds a limiting shear stress; or the layer, initially in complete contact with the substrate, may partially lift from the substrate under load. The latter seems plausible as PDMS is known to sweat un-cured monomer [27]. This would allow for the steel PDMS interface to be lubricated over time, gradually separating the surfaces and breaking the adhesive bond between PDMS and steel.

Due to the low contact pressures and low entrainment speeds it is believed that the interfacial friction between the PDMS and metal substrate would not be great enough to cause the effects discussed above. It has already been mentioned that SFO is not hygroscopic, nor is its viscosity greatly affected by changes in temperature. Therefore, the initial explanation given for the discrepancy between theoretical and experimental film thickness data, for GLY, no longer holds any value. It is likely that due to the poor wettability of PDMS, and the entrainment mechanism used in the experimental setup, that starvation is the main cause for the drop in film thickness. This is investigated experimentally in chapter 8.

6.5 Concluding remarks

It has been shown that monochromatic optical interferometry can be used to measure lubricant film thickness in a compliant contact under low load conditions at low entrainment speeds. Film thickness data from the contact are lower than numerical film thickness predictions. Film thickness values were obtained from nanometer to the micron scale.

Experimental film thickness data, for both GLY and SFO, showed poor agreement with theoretical predictions. For GLY this was, at first, tentatively attributed to a lowering of the viscosity due to thermal effects and the hygroscopic nature of glycerol. However, for SFO, which is not hygroscopic, the required changes in lubricant temperature were not realistic. Therefore, the drop in film thickness was attributed to a reduction in lubricant inlet size. It is the authors' view that starvation is the cause for the drop in film thickness. Starvation is discussed in detail in chapter 8.

New fits for the Hamrock and Dowson lubricant film thickness equations for an I-EHL contact for materials of low elastic modulus [97] were obtained. These showed slight differences in dependence on the dimensionless speed and load parameters from those already available in the literature. It was shown that the experimental film profiles vary markedly with both $\overline{U}$ and $\overline{W}$ and, at higher U, a sharp constriction appears at the outlet and the centre of pressure moves towards the rear of the bearing. The outlet of the bearing is therefore responsible for a larger proportion of the total load support. This is in contrast to film shapes predicted in the literature. Further experimental investigation is required using a solid PDMS ball to establish the whether these discrepancies result from the use of a layered PDMS on steel substrate ball in the current study. This will establish whether or not the unconventional film profiles observed in the current study are a genuine feature of I-EHL contacts.

The ability to create film thickness maps using the optical interferometric technique has also been shown. These maps are relatively easy to acquire and not time-consuming. It is not yet possible, however, to generate maps across the entire contact area; in particular obtaining the correct shape of the side lobes is not yet achievable.

Chapter 7

Laser induced fluorescence: experimental technique for measurement of lubricant film thickness.

This chapter explores the possibility of using a laser induced fluorescence experimental technique to measure lubricant film thickness in compliant contacts. The experimental technique is discussed and then proof of concept is presented.

7.1. Introduction:

As discussed in chapter 5 obtaining lubricant film thickness values within a compliant contact is a challenging problem. To date there has been little work published on film thickness measurements in I-EHL contacts. This is probably because the two main methods used to measure film thickness in "hard", metallic contacts, optical interferometry and electrical capacitance, are difficult to apply to "soft", elastomeric contacts. There have, however, been a number of theoretical studies of I-EHL and equations for film thickness in I-EHL contacts have been developed [31,97] although these have not yet been experimentally verified. Chapters 5 and 6 presented an experimental procedure for measuring lubricant films in compliant contacts using a 'two-beam' optical interferometric method. This system is, however, limited to thin films ($h < ca$ 2 μm), due to the loss of coherence in illuminating light with increasing film thickness. Many practical engineering and biological applications operate outside the experimental conditions presented in chapters 5 and 6. Therefore a technique is required to measure thicker films ($h >$ 2 μm). A laser induced fluorescence technique for measuring such films is presented here.

7.2. Laser Induced Fluorescence

Laser induced fluorescence (LIF), is a technique based on the photo-excitation of a fluorophore or fluorescent dye. It has become a commonly used visualization technique for numerous 1D, 2D and 3D applications [106]. However, it has seen limited use as a quantitative tool [75]. The reason for this stems primarily from the difficulty in separating variations in excitation illumination, surface reflectivity and optical distortion effects from fluorescent emission.

In order to understand the principles of this technique and the advantages it presents, it is necessary to understand the fundamental characteristics of dye photo-fluorescence and how it can be used to determine a scalar of interest [106]. As stated by Haugland [107], fluorescence is the result of a three-stage process that occurs in certain molecules (generally polyaromatic hydrocarbons or heterocyclics) called *fluorophores* or fluorescent dyes. These three stages (Fig. 7.1) are explained by Haugland [107] as:

A. Excitation: A photon of energy hv_{EX} is supplied by an external source such as an incandescent lamp or a laser and is absorbed by the fluorophore, creating an excited electronic singlet state (S'_1).

B. Excited-State Lifetime: The excited state exists for a finite time (typically 1 ns to 10 ns). During this time, the fluorophore undergoes conformational changes and is subject to a multitude of possible interactions with its molecular environment. These processes have two important consequences. First, the energy of S'_1 is partially dissipated, yielding a relaxed singlet excited state (S_1) from which fluorescent emission originates. Second, not all the molecules initially excited by absorption (Stage 1) return to the ground state (S_0) by fluorescent emission. Other processes such as coalitional quenching, fluorescence energy transfer and intersystem crossing may also depopulate S_1. The fluorescence quantum yield, which is the ratio of the number of fluorescence photons emitted (Stage 3) to the number of photons absorbed (Stage 1), is a measure of the relative extent to which these processes occur.

C. Fluorescence Emission: A photon of energy hv_{EM} is emitted, returning the fluorophore to its ground state S_0. Due to energy dissipation during the excited-state lifetime, the energy of this photon is lower, and therefore of longer wavelength, than the excitation photon hv_{EX}. The difference in energy or wavelength represented by ($hv_{EX} - hv_{EM}$) is called the Stokes shift. The Stokes shift is fundamental to the sensitivity of fluorescence techniques because it

allows emission photons to be detected against a low background, isolated from excitation photons.

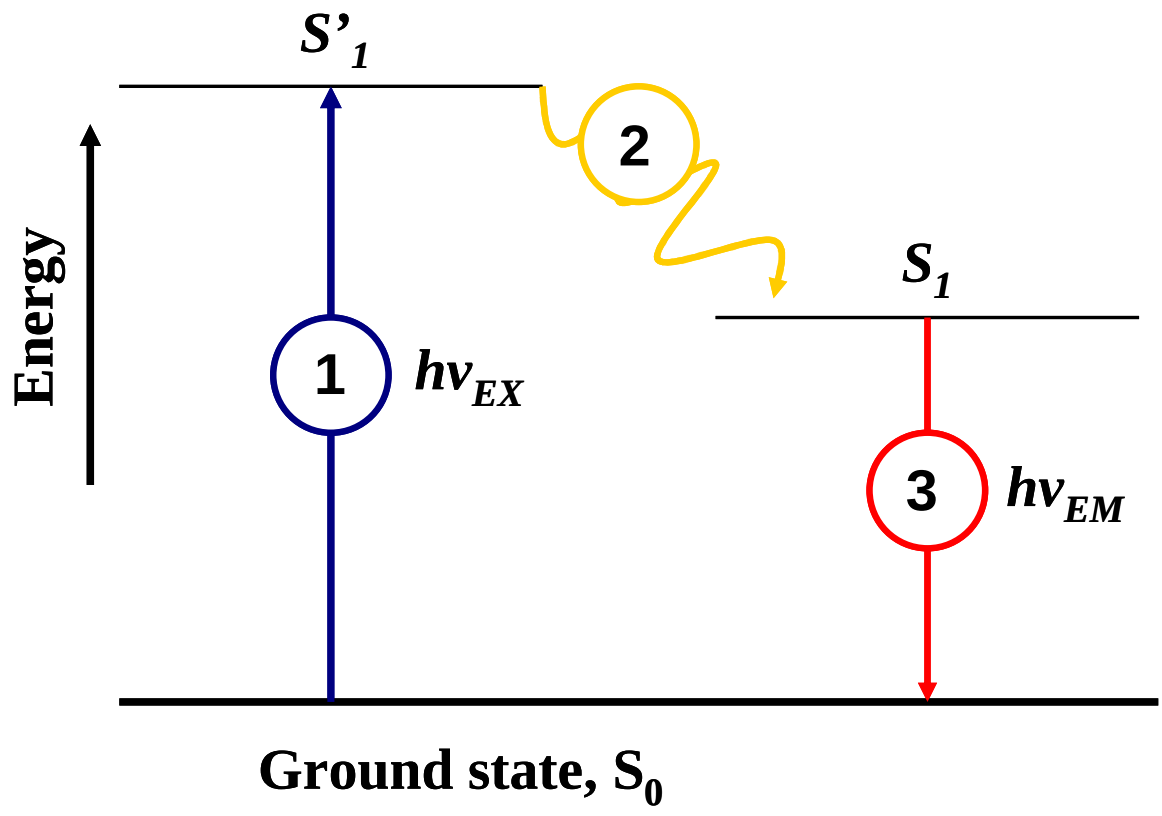

Figure 7.1. Fluorescence principle

Hidrovo *et al.* [76], state that photofluorescence can be used to characterize any scalar that affects the fluorescence of the dye. Fluorescence is a function of the dye characteristics, the dye concentration, the exciting light intensity, and the scalar being measured. Once a particular dye and concentration are selected, the fluorescence dependence on these factors is constant. However, problems lie in the irregularity of illumination light intensity. Most illumination sources are far from uniform. They vary in intensity in space and time. Pulsed lasers are particularly prone to exhibit this behaviour due to the characteristics of their resonance cavities [106]. However the use of pulsed lasers is desirable because their short pulse duration (and consequently short fluorescent emission), allow for nearly instantaneous measurements of the desired scalar. Long periods of illumination may cause undesirable effects such as bleaching.

7.3. Apparatus

The setup used in this study employs an adapted EHL optical interferometry rig (PCS-Instruments, UK). As shown in Fig. 7.2, the tribological contact consists of a stationary elastomer hemisphere pressed against a transparent optical window. The optical window is a large, plain BK7 glass disc (PCS instruments, UK), which is naturally hydrophilic and was used as supplied. No reflective coatings were used on either surface of the glass disc. The glass disc has a Young's modulus of 65 GPa, Poisson's ratio of 0.24 and refractive index of 1.517.

Excitation of the fluorescent dye and illumination of the contact was provided by a solid-state, diode-pumped pulsed laser, which produced green, 532 nm, light. A low power laser (Laser2000 Ltd, Northants, UK) with a maximum power output of 40 mW at 3 kHz was used.

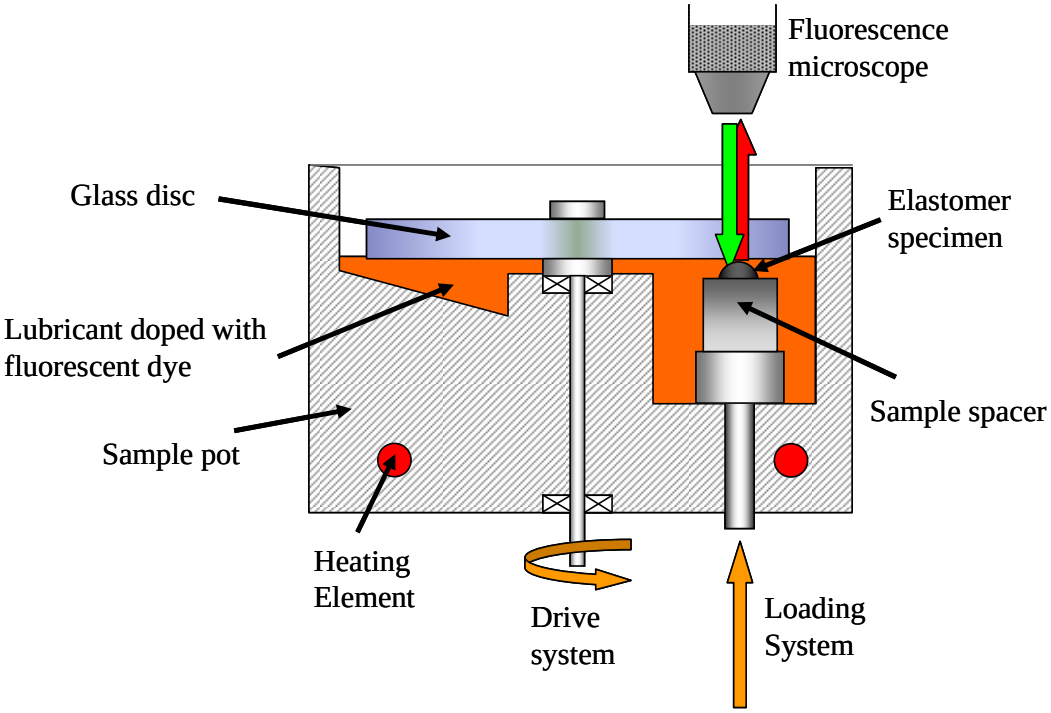

Figure 7.2 Tribological contact and sample pot.

7.3.1. Drive and load system

The standard EHL optical interferometry rig employs a steel ball supported on a bearing carriage, to allow free rotation of the ball. For the current study, the ball and carriage are replaced by a hemispherical elastomer specimen, elevated to a similar height as the ball by a spacer. The elastomer specimen is glued to the spacer, allowing tests to operate in pure sliding conditions. Lubricant is entrained into the contact by rotation of the glass disc and to ensure this, the bottom surface of the disc is immersed in lubricant.

The drive system used was the standard one supplied with the PCS Instrument rig. The glass disk is driven by a DC electrical motor and an optional 25:1 reduction gear box can be attached in series with the disk drive motor. This allows for an accurate control of entrainment speed for speeds less than 2 mm s^{-1}. With this setup, an entrainment speed range of 3 m s^{-1} to 0.1 mm s^{-1} can be achieved.

The entrainment speed, U, is defined as the mean speed of the two surfaces, which, since one surface is stationary, is half the disk speed;

$$U = \frac{u_b + u_d}{2} = \frac{u_d}{2} \tag{7.1}$$

where u_d is the disk speed and u_b is the speed of the ball or, in this case, hemispherical specimen, which, in this case, is $u_b \equiv 0$.

The test sample is mounted on a platform within the sample pot and loaded against the glass disc from below. The existing displacement load system designed for hard/metallic contacts is employed but at low loads (W < 1 N) the system is not sufficiently sensitive or responsive to correct fluctuations in load created by mechanical vibrations. The real applied load for each test was therefore determined

by fitting JKR theory to the load-dependent contact area obtained from captured images of a static contact. This load was then used for film thickness calibration and the subsequent operating load, when a lubricant film is present, was taken to be the static load minus the adhesive force.

7.3.2. Test specimens

It has been reported that the reflectivity of the surfaces under illumination has an effect on the total fluorescent radiation detected by the imaging system [75,77]. Light, from either unabsorbed excitation or emitted light that is transmitted through the fluid and reflected back off the test specimen may cause errors in film thickness measurements. Both Hidrovo *et al.* [77] and Sugimura *et at* [75] comment on the difficulties introduced by reflection. If the contacting surfaces have irregular reflectivity, an error in the total intensity output, and therefore film thickness, may be created.

The elastomer samples were moulded in a plano-concave lens (Edmund Optics, UK), radius of 12.7 mm, and were made from PDMS (Sylgard 184, Dow Corning, UK). Although the PDMS has a low reflectivity, typically $R < 0.05$ %, it is highly transparent. Light transmitted through the PDMS might confuse intensity readings due to irregular reflectivity from within the specimens or from the sample mounting. Filler can be added to the PDMS to reduce background scattering and absorb laser light.

A Wyko optical interferometer (Veeco, UK) was used to study the topography of the reflection interfaces (PDMS, glue, metal mounting) by focusing down through a mounted, clear, PDMS sample. The PDMS surface was found to have roughness, Ra = 9.54 nm, the glue 200 ± 50 nm and metal sample mount 1.8 ± 0.15 μm.

The filler used to absorb transmitted light, was carbon black (CB) (Fluffy, Cabot, UK), which was added to the PDMS at 0.5 wt. %. The addition of CB has little effect on the PDMS surface roughness, increasing slightly to 10.24 nm. The addition of CB to PDMS has negligible effect on the refractive index and therefore reflectivity of the material. The elastic modulus of the resulting elastomer was E = 3.8 MPa, obtained using dynamic mechanical analysis (DMA, Triton, UK). The elastomer was naturally hydrophobic and was used in this state.

Figure 7.3 shows the intensity profile, through the midline of the contact, for CB filled and plain PDMS. The greater intensity of the plain PDMS sample (black line) is a result of the increased reflection of illuminating light. The apparent rise in surface roughness of the plain PDMS is not due to differences in R_a, between the CB and plain PDMS, but created by the irregular reflectivity of the sample mount. This is most evident within the Hertzian contact area.

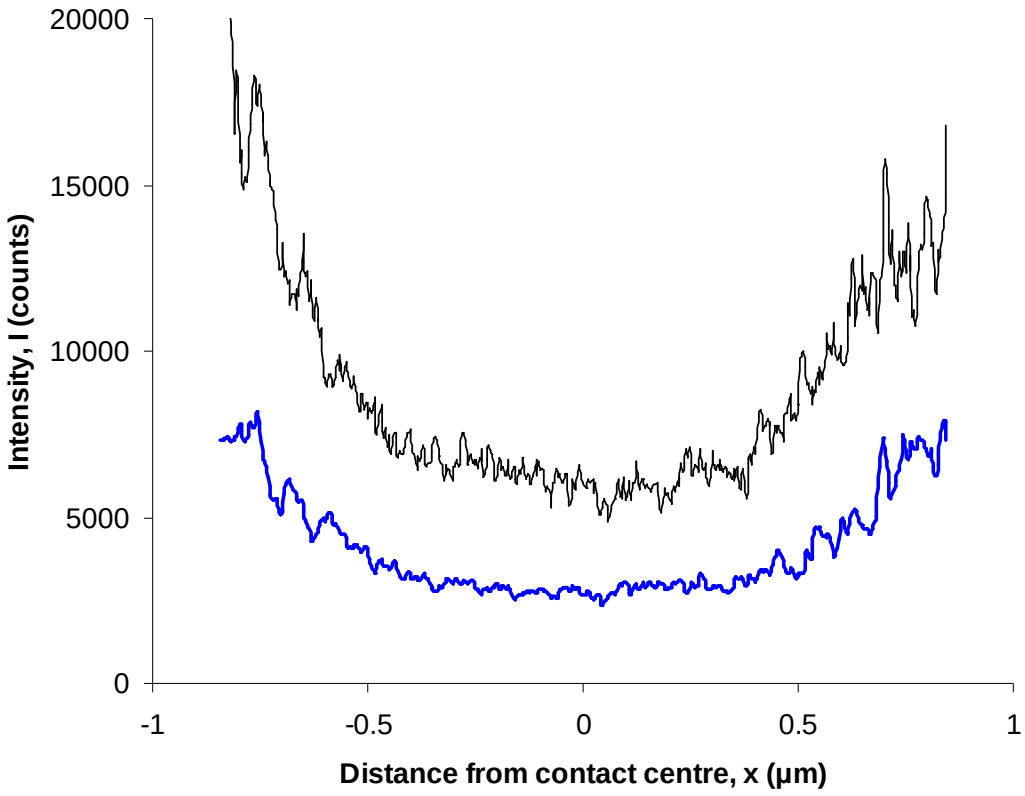

Figure 7.3 Central intensity profile across a static contact for CB filled (blue) and plain (black) PDMS.

7.3.3. Optical equipment

The fluorescence intensity images were observed with an Axiotech Vario microscope (Zeiss, Germany), adjustable along the vertical axis. The mechanical rig was placed on X and Y platforms, allowing image capture of the tribological contact to take place along both axes. A magnification of 3X was found to be convenient for observing both the Hertzian region and inlet/outlet lubrication across the range of loads tested. No eyepiece was needed for the experimental setup as a live image display is provided on the camera's operating PC. Excitation was provided using a solid-state, diode-pumped pulsed laser which generates a wavelength 532 nm (Laser2000 Ltd, UK).

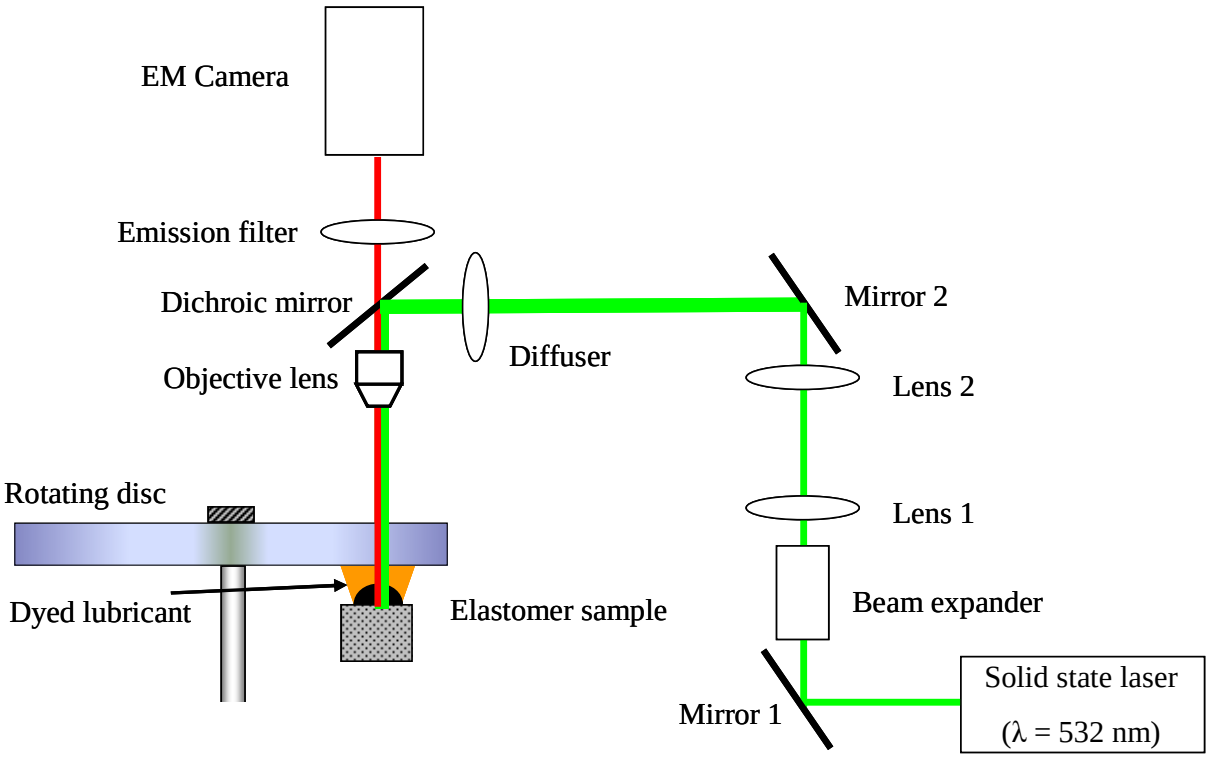

Figure 7.4. Schematic of optical set up and tribological contact

The fluorescent light emitted from the contact is of a longer wavelength than the excitation wavelength of the laser. This allows for the separation of the two light beams by a dichroic mirror, 532 nm (Chroma, USA), located between the objective and camera as shown in Fig. 7.4. An emission filter (Chroma, USA) located above the dichroic mirror is used to filter any light which is not produced by the excited fluorescent dye. The optical setup was selected so that fluorescent dyes that emit within the range of 580 - 640 nm will be observed by the camera. A diffuser is placed before the dichroic mirror to reduce irregularity in the illuminating light. The laser beam intensity distributions of both light sources used in the current study are Gaussian. To flatten the intensity distribution the beam was expanded *ca* 30X using lenses 1, 2 and the beam expander. The titling mirrors 1 and 2 were employed for laser beam alignment. These components were mounted on a common rail and were fully adjustable in the *xyz* axis. The light source was mounted on its own Z stage at the end of the optical setup.

Images were captured *via* the same Rolera MGi B/W EMCCD camera (QImaging, UK) discussed in chapter 5. Images were captured at a series of entrainment speeds, beginning at a low value and increasing in stages. A computer-processing technique was then used to analyse captured images, pixel by pixel, and create film thickness maps based on grey scale intensity. Images were captured as 16 bit tif files, in a 512x512 array. The camera was able to accept an external trigger. The triggering circuit supplied a 5 V TTL signal to the camera using an optical sensor, mounted next to the disk drive shaft, as the triggering switch.

7.3.4. Dye selection

Several factors were considered in selecting an appropriate dye, including:

- Commercial availability.
- Solubility of the dye in the test lubricants.

- Excitation peaks coinciding with the wavelength of the laser (532 nm).
- Compatibility between emission wavelengths and the emission filter wavelength range.
- Quantum yield must be sufficiently high to result in clearly-defined images of the contact.

For thin films or low concentrations, the relationship between the film thickness and emission intensity is linear [7]. It is, therefore, desirable to minimize the dye concentration so that even the thickest films will fall within the linear range of output. However, the concentration/emission intensity must be high enough to over come any background noise from the EMCCD [108]. This is why it is important to select a high quality EMCCD with low background noise.

For this work, the dye Eosin Y (Ana Spec Inc) was chosen since (i) its polar nature allows it to dissolve into aqueous solutions, (ii) its absorption peak coincides with the wavelength of the laser excitation (532 nm) and (iii) its quantum yield is sufficiently high to result in bright, clearly-defined images of the contact. The absorption and emission spectra of Eosin Y were measured using a Luminescence Spectrometer (Perkin Elmer, model LS 50 B). This was kindly carried out by Dr Marinov (Unilever Ltd.). The spectra are shown in Fig. 7.5 alongside the characteristics of the dichroic beam splitter used to separate excitation and emitted light.

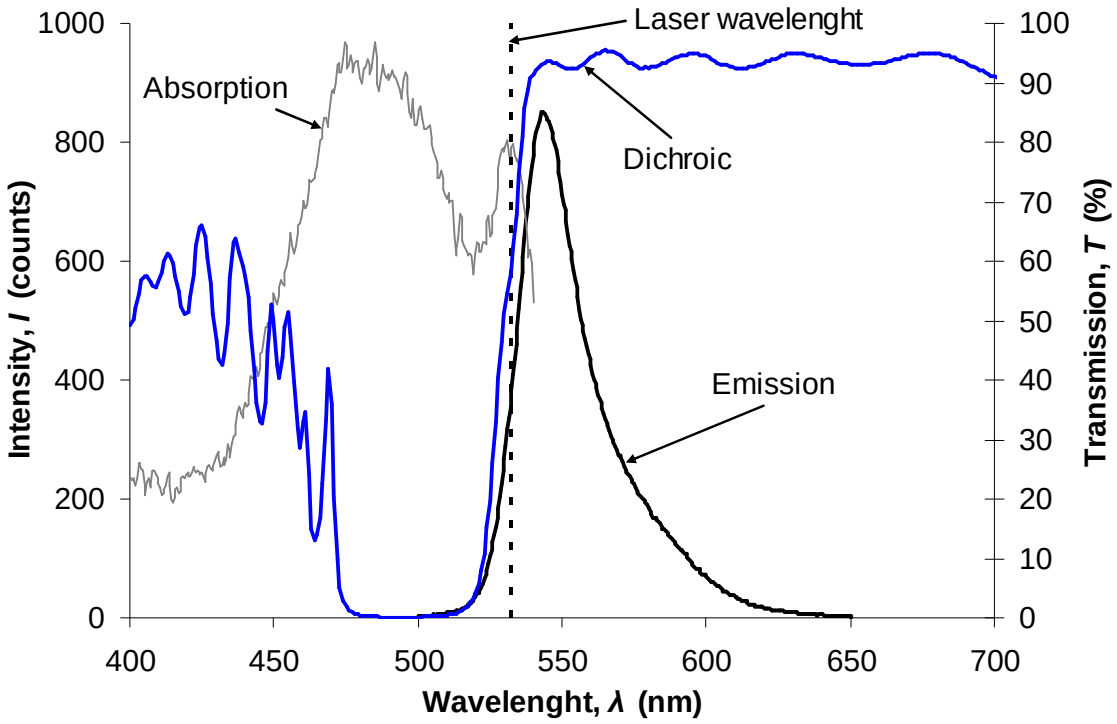

Figure 7.5. Absorption and emission spectra for Eosin Y plotted alongside laser wavelength and Dichroic mirror transmission characteristics.

A small amount of fluorescent dye was found to attach to both PDMS and glass; however the outputted intensity from this was very small compared to the fluorescent intensity created by the high concentration of dye used in the test solutions. Therefore, any build up of dye attached to the surfaces during testing was insignificant and had negligible effect on film thickness measurements.

7.3.5 Test lubricants

Glycerol and water were used as the fluid components for the majority of testing, since their polar nature allows them to dissolve a range of commercially-available fluorescent dyes. Three lubricants were used; pure glycerol (GLY), 50% wt. glycerol solution (GLY50) in distilled water and distilled water. The dynamic viscosities, η, of these lubricants were 1.1, 0.0055, 0.00089 Pas, respectively.

Lubricant viscosities were measured prior to testing using a Stabinger Viscometer (Anton Paar, UK). The viscosity for distilled water, at test temperature (T = 22 ± 2 °C), was obtained from Douglas *et al.* [86].

7.4. Normalization

There are two basic types of noise present in the LIF system employed. The first is created by random fluctuations in the laser light and background noise present within the imaging system. This noise is present at low film thickness/intensities and cannot be eliminated through normalization of the captured fluorescent images. The second is caused by constant irregularities within the illuminating light. This will include speckle, which is caused by filters, lenses or dust and damage on any of the lens/filter surfaces. This noise increases with film thickness. Added to this second noise, the laser used in the current study has a Gaussian intensity distribution which will skew the emission intensity, and thus film thickness measurements, around the Gaussian curve. To reduce these effects, all images were normalized against a background, non-contact image, captured prior to testing. Figure 7.6.a) shows an intensity image from a typical, loaded tribological contact of interest, under static conditions prior to normalization. Some of the intensity variation observed is a result of the varying laser intensity distribution rather than variations in dye quantity. Figure 7.6.b) shows the intensity distribution from a non-contact image. Figure 7.6.c) shows the resultant contact image after normalization of the image in Fig. 7.6.a) using Fig. 7.6.b). It can be seen that the noise is greatly reduced by this normalization.

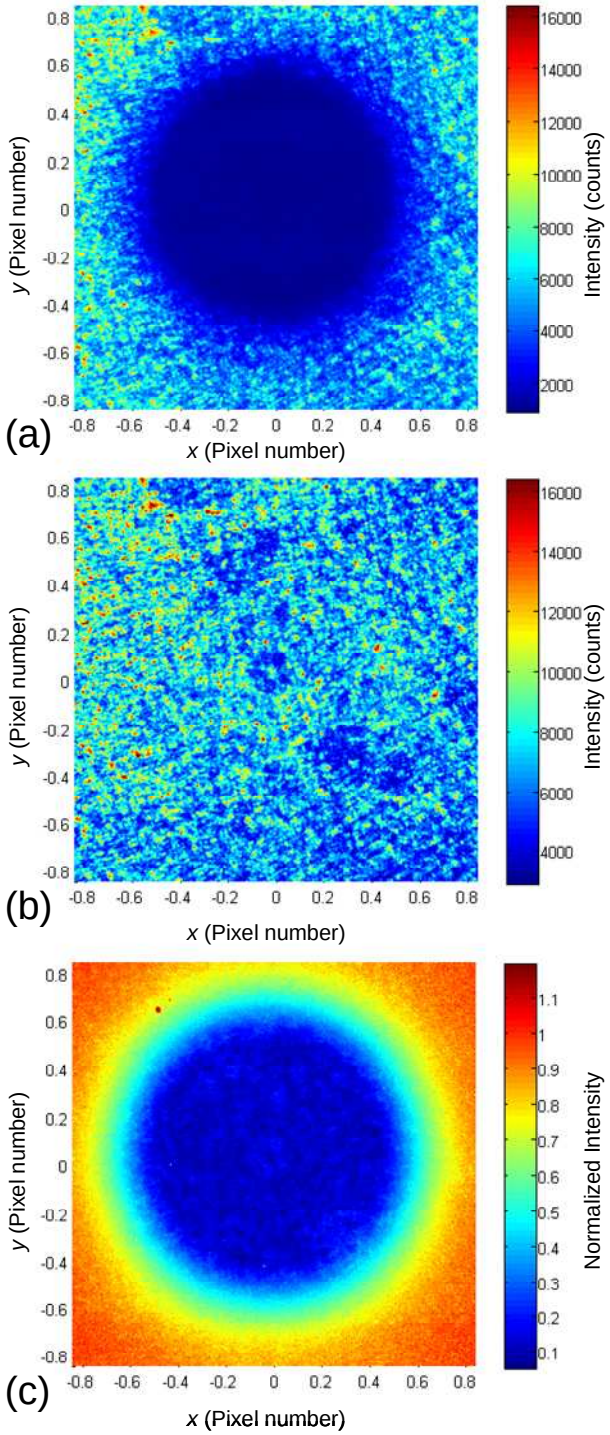

Figure 7.6. Intensity images used for normalization process; (a) typical tribological contact of interest prior to normalization: (b) non-contact image: (c) image 'a' after normalization.

Normalization of all images is done by a two step process. First the minimum intensity value, I_0, in each image, is found and subtracted from each pixel, allowing the minimum intensity to be set to zero. It is necessary to subtract I_0 due to an intensity offset programmed within the camera by the manufacturer, to ensure that no negative values can ever be achieved. The offset value and intensity scale, which is arbitrary, is unique to each camera. If the zero intensity value is not set, noise will be induced within the contact zone. It should also be noted that it is therefore important that intensity values between camera types are not directly compared. Instead, intensity values should be calibrated to a common scalar, such as film thickness, for comparison. Second; the image of interest is then divided by the non-contact image to produce the normalized image, Fig. 7.6.c).

To further reduce the effect of background noise present in the imaging system and of fluctuations in illuminating light, smoothing of intensity values was also carried out. This was done by smoothing three successive times using a simple weighted average in which the intensity at each pixel, $P_{(i,j)}$, was determined by the following equation:

$$P_{(i,j)} = (8P_{(i,j)} + P_{(I+1,j)} + P_{(I-1,j)} + P_{(i,j+1)} + P_{(i,j-1)} + P_{(i-1,j-1)} + P_{(i+1,j-1)} + P_{(i-1,j+1)} + P_{(I+1,j+1)})/16; \quad (7.2)$$

where the last 8 terms are the intensity values of the immediate neighbours.

Figure 7.7 shows intensity plots taken from Fig. 7.6a), b) and c) taken through $y = 0$ (*i.e.* along the mid-line through the stationary contact). The non-contact image profile shows the intensity irregularities across the image. It can be seen that the contact profile was clearly improved by the normalization process. In particular, outside the contact area the profile more closely resembles a Hertzian ball-on-flat out-of-contact shape.

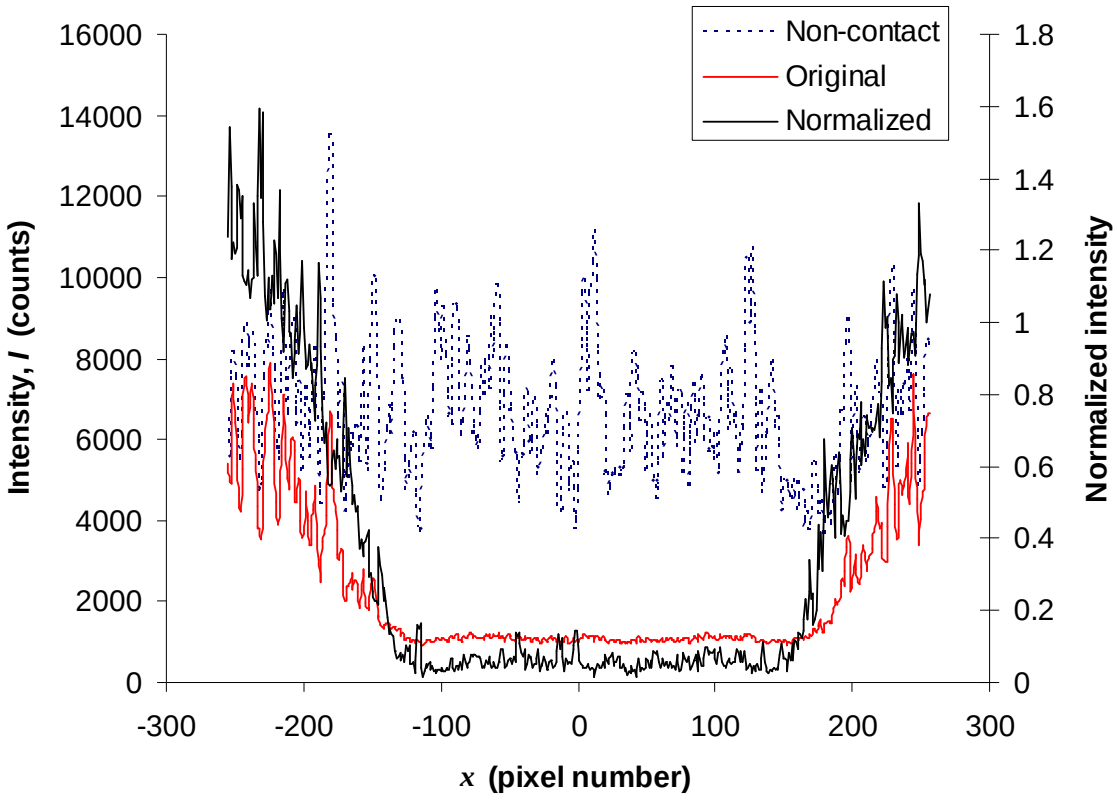

Figure 7.7. Intensity plots of non-contact, contact and normalized contact image, taken through y = 0.

7.5. Calibration

In previous fluorescence work, calibration has been achieved by plotting a known film thickness *versus* fluorescent intensity. This has been done in a number of ways. Sugimura *et al.* [75] employed film thickness values measured using optical interferometry and compared them to intensity curves. For compliant contacts, where extensive film thickness investigations have yet to be carried out, no comparable calibration is possible. Hidrovo *et al.* [106] and Poll *et al.* [7] used an assumed geometry of a calibration wedge or cylinder, respectively. However, Hidrovo has remarked on the effect of reflectivity on emission intensity, and pointed

out that any difference between the calibration piece and the test specimen will introduce an error when converting intensity to film thickness.

In the current study, film thickness calibration was achieved based on intensity images of the contact in static steady state (U = 0) conditions. At the start of each test, the PDMS hemisphere was loaded against the glass disc and intensity profiles taken through the centre of the contact. These intensity profiles were then plotted against the Hertzian equation for the gap outside the central contact region [56].

$$h = \frac{a.p_{\max}}{E'}\left[-\left(2-\frac{r^2}{a^2}\right)\cos^{-1}\frac{a}{r}+\left(\frac{r^2}{a^2}-1\right)^{\frac{1}{2}}\right] \tag{7.3}$$

where the maximum pressure is defined as $p_{\max} = \frac{3W_S}{2\pi a^2}$, r is the distance from the centre of the contact, a the contact radius and W_S is the total load present in the static contact.

There are two potential problems in applying this approach to low load, soft contacts. One is that there will be a significant contribution to the load from adhesive surface forces in the low load, static contact, i.e. $W_s = W_{appl} + W_{adh}$. This needs to be taken into account in solving Eq. (7.3). However it will not be present when the surfaces are separated by a lubricant film. The second is that the effect of adhesion in the static contact may change the separation profile outside the contact so that Eq. (7.3) is no longer applicable. A third complication in the current study was that the actual value of applied load, W_{appl} was not directly controlled due to inadequacies in the loading system.

To determine W_s and W_{appl} the following procedures were adopted. The contact radius was determined from the static intensity image. Using JKR theory for a ball on flat, this is related to the applied load and the surface energy by:

$$a = \left(\frac{3R}{4E'} \left(W_{appl} + 3\pi R\Delta\gamma + \left(6\pi\Delta\gamma R W_{appl} + (3\pi R\Delta\gamma)^2 \right)^{1/2} \right) \right)^{1/3} \quad (7.4)$$

where $\Delta\gamma$ is the specific energy of adhesion between the two surfaces and R the radius of the ball. The specific energy of adhesion for the PDMS samples on glass was determined by carefully placing a PDMS sample on the top surface of a plain glass disc. The contact was then viewed from the underside of the disc, and the applied load was simply the weight of the PDMS sample. An optical interferometric technique employing polarised white light and quarter wavelength plates, developed by Eguchi *et al.* [109] was used to accurately capture the contact area and measure the contact radius. By applying Eq. (7.4), $\Delta\gamma$ was found such that the calculated JKR contact radius matched the observed image contact radius. $\Delta\gamma$ was found to be 0.0356 J m^{-2}.

This value of $\Delta\gamma$ could then be used in Eq. (7.4) at the start of each test to obtain from the static contact radius the value of applied load, W_{appl} and also the total static load, W_s for use in Eq. (7.3). The latter is simply the sum of the four terms in the second bracket in Eq. (7.4). During the test the contact operates in the I-EHL regime where there should be no surface adhesion forces so the operating load equals W_{appl}.

Figure 7.8.a) compares the intensity profile across the centre of the contact with the gap predicted from Eq. (7.3). Zero film thickness is assumed within the central contact region. For a compliant contact such as the one used in the present study, rapid approach of the surfaces traps a 'bell' of liquid in the centre of the contact and the entrapped lubricant is squeezed out over time under static conditions [67,72]. To achieve an accurate calibration the contact was therefore left for 10 minutes before the intensity image was taken. The intensity *versus* film thickness calibration graph is shown in Fig. 7.8.b). At low film thickness, a difference in thickness of one micron is represented by *ca* 500 intensity counts, which means that theoretically a difference in thickness of 2 nm can be detected. However, this value is likely to be far higher, as indicated by the intensity noise present at low film thickness in Fig.

7.8.a). This noise will create a minimum measurable film thickness, which is later shown to be *ca* 300 nm.

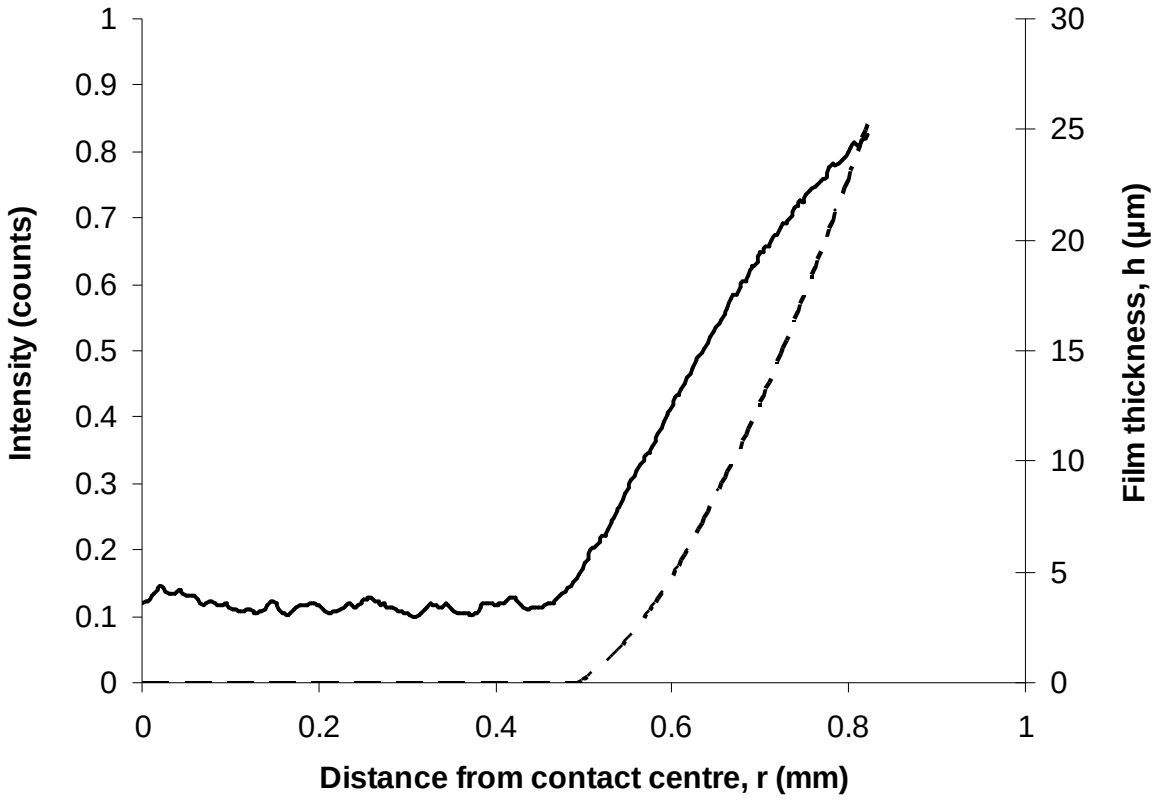

Figure 7.8.a) Line profile of the fluorescence intensity from calibration image for the tribological contact lubricated with pure glycerol, and predicted film thickness profile across the calibration contact from Eq. (7.3), plotted as solid and dashed lines respectively.

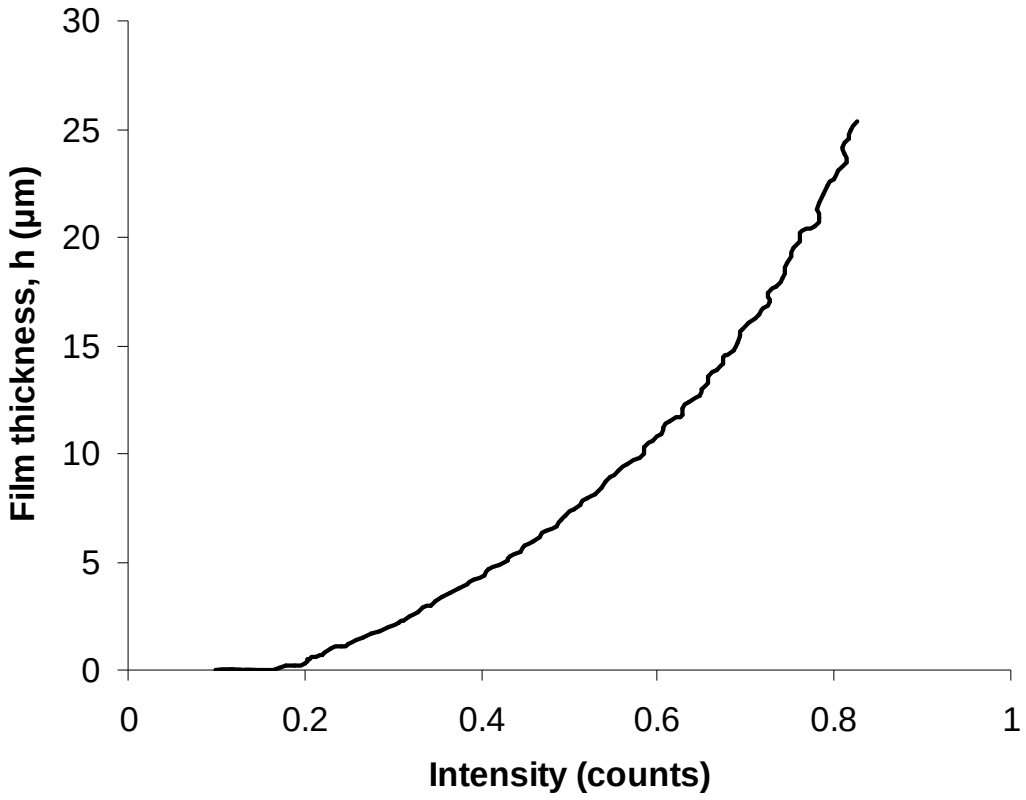

Figure 7.8.b) Intensity versus film thickness calibration curve.

The calibration shown in Fig. 7.8 assumes the theoretical gap outside the central contact regions can be obtained from Hertz theory (Eq. 7.3), *i.e.* there was no significant change resulting from adhesion forces in the static contact. However, as stated above, adhesion between the elastic bodies is occurring. Modelling the resultant contact shape through full numerical analysis is complex and time consuming. Whilst a number of these models exist, such as the work carried out by Greenwood [110], these only give the results the authors choose to pass on. These establish when JKR solution is valid and indicate the ways in which it is incomplete, but stop there. A more valuable solution is presented by Greenwood and Johnson [111], who derived a simple numerical solution. Here the gap profile outside of the contact area for a ball-on-flat, influenced by surface adhesion forces, is based on the combination of two Hertzian pressure distributions. This 'double-Hertz' model relies solely on the well known results from the Hertz analysis and that the shape of the deformed surface and of the gap involves only elementary functions.

This simple model is done by overlapping the initial Hertzian contact zone, of radius *a*, with a larger out-of-contact zone, of radius *c*, over which the adhesive force acts. The gap, *h*, is thus the combination of two external Hertzian shapes:

$$h = \frac{1+k}{\pi R}\left[a\left(r^2 - a^2\right)^{0.5} - \left(2a^2 - r^2\right)\cos^{-1}\left(\frac{a}{r}\right)\right] - \frac{k}{\pi R}\left[c\left(r^2 - c^2\right)^{0.5} - \left(2c^2 - r^2\right)\cos^{-1}\left(\frac{c}{r}\right)\right] \tag{7.5}$$

where *k* is an arbitrary scaling factor and *R* is the radius of the ball.

In contrast to Eq. (7.4), fluorescence intensity profiles can not be compared directly with Eq. (7.5) as both *k* and *c* are unknown, making calibration *via* Eq. (7.5) difficult. Before calibration of film thickness between fluorescent images and Eq. (7.5) can take place *k* and *c* must be determined. This needs to be done every time the applied load, contact materials or contact geometry is changed.

Figure 7.9 shows the measured gap profile for the tribological contact of interest lubricated with GLY, under static conditions for an applied load of 10 mN. The measured profile was obtained using the optical interferometric technique discussed in chapter 5.

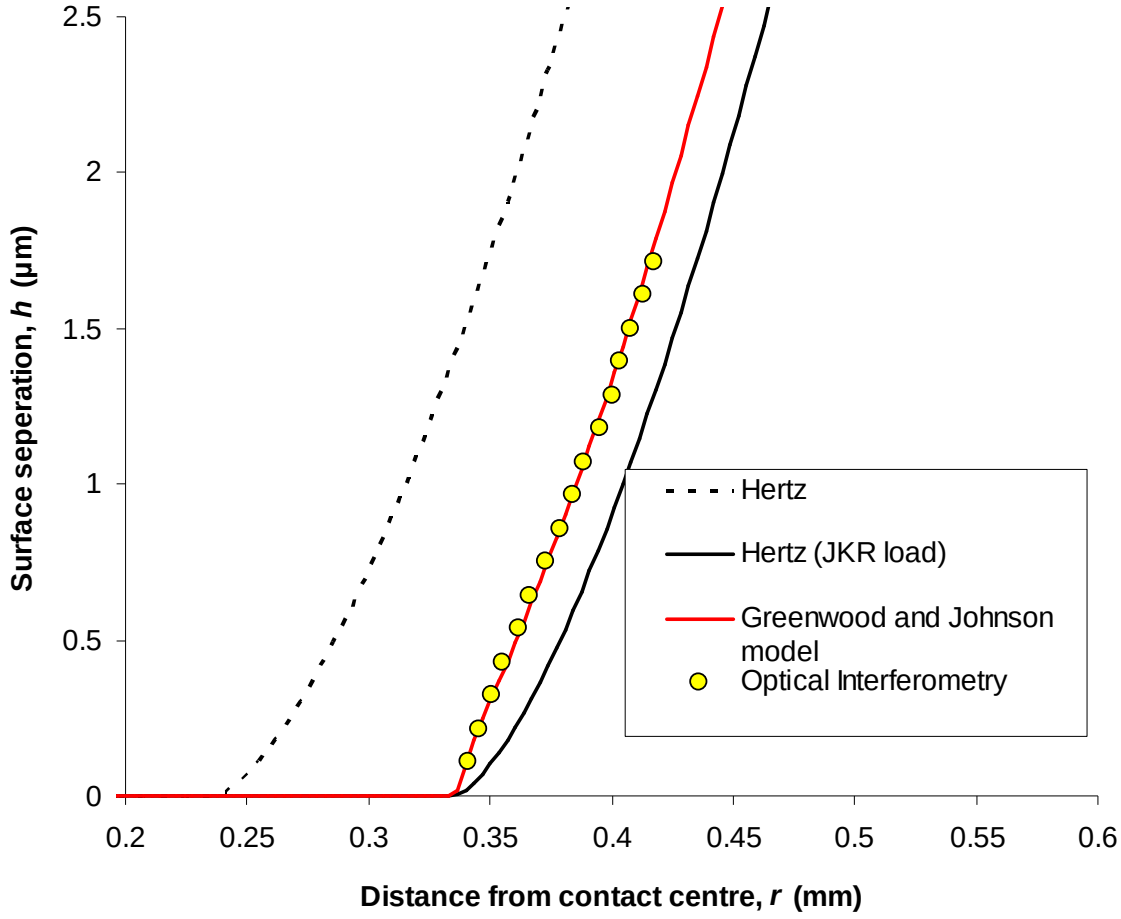

Figure 7.9. Contact profiles obtained using Hertz (dashed line), Hertz with corrected JKR load (solid line), Eq. (7.5), and optical interferometry.

Also shown are the theoretical profiles from Eq. (7.4) calculated using W_{appl}, plotted as a dashed line and W_s plotted as a solid line. The growth in contact size due to adhesive force can be clearly seen by comparing these two plots. It is also observed that the difference between Eq. (7.4), calculated using the overall static load, W_s, and the measured profile is less than *ca* 5 %.

Also given is the Greenwood and Johnson profile from Eq. (7.5) using W_s. Values for k and c were obtained by matching the theoretical to the real measured profile. A good agreement is observed. However, the surface energy calculated from these values of c and k was found to differ from the measured value stated above. Surface energy was calculated using the following equation [111]:

$$\Delta\gamma = k(k+1)\frac{E^*}{R^2}\frac{2}{3\pi}(c-a)^2(c-2a) \tag{7.6}$$

Profiles could not be matched for similar values of surface energy. It is recognised that the Greenwood and Johnson model is a simplification of adhesive contacts and therefore, may not be suitable for this particular contact of interest. Based on these difficulties the Hertz model, with total load modified to include an adhesive contribution, was considered to be adequate for calibration purposes.

7.6 Conclusion

a) For clear visible fluorescence images to be obtained an optical system must be devised which allows for the separation of excitation and emission light. This can be achieved through the employment of dichroic mirrors or beam splitters and filter lenses.

b) Fluorescent dyes must be selected by their solubility in the test lubricants, excitation coinciding with the wavelength of illumination, and their quantum yield must be sufficiently high to result in clearly-defined images of the contact. Dyes need to be prepared so that they exhibit low concentration related phenomenon; *i.e.* bleaching and quenching.

c) Non-absorbed excitation light can cause erroneous emission intensity measurements through irregular background reflection. This effect can be reduced by employing poorly reflective surfaces and good light absorbing materials. The addition of CB particles to PDMS meets this requirement.

d) There are two types of fluorescence intensity noise. The first is background electronic noise within the imaging system, observed at low film thicknesses, low dye concentration and low intensity or high gain levels.

The second is caused by irregular excitation light which is increased with film thickness and dye concentration. Normalization of images against a non-contact image can reduce these noise interferences to required levels.

e) For direct conversion from fluorescence intensity to film thickness values, a calibration system needs to be employed that avoids errors created by change in reflectivity between calibration and test samples. Calibrating, by utilizing the test specimen, against theoretical profiles eliminates this possible error.

Chapter 8

Investigation into fully flooded and starved lubrication conditions using LIF

In this chapter results are reported for a pure sliding contact between PDMS and glass lubricated with glycerol and water solutions over a range of entrainment speeds. Film thickness measurements were made for both fully-flooded and starved conditions using LIF. Contact profile shapes and film thickness maps are compared to theoretical models and discussed.

The work in this chapter can be found in; Myant C, et al. "Laser-induced fluorescence for film thickness mapping in pure sliding lubricated, compliant, contacts". Tribology International (2010), doi:10.1016/j.triboint.2010.03.013

8.1 Test conditions and procedure

The experiments described here were conducted using the LIF technique developed in chapter 7. The tribological contact consists of a CB-PDMS hemisphere loaded against a rotating plain glass disc. Three lubricants were used; pure glycerol (GLY), 50% wt. glycerol solution (GLY50) in distilled water and distilled water, over a large entrainment range of 0 to 1100 mm s^{-1}. All tests were carried out at room temperature (T = 22 ± 2 °C). The applied load was 40 ± 2 mN for all tests.

In addition to its robustness regarding the optical properties of the specimen materials, a further advantage of this technique is the wide range of film thicknesses that can be measured. A range of *ca* 200 nm to 25 μm is demonstrated. At high dye concentration (or thick films) there is a danger of saturation occurring, but theoretically the upper range can be controlled by simply altering the dye concentration.

The test protocol was as follows:

- A new elastomer sample was used for each test and was cleaned by successively rinsing in 2% wt. sodium dodecylsulphonate and distilled water, followed by immersion in isopropanol in an ultrasonic bath for three minutes and then rinsed in distilled water. The elastomer was naturally hydrophobic and used in this state.
- The glass disc was cleaned using lens cleaning solution (Dalloz safety^{TM}), followed by acetone.
- The test rig was then assembled and lubricant added
- Load was then applied and intensity to film thickness (and load) calibration images taken.
- Intensity images were captured at a series of entrainment speeds, beginning from a low value and increasing this in stages.

- A computer-processing technique was then used to analyse captured images, pixel by pixel, and create film thickness maps based on grey scale intensity.

Tests were carried out with two different lubricant supply conditions. In one the whole test pot was filled with lubricant to cover the stationary specimen and also the underside of the glass disc. This provided "fully-flooded" conditions. In the second, a small volume of lubricant was smeared initially on the underside of the glass disc and no further lubricant was added. This provided "starvation" conditions.

8.2 Results

8.2.1 Fully flooded

In the first set of experiments, GLY, GLY50 and water were used as test lubricants in nominally fully-flooded conditions to explore the film thickness measurements capabilities of the LIF technique. In these the hemisphere and the lower side of the glass disc were full-immersed in the lubricant. Figure 8.1 shows central film thickness, $h_{c,}$ results for all three test lubricants. The theoretical central film thicknesses for all three lubricants, calculated using Eq. (2.3), are also plotted as solid black lines. As described in chapter 6, the location of h_c in compliant contacts is not well defined since the contact generally forms a hydrodynamic wedge shape without a central plateau. Therefore the position of h_c, was simply defined as the middle of the detected contact map.

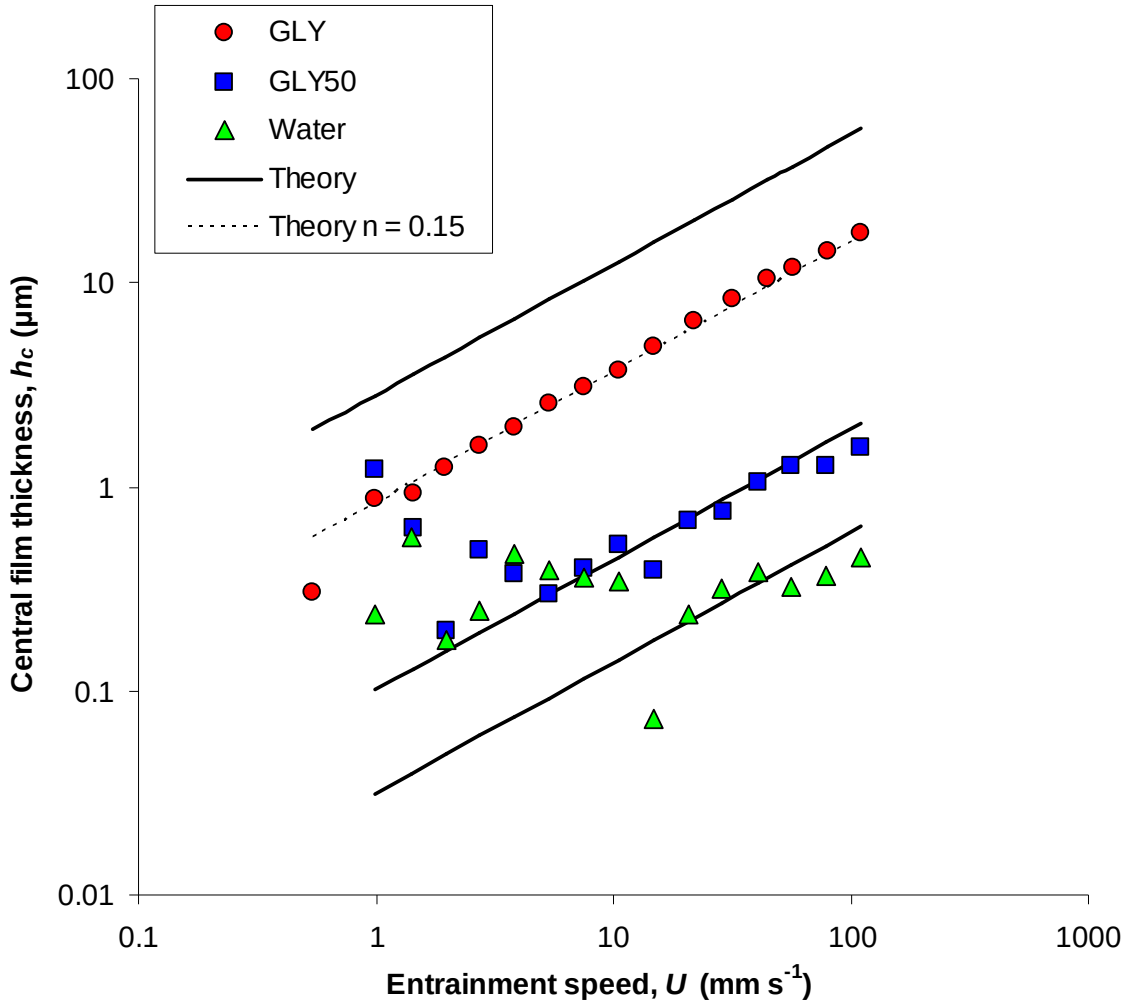

Figure 8.1. Central film thickness for the tribological contact of interest under W = 40 mN, lubricated with GLY, GLY50 and water. Numerical predictions from Eq. (2.3) are shown as solid lines for each lubricant using the measured viscosity. The predicted film thickness for η = 0.15 Pas is shown as a dashed line.

For GLY50 and distilled water, a large amount of scatter is observed at low entrainment speeds and low film thickness. The noise indicates a minimum detectable film thickness of *ca* 300 nm for the current set-up. As entrainment is increased good agreement between theoretical prediction and experimental values is observed.

For GLY it can be seen that the experimental results are considerably lower than the numerical predictions for the measured dynamic viscosity of η = 1.1 Pas. Results

presented in chapter 6 using optical interferometry, as well as work carried out by Bongaerts *et al.* [19] observed a similar disparity between theoretical and experimental values. This discrepancy between experimental and theoretical film thickness values was equated to a large change in lubricant properties caused by (i) the hygroscopic nature of glycerol and (ii) temperature rises within the contact. Good agreement is achieved for a value of η = 0.15 Pas, rather than the measured value.

It seems more likely that a noticeable temperature rise may occur within the contact of interest compared to that of chapter 6, due to the introduction of a laser and considerably higher entrainment speeds. The higher $\overline{U}$ and $\overline{W}$ used in this investigation would give rise to higher shear heating of the lubricant. Using Eq. (6.2) a temperature rise of *ca* 4 °C is calculated. It is also possible, now, to estimate the temperature change due to illumination. The maximum impact of heating caused by the illuminating laser light can be estimated by relating the laser power, P_R, to the change in temperature, ΔT, using the relationship:

$$P_R = \frac{m.c_p \Delta T}{t}. \tag{8.1}$$

where c_p is the specific heat capacity of glycerol, m the mass of lubricant volume affected ($m = \pi a^2 h_a \rho$) and t the time taken for fluid to pass through the contact ($t = \frac{2a}{U}$) where ρ is the density of glycerol, a is the contact radius and h_a the average film thickness. For a density and specific heat of glycerol of 1250 kg/m^3 and 2400 J kg^{-1} K^{-1}, a = 0.42 mm and assuming an average film thickness of 5 μm at U = 10 mms^{-1}, as indicated in Fig. 8.1. The temperature rise at the given laser power of 0.4 mW would be *ca* 4 °C. Whilst Eq. (6.2) also gives $\Delta T \approx 4$ °C for the same values of h and U.

The combined temperatures from Eqs. (6.2) and (8.1) are somewhat closer than those observed in chapter 6 to the required temperature increase needed for the effective change in lubricant viscosity to occur. However, as discussed in chapter 6, the actual

temperature increase is likely to be much lower. Results for SFO, in chapter 6, suggested that lubricant viscosity change is unlikely to be the main cause for the discrepancy between experimental and predicted film thickness values. It was suggested that two possibilities remain; (i) theoretical error and (ii) starvation.

Eq. (2.3) is a best fit obtained from a series of I-EHL numerical solutions obtained by Dowson and Hamrock [97]. In their study a range of values of $\overline{U}$ = 5 x 10^{-9} to 5 x 10^{-8} and $\overline{W}$ = 0.2 to 2 x 10^{-3} were used. In the current experimental measurements the range of values of $\overline{U}$ = 7 x 10^{-12} to 1 x 10^{-6} and $\overline{W}$ = *ca* 2 x 10^{-5} were covered, so $\overline{W}$ is somewhat smaller than the dimensionless load parameters used by Hamrock and Dowson. It is unlikely that the difference in $\overline{W}$ is the main cause for differences between experimental and theoretical values, as film thickness has a low dependence on the dimensionless load parameter (as seen in Eq. 2.3, 2.4).

The numerical predictions made by de Vicente *et al.* [31], discussed in chapter 2 (Eqs. 2.10 and 2.11), were solved over a different range of dimensionless parameters to those used by Dowson and Hamrock. De Vicente *et al* used $\overline{U}$ = 1.5 x 10^{-7} to 4 x 10^{-5} and $\overline{W}$ = 7.5 x 10^{-4} to 2.45 x 10^{-2}. These also predict greater film thickness values than obtained experimentally for the measured viscosity of 1.1 Pas. Good agreement is achieved for a lowered viscosity of 0.22 Pas.

Due to the poor wettability of PDMS it is possible that some level of starvation is occurring. Starvation under elastohydrodynamic conditions has been extensively investigated for 'hard', metallic contacts and is now well understood [112-114]. Wedeven *et al.* [115], compared experimental observations to theoretical predictions, whilst Hamrock and Dowson [116] used numerical contact models to predict the onset of starvation. Both studies showed that the film thickness within the Hertzian contact region is a function of the lubricant supply immediately upstream. Dowson and Hamrock extended their initial numerical analysis to materials of low elastic modulus [117]. Starvation is investigated in the following section.

8.2.2 Starved results

A second set of experiments was carried out investigated to explore the impact of starvation on film thickness. To promote starvation, tests were carried out in which a small amount of lubricant was smeared onto the underside of the glass disc rather than fully-immersed conditions. The maximum entrainment speed was also increased to 1100 mm s^{-1}.

Figure 8.2 shows a series of fluorescence intensity images obtained with increasing entrainment speed for lubrication with glycerol under starved conditions. Entrainment was from right to left along the *x* axis. A 'horseshoe' constriction at the outlet of the contact was formed whenever lubricant was entrained, although it can only be seen in the images for U = 14.6 mm s^{-1} and above, due to the colour scale chosen for these images.

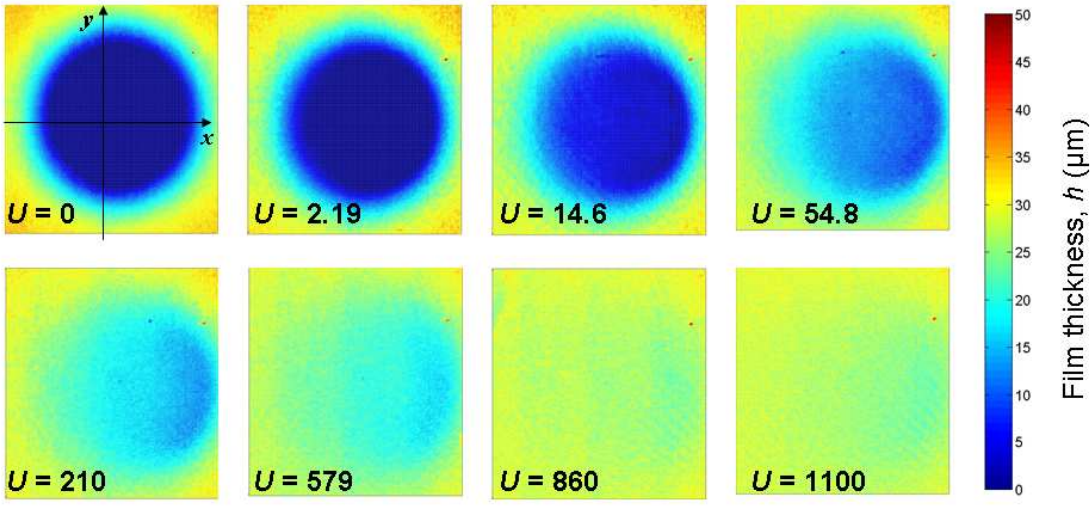

Figure 8.2. Film thickness maps of the tribological contact, lubricated with GLY. Film thickness is expressed as RGB intensity given in the colour bar scale on the right of the figure. Inlet is on the right of each image. Images are ca 1.5x1.5 mm in size.

It should be emphasised that, unlike optical interferometry, LIF does not measure the separation of the surfaces but rather the amount of fluorescent dye between the surfaces. Thus if starvation or cavitations occurs, this will be reflected in a lower intensity than there would be with a full fluid film between the surfaces.

From the calibrated fluorescence images, central and minimum film thickness values were obtained. Central film thickness values were taken at the position $x = 0$ and $y = 0$. The results for pure glycerol are shown in Fig. 8.3 plotted against the entrainment speed, U. Also shown is the theoretical central film thickness (Eq. 2.3) plotted as a solid black line. This is based on the effective viscosity of 0.15 Pas found in the fully flooded tests.

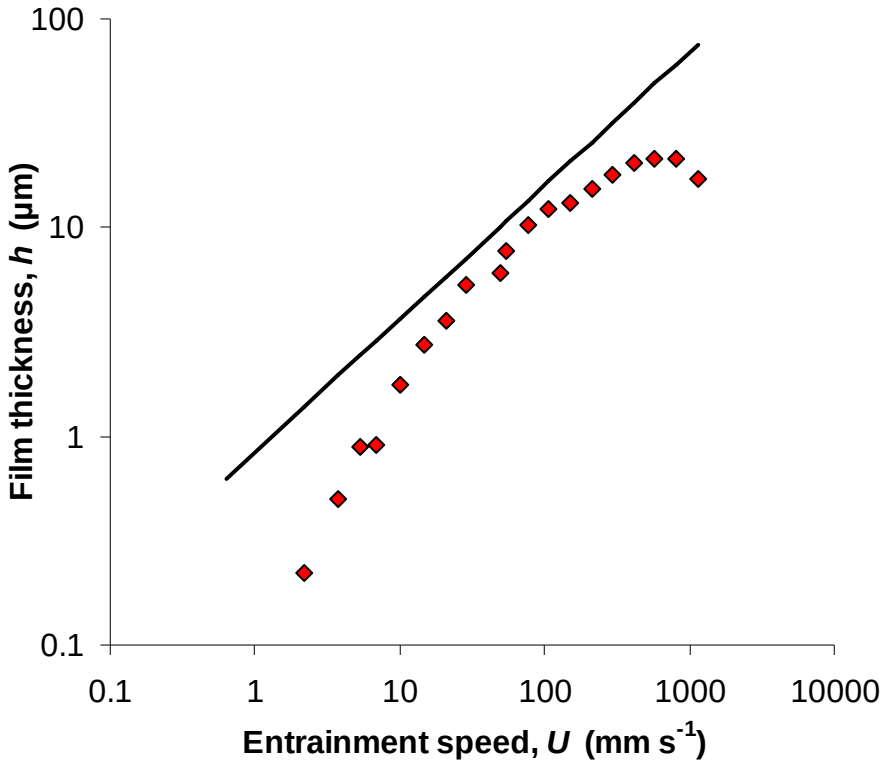

Figure 8.3. Central film thickness for the tribological contact of interest under W = 40 mN, lubricated with GLY. Numerical predictions from Eq. (2.3) are shown as a solid line, using the lowered viscosity (η = 0.15).

It can be seen that film thickness values for h_c are below the theoretical fully-flooded values, even though the latter are based on the effective viscosity of 0.15 Pas which best fitted the fully-flooded measurements. At high speeds, a rapid divergence is recorded. Since this reduction in film thickness occurred when then lubricant supply was limited it is likely to have resulted from starvation.

Figures 8.4.a) and (b) show measured film thickness profiles along the entrainment direction (at $y = 0$) and transverse to the entrainment direction (at $x = 0$) respectively. These were obtained from the images shown in Fig. 8.2. As U increased, profiles along the sliding direction changed from being close to Hertzian to forming an almost linear wedge. At low entrainment speeds an inlet profile can be seen, however, for the two high entrainment speed profiles, the lack of an inlet profile is observed. This, coupled with the deviation in experimental from predicted values observed in Fig. 8.3, might suggest the onset of starved conditions. The constriction near the contact exit can be seen but is partially obscured by noise in the profile. This noise is not believed to indicate a real feature such as surface roughness or debris within the lubricant, but rather is due to noise within the illuminating light [77].

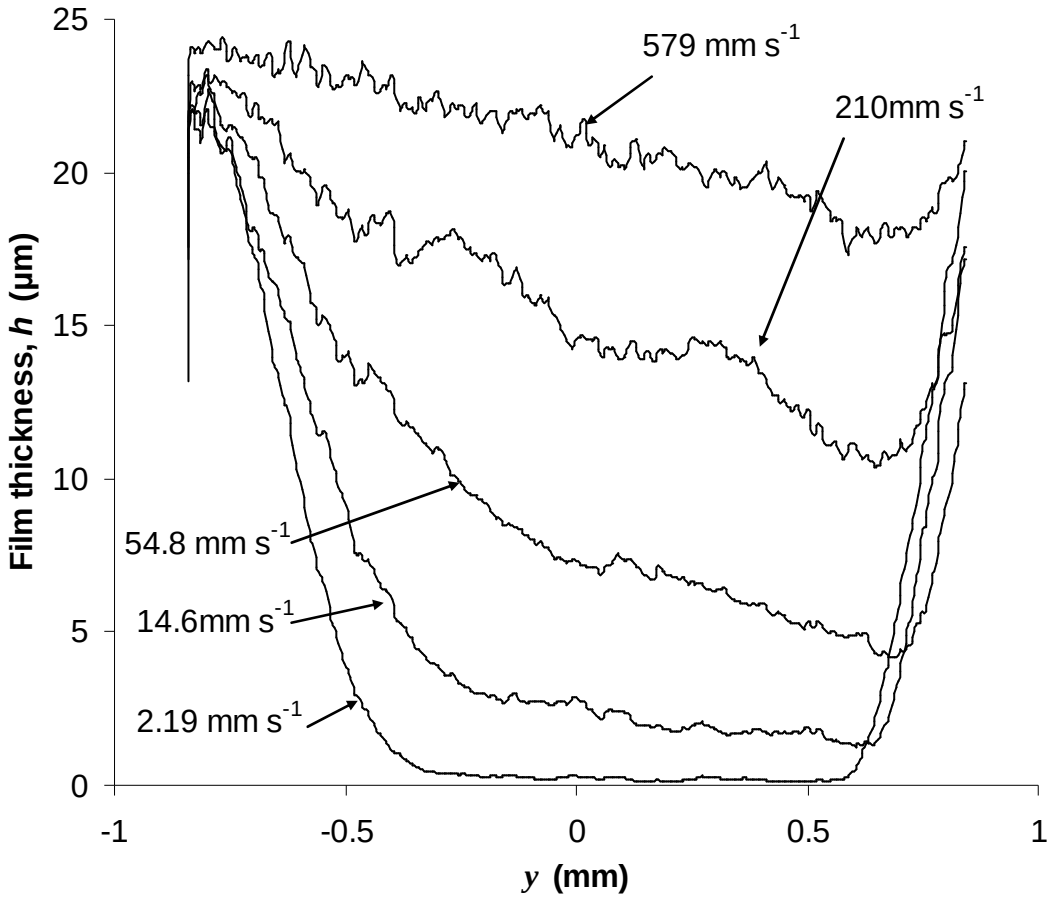

Figure 8.4.a) Film thickness profile plots along the entrainment direction (at y = 0) for selected entrainment speeds. Fluid flows right to left.

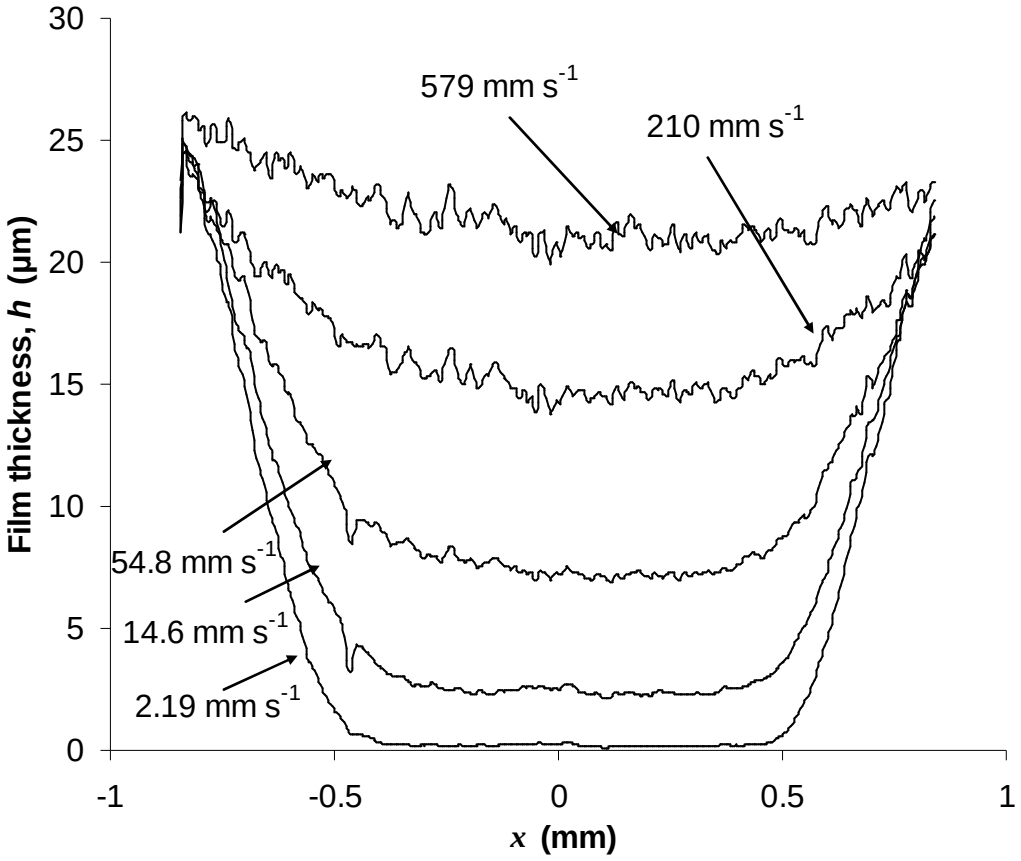

Figure 8.4.b) Film thickness profile plots taken along the plane transverse to the entrainment direction (at x = 0) for selected entrainment speeds

Hamrock and Dowson state that lubricant starvation can be studied simply by reducing the dimensionless inlet distance, *m*, where $m = x_b/a$, and *a* is the Hertzian contact radius and x_b is the inlet boundary distance measured from the centre of the Hertzian contact to the edge of the inlet boundary immediately upstream. To evaluate the reduction in inlet size required for agreement between experimental and theoretical film thickness profiles, numerical solutions for compliant EHL developed by de Vicente *et al.* [31] are compared to profiles from Fig. 8.4.a), at U = 14.6, 54.8 and 210 mm s^{-1}, in Fig. 8.5a) to c) respectively. The theoretical profiles under fully flooded conditions (using η = 0.15 Pas) are shown and also solutions for reduced inlet size. The minimum film thickness position was used as a universal reference point to compare the plots. For the starved solution cases (Figs. 8.5.b and c) the inlet boundary positions are indicated.

In the work of de Vicente *et al.* the fully flooded inlet distance was taken to be m = 5, when deriving Eqs. (2.10) and (2.11). However, the experimental results at high speeds can only be made to match predictions if the inlet distance is reduced, with the inlet approaching very close to the contact radius. Under these conditions it is also clear that there is far less fluid present upstream of this starved inlet than would be required to fill the gap between the surfaces. By contrast, at low speeds, only a mild reduction in the inlet length of m = 2 is required to fit the results and, indeed, the fluorescence results show that the inlet remains flooded to the maximum measureable distance of 2a in front of the Hertz inlet.

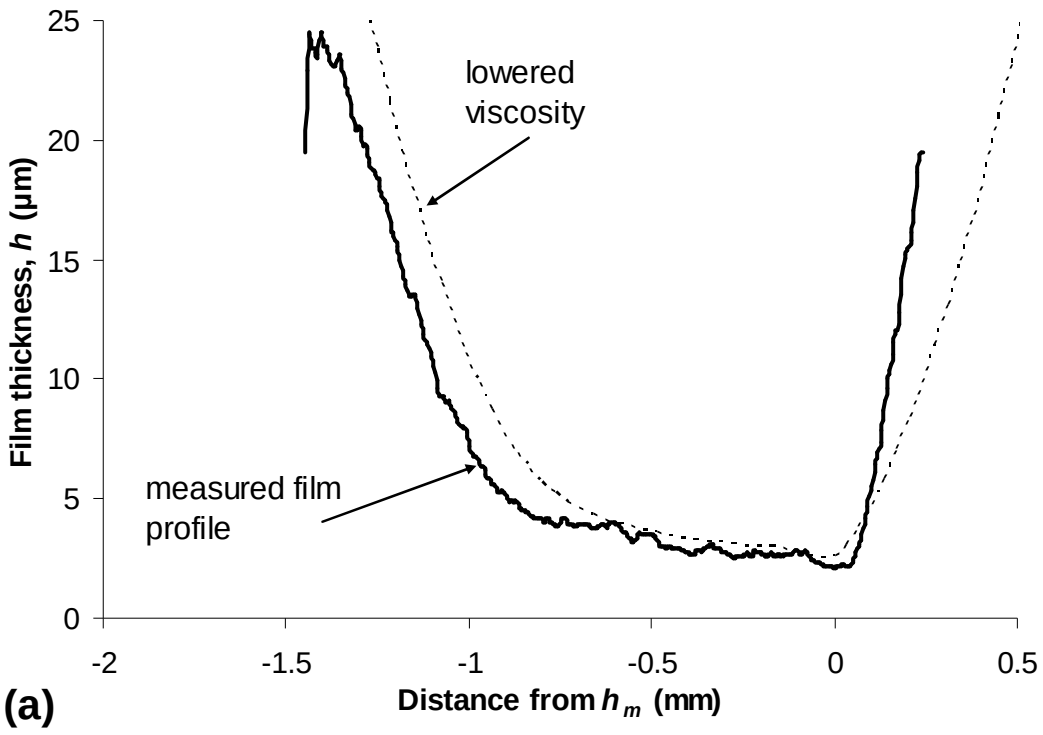

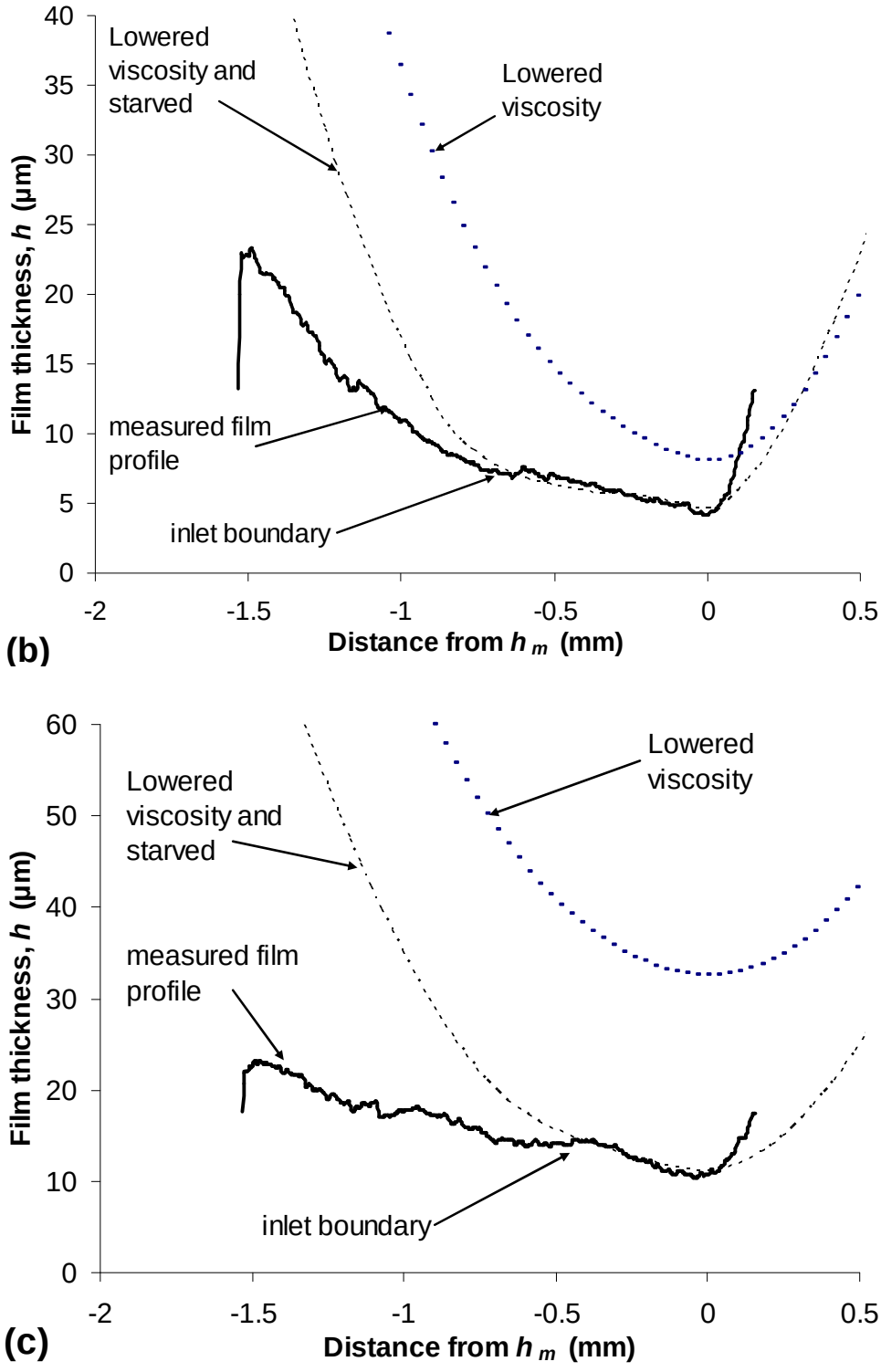

Figure 8.5. Measured and numerically predicted film thickness profiles for the tribological contact of interest, lubricated with GLY, under W = 40 mN, at (a) U = 14.6, (b) 54.8 and (c) 210 mm s^{-1}. Fluid flows from right to left. Plots have been reconciled at the minimum film thickness values, h_m.

Using the numerical solutions for compliant EHL contacts developed by de Vicente *et al.* [31], the influence of inlet length on contact shape was investigated. The solution method is described in [31]. Figure 8.6 shows the influence of inlet boundary location on the numerically predicted (a) film thickness and (b) pressure profiles for five dimensionless inlet distances. Profiles were taken along the midline in the entrainment direction (y = 0) at U = 100 mm s^{-1}, under W = 40 mN for η = 0.15 Pas. For $m \leq 1$ the contact is under severe starvation as $m = a$. Figure 8.6.c) shows the influence of inlet boundary location on the minimum film thickness; values were taken from Fig. 8.6.a).

A fully flooded state is said to exist when the inlet distance ceases to influence in any significant way the minimum film thickness. This point is the boundary between starved and fully flooded conditions, defined as the critical dimensionless inlet distance, m^*. Hamrock and Dowson give a simple description of this point; it occurs when the minimum film thickness changes ≤ 3%, as m is increased. 3% was deemed appropriate as it was believed to be the accuracy of their calculations. Therefore, when comparing h_m and m a flattening in the minimum film thickness should occur for $m > m^*$.

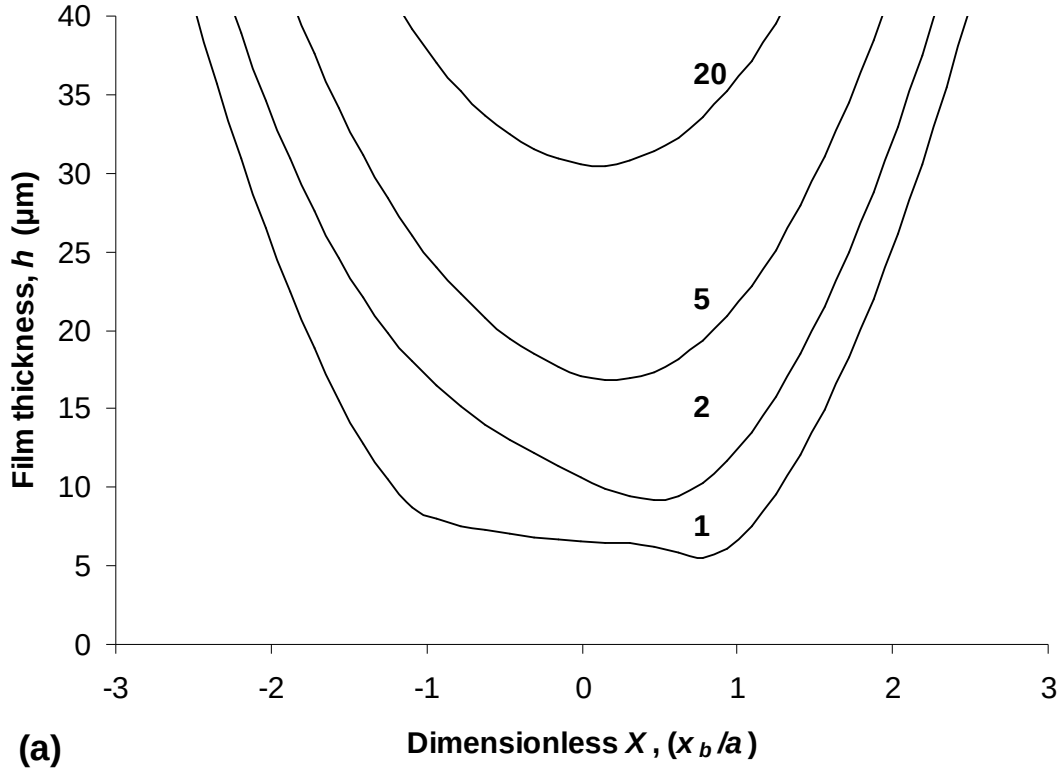
Film thickness, h (µm)
Dimensionless X , (x b /a)
20
5
2
1

(a)

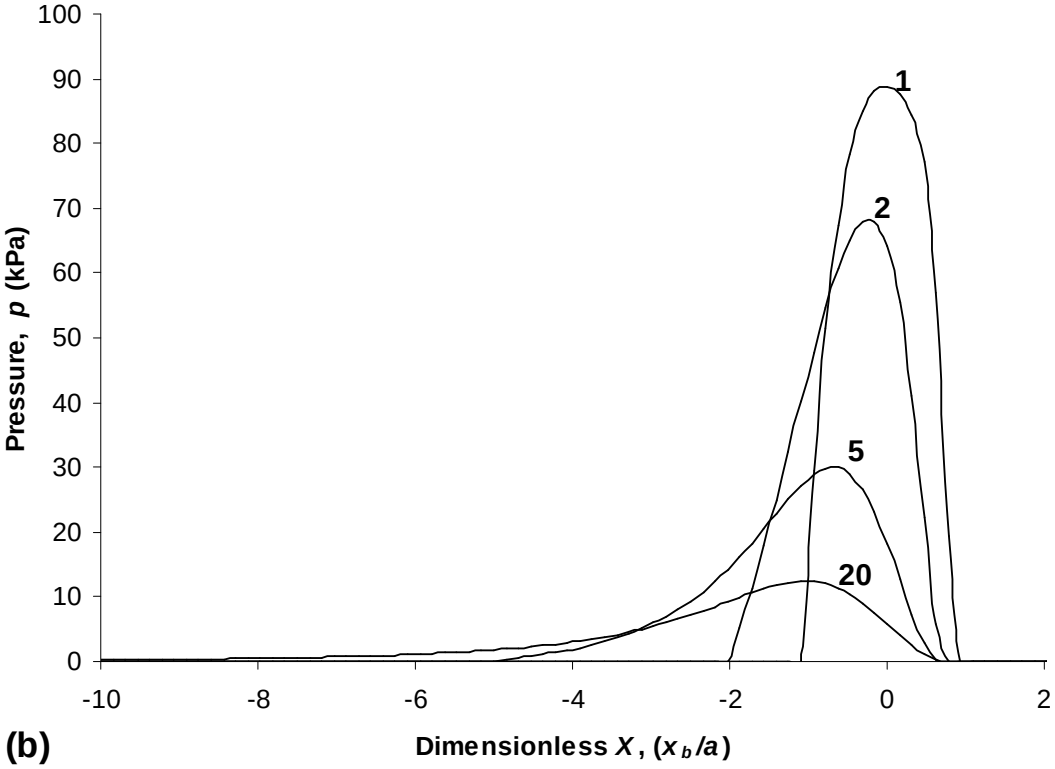
Pressure, p (kPa)
Dimensionless X , (x b /a)
1
2
5
20

(b)

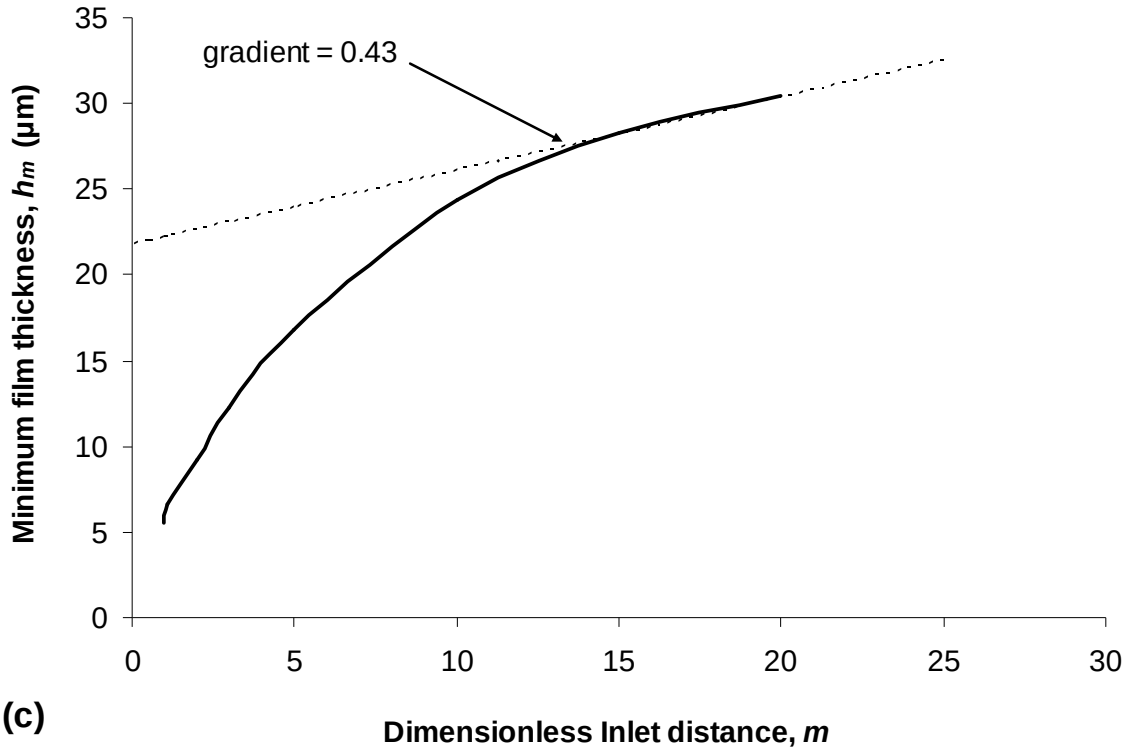

Figure 8.6. Variation in the n*umerically predicted (a) film thickness and (b) pressure profiles, for four dimensionless inlet distances, for the tribological contact of interest, lubricated with GLY, under W = 40 mN, at U = 100 mm s^{-1}. Fluid flows from right to left. (c) shows the influence of inlet boundary location on the minimum film thickness*

It is clear from Fig. 8.6.a) that the film thickness is considerably affected by inlet distance even at very large values of *m*, suggesting that the contact never reaches fully flooded conditions, even though the majority of the pressure build up occurs within an inlet distance of *m* = 4, observed in Fig. 8.6.b). As *m* is reduced, the profiles for both film thickness and pressure become more severe. This is a result of the pressure build up in the inlet reservoir occurring closer to the Hertzian contact. The contact profile becomes less of a hydrodynamic wedge, until, under severe starved conditions, the contact more closely resembles the flat profiles observed in hard/stiff contacts.

Unlike the results presented by Hamrock and Dowson [117] for the effect of dimensionless inlet distance on the minimum film thickness, there is no clear indicator in Fig. 8.6.c) for the onset of starvation. Hamrock and Dowson observed a flattening in h_m with increasing m but it can be seen in Fig. 8.6.c) that only a tentative flattening is present with a very large gradient of 0.43. There are two possible reasons for this discrepancy between de Vicente's and Hamrock and Dowson's I-EHL models; (i) a considerably larger domain size is used in the current study. At such large values of m the inlet height is large and Reynolds equation may become invalid or (ii) as suggested before, this may be a result of the much lower dimensionless speed and load parameters used in this study.

The dimensionless speed parameter for the contact of interest is lower than that used by both de Vicente *et al.* and Hamrock and Dowson, when validating their models. However, it was found that for the contact conditions in chapter 6, lubricated with SFO, a fully flooded state was achieved at $m \approx 1.2$, suggesting that the high viscosity of GLY was responsible for the continued starved state in Fig.8.6.

Based on their results, Dowson and Hamrock were able to provide an equation to predict the location of the m^*, in terms of the variables considered in this thesis for a point contact ($k = 1$), as:

$$m^* = 1 + 1.07\left(\frac{h_m}{R'}\right)^{0.16} \tag{8.2}$$

where h_m is calculated using Eq. (2.4).

Figure 8.7 shows the effect of entrainment speed on the location of m^*, calculated using Eq. (8.2), for the tribological contact of interest using both the measured and the 'effective lower' viscosities of 1.1 and 0.15 Pas respectively. Figure 8.7 clearly shows that the onset of starvation occurs at a maximum of $m^* \approx 1.6$.

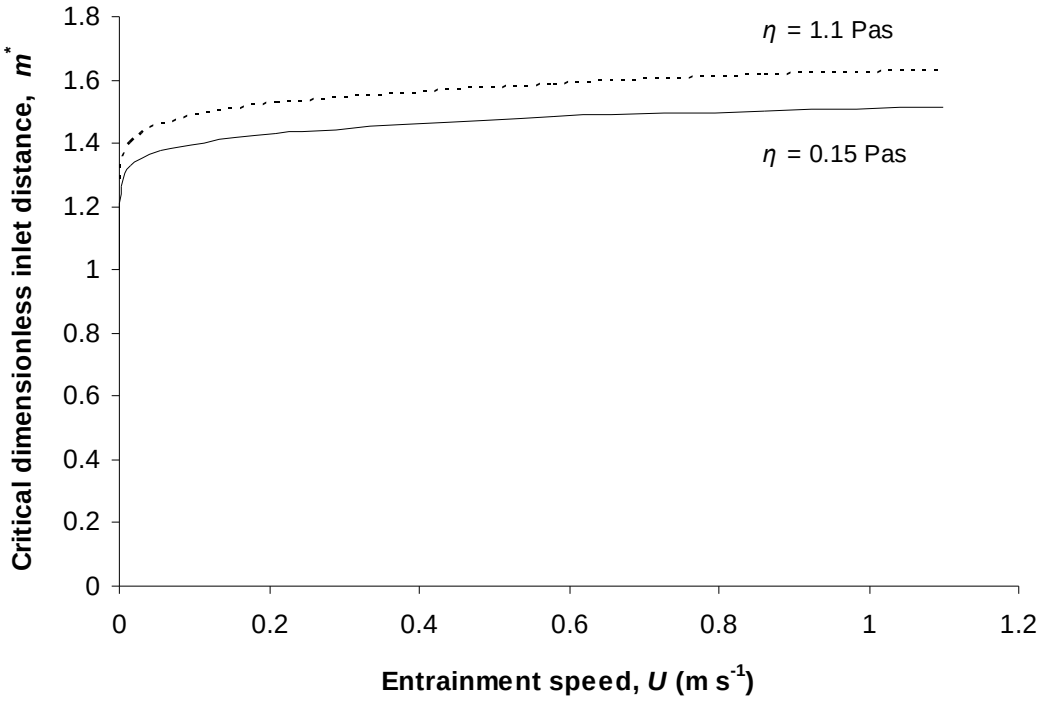

Figure 8.7. Influence of entrainment speed on the critical dimensionless inlet distance location.

It is observed in Fig. 8.7 that m^* rapidly increases at very low entrainment speeds, then, for $U > ca$ 100 mm s^{-1} only a small increase in m^* is observed (gradient of *ca* 0.1). From the results in Fig. 8.7 this would suggest that the contact of interest is in the fully flooded state for $m > 1.6$, but this conflicts with the results in Fig. 8.5 which suggest that a fully flooded state is not achieved. However, Fig. 8.7 does lend some further credence to the hypothesis that a reduction in the inlet length is a likely cause for the lower than predicted film thickness measurements. A small difference in the location of m^*, *ca* 0.1 times the Hertzian radius, is observed for a *ca* 10 times change in the viscosity. This suggests that the mismatch between theoretical and experimental film thickness values are a result of a large assumed inlet distance and not a large drop in lubricant viscosity, as previously reported.

8.3 Conclusion

This investigation has shown that fluorescence microscopy can be used to study film thickness in lubricated, compliant contacts. Results were found for three different aqueous liquids, spanning a large range of viscosity, across an entrainment speed range of 0 – 1100 mm s^{-1}.

Film thickness data obtained for fully flooded conditions showed good agreement for low viscosity fluids but film thickness was lower than predicted values for fluids with high viscosity. This was attributed to onset of inlet starvation.

A numerical solution of the point contact, starved I-EHL problem has been obtained for comparison with experimental results. The model demonstrates that contact profile shape and overall film thickness values are governed by inlet reservoir size. Good agreement with the measured values and theoretical predictions was observed for an inlet length of ca 1.1a under starved conditions, whilst a value of 2a was adequate for partially starved conditions at lower $U\eta$ values.

There are contrasting results in the theoretical predictions between numerical and empirical models for the onset of starvation within the tribological contact of interest. From the empirical model of Dowson *et al.*, Eq. (8.2), a fully flooded state is achieved for an inlet distance $m \approx 1.5$. However, if the definition is applied that a fully flooded condition exists only when the inlet distance ceases to influence in any significant way the minimum film thickness, the numerical model of de Vicente *et al.* shown in Figs. 8.5, suggests that the contact of interest never reaches a fully flooded state out to an inlet distance corresponding to the radius of the ball. Experimental verification of inlet length is required to establish a clear understanding of the onset of starvation in highly compliant I-EHL contacts. Unfortunately this was not possible with the current techniques available.

Chapter 9

Summary, conclusions and suggestions for future work

Three experimental techniques have been employed to investigate lubricated, compliant, contacts. The findings of this study are now summarised and suggestions for future work are given.

9.1 Friction investigations

Work carried out using an MTM tribometer showed the effect of load and substrate elasticity on the friction of rolling-sliding, lubricated, compliant contacts. This was first performed by varying the applied load on a PDMS disc and then by using three different polymer discs with different elastic moduli at a constant load. The investigation examined the robustness of theoretical predictions made by de Vicente *et al.* [31], for the separate rolling or sliding friction components.

Numerical predictions were shown to agree closely with the measured influence of load on I-EHL sliding friction coefficient for all tested polymers. However, the numerical models do not predict the I-EHL rolling friction coefficient accurately as a function of applied load.

Close agreement between experimental and theoretical results was found for rolling friction coefficients, with varying elastic modulus. However, theoretical models predict that there should be a negligible effect on the I-EHL sliding friction coefficient due to the elastic modulus while experimental investigations found that the sliding friction coefficient increases with decreasing elastic modulus.

Experimental results also showed that deformation energy losses in the elastic substrates are a function of the contact conditions; *i.e.* loading frequency. This has enabled the rolling friction coefficient to be predicted quite accurately, especially within the mixed and boundary lubrication regimes.

9.2 Film thickness investigations

This project set out to develop two new experimental procedures for investigating lubricant film thickness in compliant contacts. The study has demonstrated the suitability of both monochromatic optical interferometry and laser induced fluorescence (LIF) for measuring lubricant film thickness in compliant contacts. There are a number of benefits to these techniques:

- Film thickness maps can be obtained more rapidly than alternative film thickness techniques such as Raman spectroscopy [19], which tend to be time-consuming.

- The ease of film thickness mapping in compliant contacts should be of particular value when investigating the lubricating properties of shear thinning and viscoelastic solutions.

- The method can be used to validate theoretical models, in particular for I-EHL contacts.

- By combining these two techniques a large range of film thickness can be investigated. LIF can be used to study thick film thickness ($h > 2$ μm), whilst optical interferometry is suitable to study thin films ($h < 2$ μm).

- No reflective coatings are required to either contacting surface, reducing costs and eliminating possible errors created by unknown thickness on a ‘spacer layer’.

For thin film investigations into compliant contacts lubricated with single phase liquids, optical interferometry has been shown to be a suitable measurement technique. The addition of interpolating grey scale information for film thickness

values between fringe maxima and minima, first utilized by Roberts *et al.* [68], allows for more accurate contact shapes to be observed. Investigations found that the technique is limited by two major experimental factors. Firstly the contacting surfaces should be optically smooth to give clear interferograms. Any asperities, or even debris, within the contact create complex interferograms making film thickness measurements difficult. Secondly, due to the low applied loads employed during testing, vibration affects the contact size and film thickness, causing inaccuracies in film thickness results.

A LIF technique was demonstrated to be a suitable method for investigating thick films in compliant contacts, lubricated with single phase liquids. Experiments showed that a large film thickness range was achievable. Measurements were made from an upper value of *ca* 30 μm down to a minimum film thickness limit of *ca* 300 nm, with the detector system employed.

Theoretical models by de Vicente *et al.* and Hamrock *et al.* predicted higher film thickness values than obtained by both optical and LIF experimental techniques. Based on suggestions in the literature this was initially ascribed to a change in lubricant viscosity. However, although this may have been possible for glycerol, it was unlikely for sun flower oil. It is thus suggested that starvation was the main cause for the observed lower than expected film thickness. Theoretical analysis shows that, for the contact of interest lubricated with glycerol, a fully flooded state, *i.e.* one independent of inlet distance, is unlikely ever to be achieved. However, when lubricated with sunflower oil, fully flooded conditions are reached at $m \approx 1.5$. Experimental verification of inlet length is required to establish a clearer understanding for the onset of starvation in highly compliant I-EHL contacts. This was not possible with the current techniques available.

9.3 Suggestions for future work

9.3.1 Friction measurements in lubricated compliant contacts

- As discussed in chapter 2 there are a number of issues when using PDMS to mimic biological surfaces. Investigations into appropriate materials, such as Hydro-gels, could be carried out.

- Textured or structured surfaces are common in many bio-interfaces, such as the oral surfaces. The effect of such textured surfaces on the lubricating mechanisms and therefore friction is not well understood. The creation of such surfaces could be achieved using lithography and acid etching process.

9.3.2 Film thickness measurements: Optical interferometry

- General modifications could be made to the experimental apparatus to improve the accuracy of measurements. Vibrations could be reduced through the introduction of small DC servo motors and separation/isolation of motors from test apparatus.

- The creation of very smooth spherical samples is difficult and quite time-consuming. The development of moulded elastomer hemispheres, perhaps utilizing hemispherical lenses that produced high quality specimens would allow for more accurate results. The drive motor would then be

mounted at an off horizontal angle to the glass face, similar to the setup used by the MTM.

- For any optical interferometric technique the range of measureable film thickness is dependent on light coherence and therefore the type of light source employed. As the measureable film thickness range increases, resolution and accuracy diminishes. In the current study a red monochromatic light source was employed which allowed for the largest range in measureable film thickness. For very thin film thicknesses (h < 100 nm) a white light chromatic system would be best suited; however this would reduce the measureable range to *ca* 1 μm.

- The use of chromatic interferometry has yet to be achieved with lubricated, compliant, contacts due to difficulties in calibration. Development of such a calibration system would allow for the accurate measurement of low viscosity liquids and very thin films. Such a technique would also make film thickness mapping of contacts easier.

- Investigate starvation by measuring lubricant inlet distance. Development of the current technique is required for this since locating the inlet meniscus is difficult due to the low intensity of images.

9.3.3 Film thickness measurements: Laser Induced Fluorescence

- An accurate low load system needs to be employed before further experimental research is undertaken. A dead weight system would be suitable. However, if the PCS rig is continued to be used then the metallic

bellows within the sample pot need to be replaced to achieve accurate low loads.

- For future work the use of a two-dye LIF ratiometric [106] system should allow for much higher quality imaging and could provide a means of measuring very low film thicknesses. This system also allows for temperature mapping and it may also be possible to measure multiphase lubricants by adding a separate dye to each phase.

References

[1] Bongaerts J H H, Rossetti D, and Stokes J R. "The lubricating properties of human whole saliva". Tribology Letters 43 (2007), pp. 277-287. doi:10.1007/s11249-007-9232-y

[2] Gohar R. "Elastohydrodynamics: Second Edition". Imperial College Press (2001).

[3] Bhushan A D. "Introduction of Tribology". John Wiley & Sons, New York (2002).

[4] Esfahanian M and Hamrock B J. "Fluid-film lubrication regimes revisited". Tribology Transactions 34 (1991), pp. 628-632.

[5] Fujii Y. "Method for measuring transient friction coefficients for rubber wiper blades on glass surfaces". Tribology International 41 (2007), pp. 17-23.

[6] Heinrich G and Kluppel M. "Rubber friction, tread deformation and tire traction". Wear 265 (2008), pp. 1052-1060.

[7] Poll G, Gabelli A, Binnington P, and Qu J. "Dynamic mapping of rotary lip seal lubricant films by fluorescent image processing". Proceedings of the 13th Annual Conference on Fluid Sealing, BHRA, Antwerp, Belgium (1992), pp. 55-57.

[8] Poll G and Gabelli A. "Formation of lubricant film in rotary sealing contacts: Part II - A new measuring principle for lubricant film thickness". Journal of Tribology, Transactions of the ASME 114 (1992), pp. 290-296.

[9] Kaneta M, Todoroki H, and Nishikawa H. "Tribology of flexible seals for reciprocating motion". Journal of Tribology, Transactions of the ASME 122 (2000), pp. 787-795.

[10] Kaneta M, Takeshima M, Togami S, and Nishikawa H. "Stribeck curve in reciprocating seals". 18th International Conference on Fluid Sealing, BHRG, Antwerp, Belgium. (2005), pp. 333-347.

[11] Jin Z M and Dowson D. "Elastohydrodynamic lubrication in biological systems". J. Engineering Tribology, IMechE Part J 219 (2005), pp. 367-380.

[12] Dowson D and Neville A. "Bio-tribology and bio-mimetics in the operating environment". J. Engineering Tribology, IMechE Part J 220 (2006), pp. 109-123.

[13] Stokes J R and Telford J H. "Measuring the yield behaviour of structured fluids". J. Non-Newtonian Fluid Mech 124 (2004), pp. 137-146.

[14] de Vicente J, Stokes J R, and Spikes H A. "Soft lubrication of model hydrocolloids". Food Hydrocolloids 20 (2005), pp. 483-491. doi:10.1016/j.foodhyd.2005.04.005

[15] de Vicente J, Stokes J R, and Spikes H A. "Viscosity ratio effect in the emulsion lubrication of soft EHL contact". Journal of Tribology, Transactions of the ASME 128 (2007), pp. 795-800.

[16] de Vicente J, Stokes J R, and Spikes H A. "Lubrication properties of non-absorbing polymer solutions in soft elastohydrodynamic (EHD) contacts". Tribology International 38 (2005), pp. 515–526.

[17] Adams M J, Briscoe B J, and Johnson S A. "Friction and lubrication of human skin". Tribology Letters 26 (2007), pp. 239-253.

[18] de Vicente J, Stokes J R, and Spikes H A. "Rolling and sliding friction in compliant, lubricated contact". J. Engineering Tribology, IMechE Part J 220 (2006), pp. 55-63.

[19] Bongaerts J H H, Day J P R, Marriott C, Pudney P D A, and Williamson A M. "In situ confocal Raman spectroscopy of lubricants in a soft

elastohydrodynamic tribological contact". Journal of Applied Physics 104 (2008), doi:10.1063/1.2952054 (10 pages).

[20] Lee S and Spencer N D. "Aqueous lubrication of polymers: Influence of Surface modification". Tribology International. 38 (2005), pp. 922-930.

[21] Malone M E, Appelqvist I A M, and Norton I T. "Oral behaviour of food hydrocolloids and emulsions. Part 1". Food Hydrocolloids 17 (2003), pp. 763-773.

[22] Prinz J F, de Wijk R A, and Huntjens L. "Load dependency of the coefficient of friction of oral mucosa". Food Hydrocolloids 21 (2007), pp. 402-408.

[23] Tang W and Bhushan B. "Adhesion, friction and wear characterization of skin and skin cream using atomic force microscope". Colloids and Surfaces B: Biointerfaces 76 (2010), pp. 1-15.

[24] Tang W, Bhushan B, and Ge S. "Friction, adhesion and durability and influence of humidity on adhesion and surface charging of skin and various skin creams using atomic force microscopy". Journal of Microscopy 239 (2010), pp. 99-116.

[25] Bongaerts J H H, Stokes J R, and Fourtouni K. "Soft-Tribology: lubrication in compliant PDMS-PDMS contact". Tribology International 40 (2007), pp. 1531-1542.

[26] Vorvolakos K and Chaudhury M K. "The effects of molecular weight and temperature on the kinetic friction of silicone rubbers". American Chemical Society 19 (2003), pp. 6778-6487.

[27] Hillborg H and Gedde U W. "Hydrophobicity recovery of polydimethylsiloxane after exposure to corona discharges". Polymer 39 (1998), pp. 1991-1998.

[28] Hillborg H, Ankner J F, Gedde U W, Smith G D, Yasuda H K, and Wikstrom K. "Crosslinked polydimethylsiloxane exposed to oxygen plasma studied

by neutron reflectometry and other surface specific techniques". Polymer 41 (2000), pp. 6851-6863.

[29] Hillborg H, Sandelin M, and Gedde U W. "Hydrophobic recovery of polydimethylsiloxane after exposure to partial discharges as a function of crosslink density". Polymer 42 (2001), pp. 7349-7362.

[30] Schneemilch M and Quirke N. "Effect of oxidation on the wettability of poly(dimethylsiloxane) surfaces". The Journal of Chemical Physics 127 (2007), doi:10.1063/1.2770723 (7 pages).

[31] de Vicente J, Stokes J R, and Spikes H A. "The frictional properties of Newtonian fluids in rolling-sliding soft-EHL contact". Tribology Letters 20 (2005), pp. 273-286.

[32] Ranc H, Servais C, Chauvy P F, Debaudl S, and Mischler S. "Effect of surface structure on frictional behaviour of a tongue/palate tribological system". Tribology International 39 (2006), pp. 1518-1526.

[33] Dresselhuis D M, de Hoog E H A, Sturat M A C, and van Aken G A. "A tribological comparison between oral tissue and PDMS rubber in an emulsion perception context". Food Hydrocolloids 22 (2008), pp. 323-335.

[34] Cassin G, Heinrich E, and Spikes H A. "The influence of surface roughness on lubrication properties of absorbing and non-absorbing biopolymers". 1-6-2001. Tribology Letters 11 (2001), pp 95-102.

[35] Lane T B and Hughes J R. "A study of the oil film formation in gears by electrical resistance measurements". J.Appl.Phys. 3 315 (1952).

[36] Dyson A. "Investigation of the discharge voltage method of measuring the thickness of oil films formed in disc machine under conditions of elastohydrodynamic lubrication". Proc Instn Mech Engrs 181 (1966), pp. 633-646.

[37] Sirpongse C, Rogers P R, and Cameron A. "Thin film lubrication 1 - Discharge through thin oil films". Engineering 186 (1958), pp. 146-147.

[38] Sirpongse C and Cameron A. "Thin film lubrication 2 -Lubrication of the four ball machine". Engineering 186 (1958), pp. 147-149.

[39] Spikes H A. "Thin films in elastohydrodynamic lubrication; the contribution of experiment". J. Engineering Tribology, IMechE Part J 213 (1999), pp 335-352.

[40] PCS Instruments. "PCS Instruments website". 2010.

[41] Marginson H J, Olver A V, and Sayles R S. "Limitations of thin film microtransducers in highly loaded contacts". Tribology International 28 (1995), pp. 517-521.

[42] Goodman J. "Recent researches in friction". Proc.Instn.Civ.Engrs ixxxv, 1-19 (1886).

[43] Ku I S Y, Reddyhoff T, Choo J H, Holmes A S, and Spikes H A. "A novel tribometer for the measurement of friction in MEMS". Tribology International 43 (2010), pp. 1087-1090.

[44] Reddyhoff T. "Ultrasonic measurements techniques for lubricant films". PhD Thesis. Sheffield University Press (2007).

[45] Sibley L B and Orcutt F K. "Elastohydrodynamic lubrication of rolling contact surfaces". ASLE Trans. 4 (1961), pp. 234-249.

[46] Reddyhoff T, Spikes H A, and Olver A V. "Improved infrared temperature mapping of elastohydrodynamic contacts". J. Engineering Tribology, IMechE Part J 223 (2009), pp. 1165-1177.

[47] Spikes H A, Anghel V, and Glovnea R. "Measurement of the rheology of lubricant films within elastohydrodynamic contacts". Tribology Letters 17 (2004), pp. 593-605.

[48] Cann P M E, Aderin M, Johnston G J, and Spikes H A. "An investigation into the orientation of lubricant molecules in EHD contacts". Wear

Particles, Proceedings of 18th Leeds-Lyon Symposium on Tribology, Lyon, France (1991).

[49] Dvorak A D, Wahl K J, and Singer I L. "Friction behavior of Boric Acid and Annealed Boron Carbide coatings studied by in situ Raman tribometry". Triboloy Transactions 45 (2002), pp. 354-362.

[50] Bae A C, Lee H, Lin Z, and Granick S. "Chemical Imaging in a Surface Forces Apparatus: Confocal Raman Spectroscopy of Confined Poly(dimenthylsiloxane)". Langmuir 25 (2005), pp. 5685-5688.

[51] B Bhushan. "Fundamentals of Tribology and Bridging the Gap Between the Macro and Micro/Nanoscales". Kluwer Academic Publishers (2001), pp. 663-689.

[52] Gohar R and Cameron A. "Optical measurement of oil film thickness under elastrohydrodynamic lubrication". Nature 200 (1963) pp. 458-459.

[53] Blok H and Koens H J. "The 'breathing' film between a flexible seal and reciprocating rod". Proc. Instn. Mech. Engrs. (1965), pp. 221-223.

[54] Cameron A and Gohar R. "Theoretical and experimental studies of the oil film in lubricated point contact". Proc. Roy. Soc. Lond A 291 (1966), pp. 520-536.

[55] Gohar R and Cameron A. "The mapping of elastrohydrodynamic contacts". ASLE Trans. 10 (1967), pp. 215-225.

[56] Wedeven L D. "Optical measurements in elastrohydrodynamic rolling-contact bearing". PhD Thesis. University of London (1970).

[57] Foord C A, Hammann W C, and Cameron A. "Evaluation of lubricants using optical elastohydrodynamics". ASLE Trans 11 (1968), pp. 31-43.

[58] Westlake F L. "An interferometric study of ultra thin fluid films". PhD Thesis. University of London (1970).

[59] PCS Instruments. "EHL system manual". PCS Instruments Ltd. London (1993).

[60] Gustafsson L, Hoglund E, and Marklund O. "Measuring lubricant film thickness with image analysis". J. Engineering Tribology, IMechE Part J 208 (1994), pp. 199-205.

[61] Cann P M E. "Understanding grease lubrication". Proc. Leeds-Lyon Symp. on Tribology, The Third Body Concept: Interpretation of Tribological Phenomena (1996).

[62] PCS Instruments. "SLIM manual". PSC Instruments Ltd. London (1998).

[63] Krupka I, Hartl M, and Liska M. "Influence of contact pressure on central and minimum film thickness within ultrathin film lubricated contacts". Journal of Tribology, Transactions of the ASME 127 (2005), pp. 890-892.

[64] Hartl M, Krupka I, Poliscuk R, and Liska M. "An automatic system for real-time evaluation of EHD film thickness and shape based on the colorimetric interferometry". Tribology Transactions 42 (1992), pp. 303-309.

[65] Hartl M, Krupka I, Poliscuk R, and Liska M. "Thin film colorimetric interferometry". Tribology Transactions 44 (2001), pp. 270-276.

[66] Hartl M, Krupka I, Fuis V, and Liska M. "Experimental study of lubricant film thickness behaviour in the vicinity of real asperities passing through lubricated contact". Tribology Transactions 47 (2004), pp. 376-385.

[67] Roberts A D and Tabor D. "Fluid film lubrication of rubber - an interferometric study". Wear 2 (1968), pp. 163-166.

[68] Roberts A D and Tabor D. "The extrusion of liquids between highly elastic solids". Proceedings of the Royal Society of London, Series A 325 (1971) pp. 323-345.

[69] Richards S C and Roberts A D. "Boundary lubrication of rubber by aqueous surfactant". J. Phys D: Applied Physics 25 A72 (1992), doi: 10.1088/0022-3727/25/1A/014.

[70] Roberts A D. "Optical rubber". Rubber Developments 29 (1976), pp. 7-11.

[71] Roberts A D. "The shear of thin liquid films". Journal of Physics D 4 (1971), pp. 433-440.

[72] Roberts A D. "Squeeze films between rubber and glass". Journal of Physics D 4 (1971), pp. 423-432.

[73] Field G J and Nau B S. "Lubrication behaviour in loaded rubber contacts". Wear 65 (1975), pp. 79-85.

[74] McClune C R and Briscoe B J. "Elastohydrodynamic films formed between a rubber cylinder and glass plate: a comparison of theory and experiment". Journal of Physics D: Applied Physics 10 (1977), pp. 587-596.

[75] Sugimura J, Hashimoto M, and Yamamoto Y. "Study of elastohydrodynamic contacts with fluorescence microscope". Proc. Leeds Lyon Symposium on Tribology, Thinning Films and Tribological Interfaces 38 (2000), pp. 609-617.

[76] Hidrovo C H and Hart D P. "2D thickness and temperature mapping of fluids by means of a two-dye laser induced fluorescence ratiometric scheme". Journal of Flow Visualization and Image Processing 9 (2002), pp. 171-191.

[77] Hidrovo C H, Brau R R, and Hart D P. "Excitation nonlinearities in emission reabsorption laser-induced fluorescence techniques". Applied Optics 43 (2004), pp. 894-913.

[78] Dowson D and Higginson G R. "Elastohydrodynamic Lubrication". SI edition. Pergamon Press, Oxford (1977).

[79] Greenwood J A and Tabor D. "The friction of hard sliders on lubricated rubber: The importance of deformation losses". Proc. Phys. Soc 71 (1958), pp. 989-1001.

[80] Greenwood J A, Minshall H, and Tabor D. "Hysteresis losses in rolling and sliding friction". Proc. R. Soc. Lon. Series A 259 1299 (1961), pp. 480-507.

[81] Johnson S A, Gorman D M, Adams M J, and Briscoe B J. "The friction and lubrication of human stratum corneum". Proceedings of 19th Leeds-Lyon Symposium on Tribology, Thin Films in Tribology. Leeds, UK. (1992), pp. 663-672.

[82] Briscoe B J and Tabor D. "Friction and Wear of Polymers". Polymer Science. 1 (1978).

[83] Stachowiak G W and Batchelor A W. "Engineering Tribology". Elsevier (2005).

[84] PCS Instruments. "PCS MTM Instruction manual". London, PSC Instruments Ltd (1993).

[85] PCS Instruments. "Soft contact option manual supplement". London, PSC Instruments Ltd (1995).

[86] Douglas J F, Gasiorek J M, and Swaffield J A. "Fluid Mechanics 4th Edition". Pearson Education limited (2001).

[87] Callister W D. "Materials Science and Engineering. An Introduction". John Wiley & Sons, Inc (2000).

[88] Pan X D. "Significance of tuning bulk viscoelastic via polymer molecular design on wet sliding friction of elastomer compounds". Tribology Letters 20 (2005) 209-219.

[89] Matsuoka S. "Viscoelasticity and thermal analysis". Journal of Thermal Analysis and Calorimetry 59 (2000), pp. 131-141.

[90] Omata N, Suga T, Furusawa H, Urabe S, Kondo T, and Ni Q. "Viscoelasticity evaluation of rubber by surface reflection of supersonic wave". Ultrasoncis 44 (2006), pp. 211-215..

[91] Krevelen V. "Properties of polymers. Their correlation with chemical structure, their numerical estimation and prediction from additive group contributions". Elsevier Science Publishing Company INC (1990).

[92] Williams M L, Landel R F, and Ferry J D. "The temperature dependence of relaxation mechanisms in amorphous polymers and other glass-forming liquids". J. Am. Chem. Soc 77 (1955), pp. 3701-3707.

[93] Tanner R I. "Engineering Rheology: Second Edition". Oxford University Press (2000).

[94] Gohar R. "Oil films under elasto-hydrodynamic conditions". PhD Thesis., University of London (1965).

[95] Michelson A A. "Light Waves and Their Uses". Second Series, Vol. III. The Decennial Publications, University of Chicago Press (1902).

[96] Dow ltd.. "Viscosity of Aqueous Glycerine Solutions". http://www.dow.com/glycerine/resources/table18.htm . (2009).

[97] Hamrock B J and Dowson D. "Elastrohydrodynamic lubrication of elliptical contacts for materials of low elastic modulus 1 - Fully flooded conjunction". NASA TN D-8528 (1977).

[98] Cameron A. "Basic Lubrication Theory". London, Longman (1971).

[99] Hamrock B J and Dowson D. "Isothermal Elastohydrodynamic Lubrication of Point Contacts. Part III-Fully Flooded Results". J.Lubr.Technol, Transactions of ASME. 99 (1977), pp. 264-276.

[100] Abramovic H and Klofutar C. "The temperature dependence of dynamic viscosity for some vegetable oils". Acta Chim.Slov. 45 (1998), pp. 66-77.

[101] Oliveira S A G and Bower A F. "An analysis of fracture and delamination in thin coatings subjected to contact loading". Wear 198 (1996), pp. 15-32.

[102] Olver A V. "Correlation factors for the 2D coated Hertzian contact problem". Wear 212 (1997), pp. 265-267.

[103] Meijers P. "The contact problem of a rigid cylinder on an elastic layer". Appl.Sci.Res. 18 (1968), pp. 353-383.

[104] Liu S B, Peyronnel A, Wang Q J, and Keer L M. "An extension of the Hertz theory for three-dimensional coated bodies". Tribology Letters 18 (2005), pp. 303-314.

[105] Johnson K L. "Contact Mechanics". Ninth print, Cambridge University Press (2003), pp. 136-141.

[106] Hidrovo C H and Hart D P. "Emission reabsorption laser induced fluorescence (ERLIF) film thickness measurement". Meas.Sci.Technol. 12 (2001), pp. 467-477.

[107] Haugland R P. "Handbook of Fluorescent Probes and Research Chemicals 7th Edn". 1999.

[108] Hoult D P, Lux J P, and Wong V W. "Calibration of laser fluorescence measurements of lubricant film thickness in engines". Society of Automotive Engineers. Technical Paper 881587 (1988).

[109] Eguchi M and Yamamoto T. "Shear characteristics of a boundary film for a paper-based wet friction material: friction and real contact area measurement". Tribology International 38 (2005), pp. 327-335.

[110] Greenwood J A. "Adhesion of elastic spheres". Proc. R. Soc. Part A 453 (1997), pp. 1277-1297.

[111] Greenwood J A and Johnson K L. "An alternative to the Maugis model of adhesion between elastic spheres". Journal of Applied Physics 31 (1998), pp. 3279-3290.

[112] Chevalier F C, Lubrecht A A, Cann P M E, Dalmaz G, and Colin F. "Film thickness in starved EHL point contacts". J. of Tribology, Transaction of ASME. 120 (1998), pp. 126-133.

[113] Cann P M E, Damiens B, and Lubrecht A A. "The transition between fully flooded and starved regimes in EHL". Tribology International 37 (2004), pp. 859-864.

[114] Cann P M E. "Thin-film grease lubrication". J. Engineering Tribology, IMechE Part J 213 (1999), pp. 405-416.

[115] Wedeven L D, Evans D, and Cameron A. "Optical analysis of ball bearing starvation". Journal .Lubr.Tech, Transactions of the ASME. 93 (1971), pp. 349-363.

[116] Hamrock B J and Dowson D. "Ball Bearing Lubrication- The Elastohydrodynamics of Elliptical Contacts". Wiley-Interscience, New York (1981).

[117] Hamrock B J and Dowson D. "Elastohydrodynamic lubrication of elliptical contacts for materials of low elastic modulus. II - Starved conjunction". Journal .Lubr.Tech, Transactions of the ASME. 101 (1979), pp. 92-98.